Fall 2017

Engineering advanced adsorbent materials for CO_2 capture applications

Harshul Thakkar

Department: Chemical and Biochemical Engineering

ENGINEERING ADVANCED ADSORBENT MATERIALS FOR CO_2 CAPTURE APPLICATIONS

by

HARSHUL VIPUL THAKKAR

A DISSERTATION

Presented to the Faculty of the Graduate School of the

MISSOURI UNIVERSITY OF SCIENCE AND TECHNOLOGY

In Partial Fulfilment of the Requirements for the Degree

DOCTOR OF PHILOSOPHY

in

CHEMICAL ENGINEERING

2017

Approved by

Dr. Fateme Rezaei, Advisor

Dr. Ali Rownaghi

Dr. Douglas Ludlow

Dr. Xinhua Liang

Dr. Glenn Morrison

PUBLICATION DISSERTATION OPTION

This dissertation consists of the following four articles that have been published as follows:

PAPER I Pages 16-42. 3D-Printed Zeolite Monoliths for CO_2 Removal from Enclosed Environments, has been published in ACS Applied Material and Interfaces.

PAPER II Pages 43-67. Formulation of Aminosilica Adsorbents into 3D-Printed Monoliths and Evaluation of their CO_2 Capture Performance, has been published in ACS Applied Material and Interfaces.

PAPER III Pages 68-92. 3D-Printed Metal-Organic Framework Monoliths for Gas Adsorption Processes, has been published in ACS Applied Material and Interfaces.

PAPER IV Pages 93-115. CO_2 capture from air using amine functionalized kaolin-based zeolites, has been published in Chemical Engineering & Technology.

ABSTRACT

Global climate change due to the increasing CO_2 concentration in the atmosphere is primarily associated with anthropogenic CO_2 emissions. CO_2 capture technologies using adsorbents have not been implemented commercially due to lack of scalable, practical and cost-effective strategies and are still under development. Moreover, the use of conventional configurations such as pellets and beads for the removal of CO_2 from enclosed environments have been shown to impose limitations to the removal efficiency and system performance. In this dissertation, engineering of advanced and efficient structured adsorbents for practical and scalable CO_2 capture technologies and their use in CO_2 removal from enclosed environments and flue gas streams are reported.

Additive manufacturing (3D printing) technique in fabrication of adsorbents have not been explored. Herein, various adsorbents such as zeolites, aminosilicas and metal-organic frameworks (MOFs) have been formulated in monolithic form using 3D printing technique. In order to yield a robust structure with high adsorbent capacity, the composition and printing conditions were optimized accordingly. After characterizing the structural and physical properties of 3D-printed monolithic adsorbents, their equilibrium and dynamic CO_2 adsorption performance were evaluated by various techniques. This investigation has shown that 3D printing technique offers an alternative, cost-effective and facile approach to fabricate monolithic adsorbents with tunable structural, physical and mechanical properties.

In addition to the 3D-printed monoliths, several cost-effective zeolite-based adsorbents were synthesized from abundant and inexpensive kaolin clay. To enhance the adsorption capacity, the materials were then impregnated with aminopolymer and evaluated for CO_2 capture from air.

AKNOWLEDGEMENTS

First, I thank my advisor, Dr. Fateme Rezaei for her continuous support and guidance throughout my graduate studies at Missouri University of Science and Technology. Her assistance with her critical thinking and knowledge towards technical, academic and research area benefit me to conduct research, learning and creating knowledge efficiently and productively for science.

I thank to my co-advisor Dr. Ali Rownaghi for his continuous support and scientific discussions throughout pursuit of my graduate studies. I also thank him for allowing me to use the instruments to conduct my research work. I also thank my peers of both labs, Adsorption and Separation Laboratory as well as Catalysis and Membranes Research Laboratory, who helped me in my research work.

I thank chairman, Dr. Al-Dahhan, of the Department of Chemical and Biochemical Engineering at Missouri University of Science and Technology for some financial support. I thank my committee members, Dr. Xinhua Liang, Dr. Douglas Ludlow and Dr. Glenn Morrison. I also thank the staff member of the department for helping me in other resources. I also thank Missouri S&T MRC and AMCL laboratory for allowing me use instruments.

Last but not least, I am hereby expressing my special thanks to my family and also relatives for their support and encouragement.

TABLE OF CONTENTS

Page

LIST OF FIGURES

PAPER II

PAPER III

LIST OF TABLES

SECTION
1. INTRODUCTION

1.1. NECESSITY OF CAPTURING CO_2

Carbon dioxide is one of the primary reasons for the global warming due to its continuous emissions into the atmosphere. The demand of energy increasing with human population is resulting in global climate change associated with the continuous CO_2 emissions from large point sources such as coal power plants, cement plants steel industries, oil refineries, as examples. In addition, the small distributed sources such as the human respiratory system, vehicular exhaust and deforestation contribute majorly in rising CO_2 concentration level in the atmosphere. As a result, the CO_2 concentration level in the atmosphere has substantially increased to 403 ppm which was reported by National Oceanic and Atmospheric Administration (NOAA), as depicted in Figure 1.1.[1] Thus, the cause for concern of rising CO_2 emission level that has called for urgent cuts in the emission of greenhouse gases, especially CO_2.

There are number of routes such as pre-combustion, during combustion and post-combustion have been taken into consideration to capture CO_2 efficiently from large point sources. Although CO_2 can be captured productively during pre-combustion and combustion processes, complexity and high cost still hamper the commercialization. These factors have led researchers to investigate and develop technologies for CO_2 capture from post-combustion process. Since CO_2 capture from large point sources can only control the emissions, an alternative concept of lowering the CO_2 concentration from the atmosphere called “direct air capture (DAC)” or “negative carbon” was introduced by Lackner *et al*.[2] DAC technique offers to dispose stored CO_2 from one point source to another, where it has

the least impact on the environment and human activities or close to the CO_2 recycling centers.

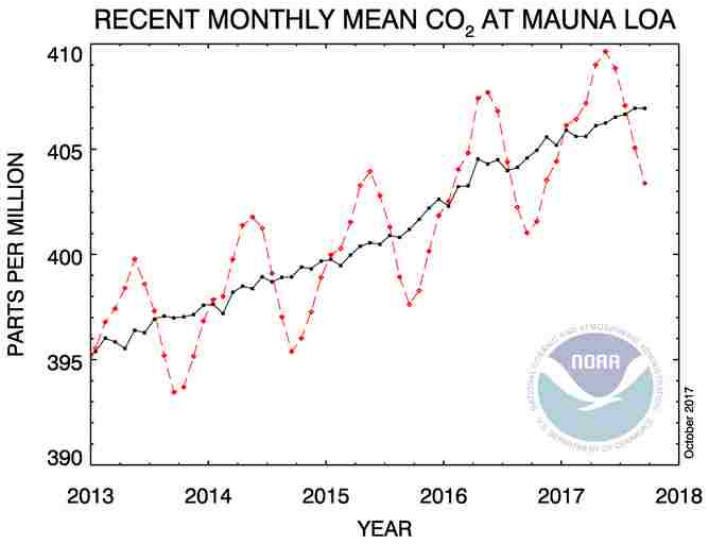

Figure 1.1. Recent monthly mean CO2 at Mauna Loa by NOAA.[1]

A continuous release of CO_2 deteriorates indoor air quality (IAQ) in offices, conventional buildings and such closed habitats. Ground-Gas Solutions Limited (GGS) reported daily carbon dioxide concentrations between 1000 to 1400 ppm during day time working hours.[3] Also, similar CO_2 concentration level was monitored in enclosed environments mentioned by Environmental Protection Administration (EPA), Taiwan, R.O.C.[4] Concentration above 1000 ppm indicate poor air quality leading to health problems.

In addition to capture CO_2 from post-combustion flue gas and air, it is essential to sequestrate CO_2 from enclosed environments such as submarines, space shuttles and air planes. The report by Wisconsin Department of Health Services demonstrated that the diffused carbon dioxide in the body is carried by blood in chemical combination with

hemoglobin.[5] According to Occupational Safety and Health Administration (OSHA), long-term exposure to CO_2 in a sealed environment increases CO_2 partial pressure in body which can result in immediate increase of carbon dioxide tension of blood leading to severe health problems such as headaches, dizziness, restlessness, needles feeling, difficulty breathing, sweating, fatigue, tiredness, elevated blood pressure, asphyxia and malaise, as shown in Figure 1.2.[6,7] These problems associate with elevated CO_2 concentration in enclosed environments are mainly because of inadequate ventilation and inefficient system. As a result, removal of CO_2 in enclosed environment is also gaining importance among researchers.

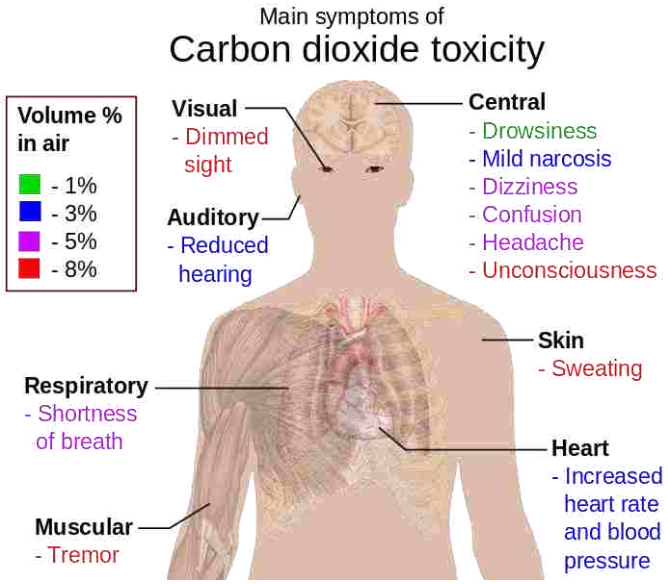

Figure 1.2. Schematic of health risks associated with long term CO_2 exposure.[7]

In sealed environments such as submarine and space shuttles, a moderated high indoor concentration of CO_2 (~3500 ppm) can directly impact decision making performance. Based on the study conducted in Lawrence Berkeley National Laboratory by Mendell and

his co-worker[8] , concentration level above 2500 ppm can significantly reduce productive decision making performance up to ~65% considering all activities, as shown in Figure 1.3. Therefore, continuous replacement of sorbent, efficient ventilation and maintenance are required in sealed environments to prevent unproductivity and health risks.

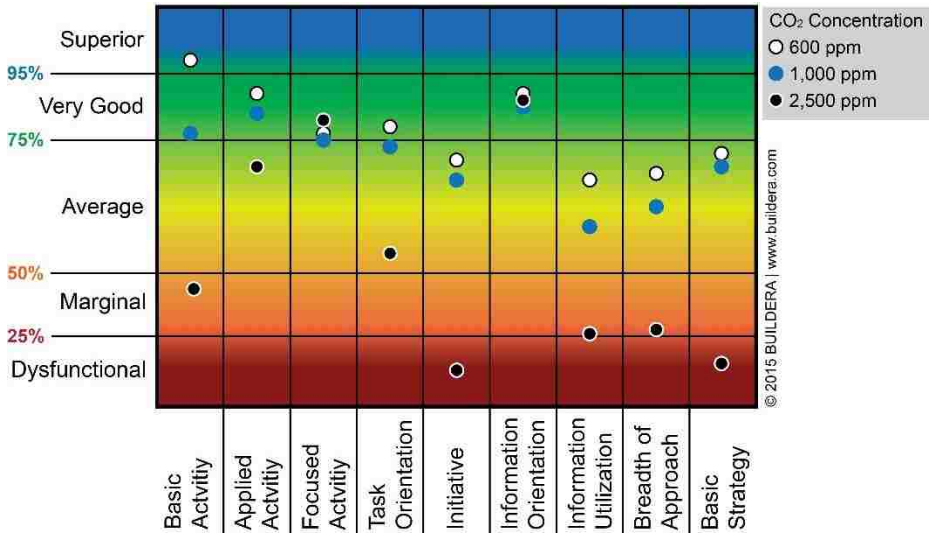

Figure 1.3**.** Impact of CO_2 exposure on human decision making performance.[8]

1.2. CURRENT CO_2 CAPTURE TECHNOLOGY

The post-combustion CO_2 capture technology adopted commercially is mainly based on absorption using aqueous amine solutions such as monoethanolamine (MEA), diaethanolamine (DEA) and methyldiaethanolamine (MDEA). Although absorption technology has been the commercially, it entails major drawbacks such as amine regeneration, corrosive properties of aqueous solutions and most importantly the loss of amines. Therefore, development of alternative CO_2 capture technologies have been suggested prevent the issues associated with absorption technology.

1.3. UPCOMING CO_2 CAPTURE TECHNOLOGIES

Several alternative processes such as membrane separation, chemical looping and adsorption have been developed for CO_2 capture to circumvent problems associated with absorption technology.[9,10] Membrane technology for CO_2 gas separation application has recently gained considerable attention due to its high selectivity, economic feasibility, and compatibility with the environment. Composite hollow fibers, a combination of polymers and adsorbents, have been developed for large scale CO_2 adsorption strategies.[11] In addition, silica supported hollow fiber membranes have been functionalized with polyethylenamine (PEI) and aminosilane (APS) and investigated for CO_2 capture.[11–15] Significant separation can be achieved in pre-combustion or during combustion processes, while post-combustion separation using membranes is very challenging due to poor selectivity of CO_2. Chemical looping has proven to be an efficient process in which a fluidized bed is composed of metal oxide and continuously supplied with oxygen. As a result, two discrete flue gas streams, one with N_2 and O_2 whereas another stream of CO_2 and H_2O from flue gas are obtained. Although significant separation can be achieved with a suitable oxygen carrier, chemical looping technology is still not favored because of high cost of the air separation unit to obtained pure oxygen.

1.4. ADSORPTION-BASED CO_2 CAPTURE

The adsorption technologies have found to provide significant CO_2 capture capacity using promising adsorbents such as hydrotalcites, alkali or alkaline-earth oxides, calcium oxides, alkali silicates and zirconates, and double salts, at high temperatures (chemisorbents) whereas low temperatures (physisorbents) adsorbents cover metal oxides, porous polymer networks (PPNs) activated carbon, covalent organic frameworks (COFs),

amine based sorbents, zeolites, and metal-organic frameworks (MOFs).[10] In general, CO_2 capture from flue gas, ambient air and enclosed environments is performed at ambient temperature, with zeolites, amine based sorbents and MOFs as the most widely investigated adsorbents. The key properties of promising adsorbents are high porosity, tunable morphology, high surface area, significant capture capacity, regenerability and high stability.[16] Also, adsorption based cyclic processes such as pressure swing adsorption (PSA) and temperature swing adsorption (TSA) offer superior CO_2 separation strategies.[10,17]

Zeolites are crystalline microporous materials with well define structure mainly composed of aluminosilicate (AlO^{4-}-SiO^{4-}) tetrahedral coordination framed with cations or protons within the cavities or channels.[18,19] Based on various three dimensional frameworks, each zeolite are assigned with unique framework types/codes. For example, MFI for ZSM-5, FAU for zeolite Y, CHA for SAPO-34 or SSZ-13, LTA for zeolite X as shown in Figure 1.4.[20] Because of their different uniform crystalline structures with unique properties, zeolites are extensively used in various applications such as gas adsorption and separations, catalysis, water softening and purifications, petrochemical cracking, as examples.[21–24]

Zeolites have proven to be a potential candidate for DAC, CO_2 capture from enclosed environments and CO_2 capture from flue gases due to its porous crystalline structure. However, developing cost-effective strategies cannot be achieved if conventionally produced zeolites are used. Therefore, zeolites have been synthesized using various routes such as microwave synthesis, organo-template and/or solvent free zeolites, and from inexpensive natural clays.[25,26] The optimum route to synthesize zeolites has found to be

from natural clays such as bentonite clay, kaolin clay, Indian clays, South African clays, as examples, due to its abundant occurrence.[27,28] The conversion of zeolites from clay have been studied extensively for catalysis and adsorption. [26,28–31]

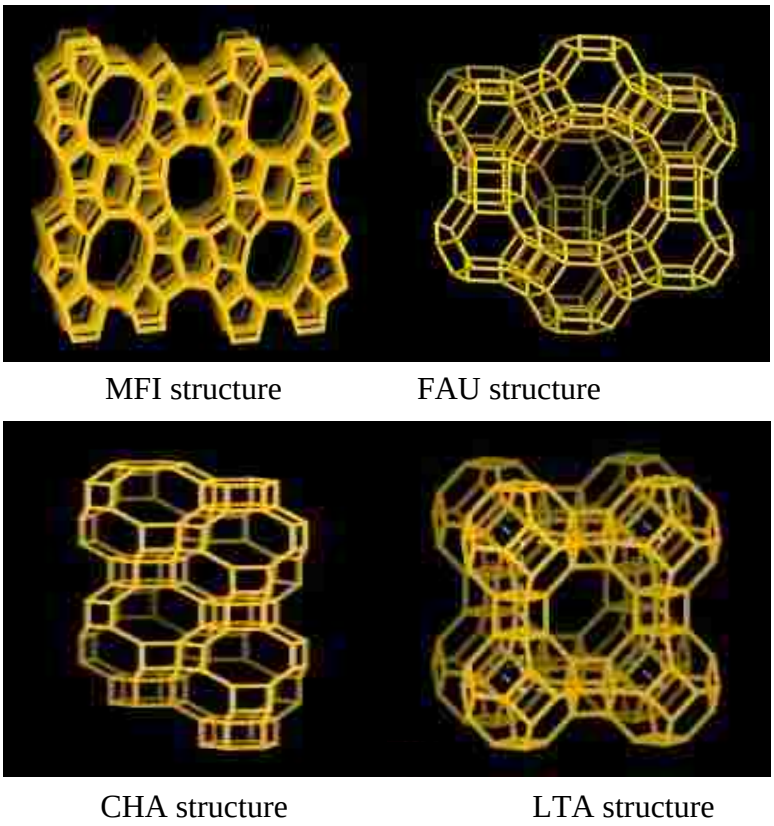

Figure 1.4. Chemical structures of various zeolite frameworks.[20]

Amine-based adsorbents have been extensively investigated for carbon capture as adsorbents supported with amines exhibit high affinity towards CO_2 molecules in dry as well as humid environments due to chemisorption.[32,33] As a result, amine based adsorbents have gained considerable attraction for CO_2 removal process.[32–42] Therefore, numerous solid supports incorporated with monoamines and/or polyamines with various types of amines (primary, secondary, tertiary) have been extensively studied for CO_2 capture. In

accordance with their physical and chemical features, amine incorporation have been categorized into three classes: impregnation, grafting, and in situ polymerization.[43,44] In class 1, amines such as alkyl chains and polyamines are impregnated (physically, van der Waals bond) into the pores of solid supports. Amines such as alkoxysilane grafted (chemically bonded, co-valent bond) on the surface of solid supports is considered as class 2 whereas class 3 consist of in situ polymerization of amine monomers in the pores of solid supports.

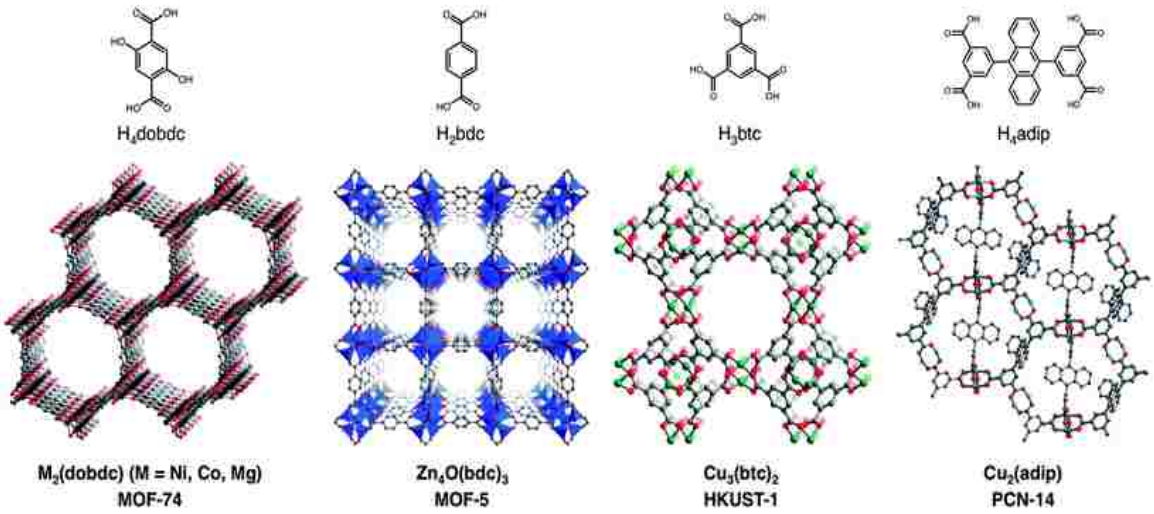

Figure 1.5. Chemical structures of metal organic frameworks.[45]

Metal-organic frameworks (MOFs) have proven to be a potential candidate for numerous applications such as gas adsorption, storage, separation, catalysis, photocatalysis, supercapacitors, and energy conversion due to their unique properties such as ultrahigh porosity and surface area, controllable pore size, tunable topology, crystalline nature with uniform structures. Another reason of being considered in many active research areas among all the materials is their straightforward design and synthesis which involves of varied metal clusters/ions and organic ligands resulting in various frameworks, as shown

in Figure 1.5.[45] Various MOFs such as MIL-101, HKUST-1, MOF-74, MOF-5, MOF-177, UTSA-16, as example, have been investigated extensively for aforementioned applications.[18,25,28,46–61] Recently, MOFs conversion from metal oxide or double salts have gained considerable attention due to its rapid synthesis process.[62,63]

1.5. CO_2 REMOVAL FROM AIR

In addition to post-combustion capture, adsorption technology can also be employed for DAC. To capture CO_2 from ultra-dilute concentrations (400 ppm) using adsorbents is very challenging and requires a system with superior CO_2 capture strategies with additional considerations to energy consumption and human health.[64] Chemisorbents such as Alkali hydroxides[65], bare and impregnated alkali carbonates[66,67], and most importantly amine-based sorbents[32,37,68–70] are highly favored for DAC technologies since physisorbents exhibit poor capture capacity at low CO_2 partial pressure. For continuous DAC process, large scale applications using chemisorbents are still limited by energy intensive regeneration processes. Therefore, development of DAC technologies using physisorbents have been taken into consideration. Kumar *et al.*[71] investigated the effect of water vapor on CO_2 capture from air using physisorbent materials such as zeolite-13X, MOF-74(Mg), HKUST-1, SIFSIX-3(Ni) and TEPA-SBA-15. The authors demonstrated that all adsorbents exhibited high CO_2 capacity, however, influence of water vapor diminished CO_2 uptake. Although capturing CO_2 from air have undergone extensive studies, more investigation is required to develop technologies with more practical and scalable approach.

1.6. CO_2 REMOVAL FROM ENCLOSED ENVIRONMENTS

In sealed environments, an energy-efficient system using promising adsorbents such as amine based sorbents, zeolites and MOFs is highly favored for CO_2 capture.[72–74] Briefly, the current-state of art of CO_2 removal technologies in NASA's International Space Station (ISS) and submarines consist of solid amine-based system using multiple beds. In particular, CO_2 is first adsorbed in the adsorber bed while the removal of CO_2 is achieved in the other bed via supplying heat or vacuum. A multi-level optimization for design of solid amine was investigated by Rong et al.[71] for closed systems. The continuous process of CO_2 removal from closed breathing environments requires an efficient technology consisting of promising adsorbents with significant CO_2 sorption capacity, high stability and regenerability. Solid sorbents such as zeolite 13X and zeolite 5A have proven to be potential candidates, however, drawbacks such as particle attrition, corrosion, pressure drop have hampered their implementation onboard.

1.7. STRUCTURED ADSORBENTS FOR CO_2 CAPTURE APPLICATION

Adsorbents that are commonly produced in traditional configuration (powder form), when implemented into practical and scalable CO_2 capture technology, result in issues such as attrition, high pressure drop and slow mass transfer. In turn, all promising adsorbents such as zeolites, amine based sorbents and MOFs have been shaped into traditional configurations such as beads, granules, pellets and laminates.[16,75–78] However, the implementation of traditional configurations to large scale applications have failed to deliver superior CO_2 adsorption strategies due to associated issues such as particle attrition, pressure drop, low diffusivity and poor heat and mass transfer and loss of adsorbents

because of dusting which have led researchers to investigate other shaping strategies for the development of practical and scalable CO_2 capture technology.[78]

For example, the primary CO_2 removal system, Carbon Dioxide Removal Assembly (CDRA) for international space station (ISS) consists of duel-bed filled with pellets of zeolite where one bed (adsorbent bed) adsorbs CO_2 from the cabin air while the other bed (desiccant bed) desorbs previously accumulated CO_2 to space vacuum. The cabin air is first flowed through desiccant bed to avoid moisture exposure to zeolite. The moisture free air then flowed through the motive blower into zeolite bed. This dual-bed system requires high maintenance due to zeolite pellets attrition increases pressure drop in the fixed bed indicate the poorer performance of traditional packing system.[79]

To address the issues associated with traditional packing system, an engineered geometry termed as ‘monolith’ with uniform channels has gained a great deal of attention due to its configuration consisting of parallel flow channels that allow even flow distribution throughout the system resulting in lower pressure drop and better heat and mass transfer. Also, the additives used in monolith preparation can often enhance the mechanical strength of the monoliths which can eventually prevent attrition and dusting issues commonly encountered in traditional packing systems such as pellets and beads.

Critical aspects of developing robust monolithic contactors fall into formulation by considering factors such as wall thickness, cell density (measured in terms of cells per square inch, cpsi) and cell spacing that influence the processing requirements.[16] For example, combination of wall thickness with appropriate cell density and shape (round, oval etc.) can result in a superior and constructive system with very high mechanical strength, less attrition, rapid heat and mass transfer, low diffusivity resistance and less

pressure drop when compared to traditional packing system. These factors influencing process requirements result in constructive and superior CO_2 capture strategies for industrial-scale applications.

1.8. PREPARATION OF MONOLITHIC ADSORBENTS

Traditional preparation of commonly used monoliths in adsorption and catalysis processes is performed via two methods, namely, coating and self-standing.[78,80] In coating method, the bare monolithic substrate (mostly cordierite) is coated with an active adsorbent using various well developed coating methods such as wash coating[81,82], in situ coating[83], layer by layer (LBL) coating[84] or hydrothermal coating.[85,86] Most recently, Rezaei *et al.*[87] evaluated CO_2 adsorption performance of cordierite monoliths coated with MOF-74(Ni) and UTSA-16(Co) and demonstrated that monoliths with MOF loading as high as 52 and 55 wt. % on cordierite exhibited high affinity towards CO_2 relative to N_2. Moreover, Lawson *et al.*[88] enhanced MOF-74(Ni) and UTSA-16(Co) loading up to 73 and 80 wt. %, respectively, on cordierite by impregnating a polymer on the support and achieved higher CO_2 capacity. A limitation in adsorption capacity from coated monoliths was observed as the substrate does not contribute to CO_2 adsorption capacity and eventually results in very low CO_2 uptake. High loading of active components on the support also lead to poor heat and mass transfer and pressure drop. In addition, adhesion of active component while transportation is a major problem associated with coated monoliths.

To address the known issues associated with coated monoliths, manufacturing of self-standing monoliths using extrusion technique have been extensively studied over two decades. An extrusion technique is a continuous process where an adsorbent is introduced with additives such as binder and plasticizer materials to obtain monolithic form with

desired structural, mechanical and physical properties. In particular, binders are used for binding the adsorbent particles whereas adhesion is carried out by plasticizer between binder and adsorbent particle. Appropriate solvent is also used to obtain homogeneity of the paste while monolith preparation. Upon achieving the homogeneity, the paste is forced through constrained spaces or custom made dies. Large volume of monoliths with channels can be manufactured using extrusion technique. Despite their precise fabrication, extrusion technique entails major drawbacks such as swelling of die, energy intensive, availability of complex parts and limitation of certain cross-sectional shape or product limitations. Hence, it is difficult to fabricate monoliths with various channel size, wall thickness and density.

1.9. 3D-PRINTING TECHNIQUE FOR MONOLITH PREPARATION

3D printing or robocasting (additive manufacturing) technique has gained immense importance in energy and environmental applications over extrusion technique to fabricate solid materials.[89–91] Robust monoliths with desired wall thickness, channel size and density can be precisely fabricated by varying and optimizing the additives using 3D printing technique, as shown in Figure 1.6. Particularly, an external parametric diameter with appropriate cell density and shape (round, oval etc.) can be set for monolith preparations. In addition, channel size and wall thickness can be modified by using various sizes of extruding syringe (from 2 μm to 50 μm). To fabricate adsorbent monoliths in large size (10 cm x 10 cm), different tube sizes ranging from 3 mL to 50 mL, could be used. Moreover, the extrusion is carried out by supplement of air, which can be controlled using air flow controller, by varying force from 1 bar to 5 bar depending on the viscosity of the paste. Therefore, channel size and wall thickness can be altered by adjusting air flow. Various shapes can also be easily designed by AUTOCAD software which is required to code via

(Slic3r) software. In short, the Robocasting or 3D printing technique found to be a facile approach to fabricate monoliths with controlled channel size, wall thickness and density.

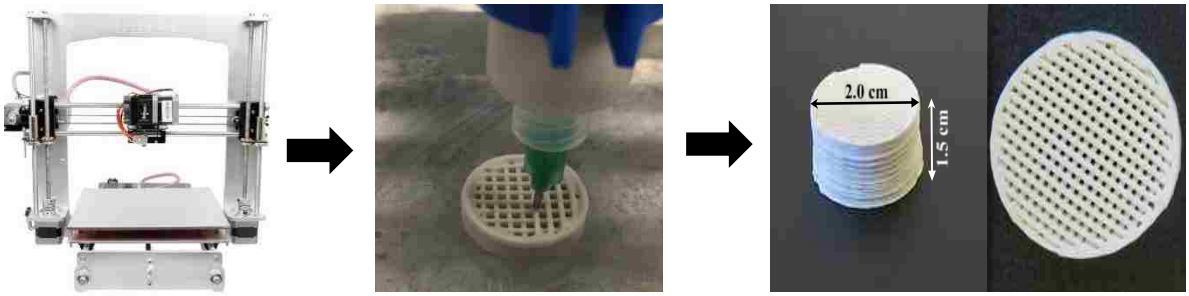

Figure 1.6. Image of (a) Geeetech Prusa I3 3D printer (b) paste extrusion using 3D printing in monolithic geometry (c) cross-sectional of 3D printed monoliths.

2. RESEARCH OBJECTIVES

The overall objective of this work is to engineer advanced gas-solid contactors for use in CO_2 capture processes. The specific objective are as follows:

1) Develop and optimize monolithic structures from zeolite, aminosilica, and MOF adsorbents using 3D printing technique.

2) Assess the structural, physical, and mechanical properties of 3D-printed monolithic adsorbents by various characterization techniques.

3) Evaluate adsorption performance of monolithic adsorbents and compare with their corresponding powders using equilibrium and dynamic adsorption techniques.

4) Develop cost-effective adsorbents from bentonite clay and post-functionalize them with amines for use in CO_2 capture.

PAPER

I. 3D-PRINTED ZEOLITE MONOLITHS FOR CO_2 REMOVAL FROM ENCLOSED ENVIRONMENTS

Harshul Thakkar[1], Stephen Eastman[1], Amit Hajari[1], Ali A. Rownaghi[1], James C. Knox[2], Fateme Rezaei[1*]

[1]Department of Chemical & Biochemical Engineering, Missouri University of Science and Technology, Rolla, MO 65409-1230, United States
[2]George C. Marshall Space Flight Center, National Aeronautics and Space Administration, Huntsville, Alabama 35812, United States

ABSTRACT

Structured adsorbents especially in the form of monolithic contactors offer an excellent gas-solid contacting strategy for development of practical and scalable CO_2 capture technologies. In this study, the fabrication of 3D-printed 13X and 5A zeolite monoliths with novel structures and their use in CO_2 removal from air are reported. The physical and structural properties of these printed monoliths are evaluated and compared with their powder counterparts. Our results indicate that 3D-printed monoliths with zeolite loading as high as 90 wt% exhibit comparable adsorption uptake to powder sorbents. The adsorption capacities of 5A and 13X monoliths were found to be 1.59 and 1.60 mmol/g, respectively using 5000 ppm (0.5%) CO_2 in nitrogen at room temperature. The dynamic CO_2/N_2 breakthrough experiments show relatively fast dynamics for monolithic structures. In addition, the printed zeolite monoliths show reasonably good mechanical stability that can eventually prevent attrition and dusting issues commonly encountered in traditional pellets and beads packing systems. The 3D printing technique offers an alternative cost-effective and facile approach to fabricate structured adsorbents with tunable structural, chemical and mechanical properties for use in gas separation processes.

Keywords:
3D-printed monolith, enclosed environments, CO_2 removal from air, adsorption

1. INTRODUCTION

In enclosed environments such as spacecraft or submarine cabins, CO_2 level should be below 0.5% as long-term exposure to CO_2 of higher than this level can cause severe health problems such as fatigue, listlessness, malaise, mood changes and headache.[1,2] Therefore, removal of CO_2 from cabin atmosphere is a critical function of any spacecraft's or submarine's life support system.[3] In addition, the removal of CO_2 from indoor air in commercial buildings is gaining significant attention among researchers primarily due to the health risks associated with high CO_2 concentration level as a results of inadequate ventilation.[4,5]

The removal of ultra-dilute CO_2 (ppm level) from enclosed atmosphere is more challenging and energy-intensive than CO_2 capture from other industrial gas streams in which CO_2 concentration is typically above 5 vol%. This is due to the low concentration-gradient driving force for adsorption at extremely dilute conditions. Moreover, additional considerations related to human health should be taken into account when developing technologies for CO_2 capture from enclosed environments. This is particularly important for spacecraft or space stations where attrition of the adsorbent particles or the release of some toxic chemicals from can pose serious health problems to astronauts.[6,7]

The current state-of-the-art systems for cabin CO_2 removal in such systems utilize fixed beds of adsorbent pellets or beads. These adsorbents are mainly zeolite 13X or 5A molecular sieves which are commonly used as benchmark adsorbents for CO_2 capture from flue gas streams.[8,9] As a result of high particle attrition rate, pressure drop builds up in the

fixed bed which increases the blower power required to maintain flow and eventually requiring highly undesirable system maintenance. Dust fines generated from the attrition propagate downstream and can accelerate failure rates in downstream components.[6] To reduce flow resistance through the fixed bed, pelletization of adsorbent particles with clay binder (or binderless pellets) is required. Such pellets are highly porous structures allowing rapid mass transfer through the pellet. However, this open composite structure tends to have low resistance to attrition and may be weakened by humidity and/or large temperature excursions. Moreover, dusting due to the particles attrition in enclosed environments can lead to human health problems such as pneumoconiosis.[10] To improve CO_2 removal system efficiency and reliability, more robust and highly efficient adsorbent structures are required.

To overcome the limitations associated with the traditional configurations, adsorbent particles could be shaped into other configurations such as monolithic structures that offer substantial advantages compared to conventional packing systems like pellets, beads or granules.[11–13] Such well-designed robust contactors have been shown to improve the overall performance in terms of pressure drop and mass and heat transfer characteristics that eventually translate into a low-cost and more efficient capture technology while addressing the drawbacks of conventional packing systems. Monoliths are structured materials with parallel gas flow channels in which the shape and the diameter of the parallel channels and their density per cross sectional area of the monolith are controllable. A particularly challenging aspect to shape adsorbents into monolithic contactors is the trade-off between key design parameters such as active adsorbent loading, mass and heat transfer properties, and cell density (cpsi). While higher adsorbent content per unit volume is

desirable to achieve higher uptake, the kinetics of adsorption tends to become slower as a result of limited accessibility to adsorption sites in thicker walls. In addition, high cell density monoliths that maximize active adsorbent loading and surface area are preferred but pressure drop through the narrow channels is substantially higher than through low cell density monoliths.[14]

In recent years, monolithic adsorbents made of activated carbon, zeolites, and metal-organic frameworks (MOFs) have received considerable attention for use in adsorption systems.[15–26] More specifically, cordierite monoliths washcoated with a thin layer of 13X zeolite have been investigated experimentally and numerically for CO_2 capture from flue gas.[11,14,27,28] For these coated substrates, although the mechanical strength is reasonably good, the ceramic support does not contribute to CO_2 adsorption, hence limiting the active adsorbent amount per unit volume. On the other hand, self-standing supports for which the active adsorbent constitutes the major portion of the structure have also been investigated.[29–31] For these structures, the adsorbent is mixed with a binder and small amount of plasticizer or other additives to form the monolith. Hasan et al.[30] reported the development of 5A zeolite monoliths with zeolite loading of 92 wt% for use in CO_2 capture applications. The authors used a custom made die to fabricate monoliths with hierarchical pore network. Ojuva et al.[31] prepared NaA zeolite monoliths by freeze-casting suspension of method and evaluated their CO_2 adsorption performance and mechanical stability. The lamellar structure of the freeze-casted monoliths exhibited sharp CO_2 breakthrough fronts.

Literature data on the application of monolithic adsorbents in CO_2 removal from air are very scarce. A process level and economic analysis of the application of amine-modified honeycomb monoliths for direct capture of CO_2 from air was performed by Kulkarni and

Sholl.[32] Most recently, Sakwa-Novak et al.[33] reported the impregnation of poly(ethylenimine) (PEI) into monolithic alumina honeycombs and their use for CO_2 capture from air. A volumetric capacity of 350 mol CO_2/m^3-monolith was reported for the removal of 400 ppm CO_2 in N_2.

Traditionally, monoliths are fabricated using the conventional extrusion process. Most recently, 3D printing techniques are in-demand for fabricating complex geometries with unique mechanical and structural properties. Notably, these techniques allow for precisely fabricating three-dimensional devices with desired configurations and optimized properties, as opposed to conventional extrusion processes.[34] High productivity and low fabrication cost are other noticeable advantages of these methods. By employing 3D printing technique, it is possible to fabricate monoliths with various cross-sections, channel sizes, and wall thicknesses. More importantly, the fabrication parameters could be tuned to obtain parts with high mechanical properties. Most recently, the 3D printing technique was used to fabricate heterogeneous Cu/Al_2O_3 catalysts for different Ullmann reactions.[35] The 3D-printed catalysts showed high catalytic efficacy and good recyclability.

This proof-of-concept study describes fabrication of 3D-printed 5A and 13X zeolite monoliths and their use in CO_2 removal from air. The printed structures were physically and structurally characterized and then evaluated for equilibrium and dynamic CO_2 capture from air. We hypothesize that the 3D-printed zeolite monoliths exhibit excellent mechanical and adsorption properties that render them as suitable candidates for not only CO_2 removal from enclosed environments but also for other adsorption and separation processes.

2. EXPERIMENTAL SECTION

2.1. PREPARATION OF ZEOLITE MONOLITHS

Self-standing zeolite monoliths were prepared from zeolite 13X and 5A powders (UOP), bentonite clay (Sigma Aldrich) as a binder, methyl cellulose (Thermo Fisher), as a plasticizing organic binder, and poly(vinyl) alcohol (PVA, Sigma-Aldrich) as a co-binder. Methyl cellulose contains hydroxyl groups that contributes to additional particles cohesion while playing an important role in the monolith strength. A desired amounts of these powders were first mixed using a high-performance dispersing instrument IKA-R25 at 2500 rpm. After obtaining a homogeneous powder mixture, a sufficient amount of distilled water was added and mixed rigorously using the IKA-R25 at 2500 rpm until a homogenous aqueous paste with suitable viscosity was produced. The paste was loaded into a syringe (3 mL, Norson EFD, USA) attached to a nozzle with a 0.60 mm diameter. In the next step, the paste was extruded through the moving nozzle in a Robocasting 3D printer (3D Inks, Stilwater, USA). In this method, the printed product was first designed by the software RoboCAD 4.2 that controlled the printer motion and then the paste was deposited in a layer by layer fashion with layers having perpendicular to each other.[36] The well-defined structures with uniform channels and layers thickness could be obtained by this technique. Figure 1 shows the cylindrical zeolite monoliths with square channels and smooth surfaces fabricated by the 3D printer.

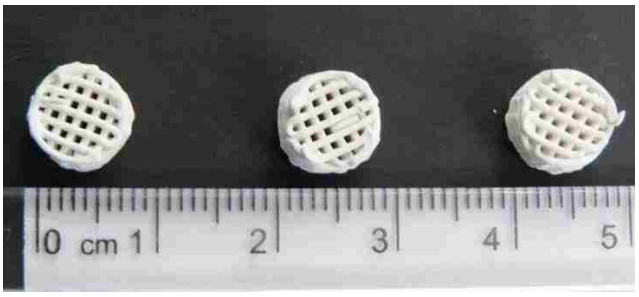

Figure 1**.** Self-standing zeolite 13X monoliths extruded by Robocasting 3D printer.

After the monolithic structures were printed, they were initially dried at room temperature to partially remove water content. The pieces were then placed into an oven and heated at 100 °C to remove the rest of water and allow the polymer linker (PVA) and methyl cellulose to quickly build up high strength and avoid skin cracking. After drying in the oven, the monoliths were calcined (sintered) at 700 °C at the rate of 20 °C/min in a temperature-controlled furnace for 2-4 h in order to decompose and remove the co-binders, methyl cellulose and PVA. This calcination step removes the organic content and results in increasing the mesoporosity in addition to enhancing the mechanical strength of the final calcined monolith. To investigate the mechanical stability and CO_2 adsorption performance of monolithic structures, zeolite 13X and 5A monoliths were prepared by varying the zeolite to binder weight ratio, co-binder and plasticizer concentrations, as listed in Table 1.

Table 1. Compositions of the fabricated 3D-printed 13X and 5A zeolite monoliths.

Monolith	**Zeolite (wt %)**	**Bentonite clay (wt %)**	**Methyl cellulose (wt %)**	**PVA (wt %)**
R2	80	15	3.5	1.5
R3	85	10	3.5	1.5
R4	90	7	2.0	1.0

2.2. CHARACTERIZATION OF ZEOLITE MONOLITHS

N_2 physisoprtion isotherms were collected at 77 K using a Micromeritics 3Flex gas analyzer to investigate the textural properties of the zeolites in both powder and monolith forms. All samples were first degassed on a Micromeritics PreVac at 350 °C for 8 h before measurement. The obtained isotherms were used to evaluate the surface area pore volumes, and pore size distribution (PSD). The X-ray diffraction (XRD) measurements were conducted using PANalytical X'Pert Multipurpose X-ray Diffractometer with scan step size of 0.02^o/step at the rate of 147.4 s/step. Structural morphology was studied by Hitachi S4700 Field Emission Scanning Electron Microscopy (SEM). In order to obtain cross sectional view in SEM, monolith structures were placed horizontally on the sampler holder and their height was adjusted accordingly. To measure the residual binder content that remains in the monolith after calcination, TGA-DSC was carried out from 25 to 700 °C at the rate of 20 °C/min using TGA (Q500, TA Instruments).

2.3. MECHANICAL TESTING

Mechanical testing was carried out using an Instron 3369 (Instron, Norwood, USA) mechanical testing device. Initially, monoliths were polished with a 3M surface smoothing sand paper to prevent uncertain surface and to avoid cracks on the surface for achieving effective results. After polishing, the monolith was placed between two metal plates and compressed with 500 N load cell at 2.5 mm/min while the applied load and piston movement was recorded, following the ASTM D4179–01 (standard test method for single pellet crush strength of formed catalyst shapes) procedure.[37] The compressive force was applied until the monolith broke.

2.4. ADSORPTION CAPACITY MEASUREMENTS

TGA (Q500, TA Instruments) was utilized to measure CO_2 capacity under ultra-dilute capture conditions. To drive off the pre-adsorbed gases, moisture or any other impurities, commercial powders and synthesized monoliths were first degassed at 400 °C under N_2 with the flow rate of 40 mL/min. CO_2 capture uptake measurements were then carried out at room temperature by exposing the samples to 0.5% CO_2 in N_2. In addition, the CO_2 and N_2 adsorption isotherms for R4 monoliths and their powder counterparts were measured by 3Flex at 25 °C.

2.5. CO_2 BREAKTHROUGH EXPERIMENTS

The breakthrough experiments were performed in a small-scale fixed-bed column coupled with a BEL-Mass spectrometer (MS). The schematic of the setup could be found in our previous publication.[38] The feed stream with the composition of 0.5% CO_2/N_2 was fed into the column at the flow rate of 60 mL/min. Prior to each sorption experiment, the bed was heated to 400 °C under flowing N_2 at 60 mL/min for 2 h to desorb adventitious CO_2 and water, then cooled to 25 °C and exposed to CO_2 for the experimental sorption run. The effluent composition exiting the column was transiently measured by the MS and after reaching the inlet concentration, desorption step was started by flowing N_2 to the column at the same flowrate (*i.e.,* 60 mL/min).

3. RESULTS AND DISCUSSION

3.1. PHYSICAL PROPERTIES OF 3D-PRINTED MONOLITHS

N_2 physisorption isotherms and the corresponding pore size distribution curves, displayed in Figure 2, were used to assess the porosity of the monoliths and their powder analogues. For monolithic sample, the isotherms show an initial steep uptake at low partial pressures (P/P_0) between 0.0 and 0.05 corresponding to the adsorption in the micropores,

followed by a gradual increase with hysteresis at high P/P_0 indicative of capillary condensation in mesopores.[28,29] The N_2 isotherms for 3D-printed 13X and 5A monoliths are of type IV isotherm shape while the powder zeolites displayed a typical type I isotherm shape characteristic of microporous materials.[17]

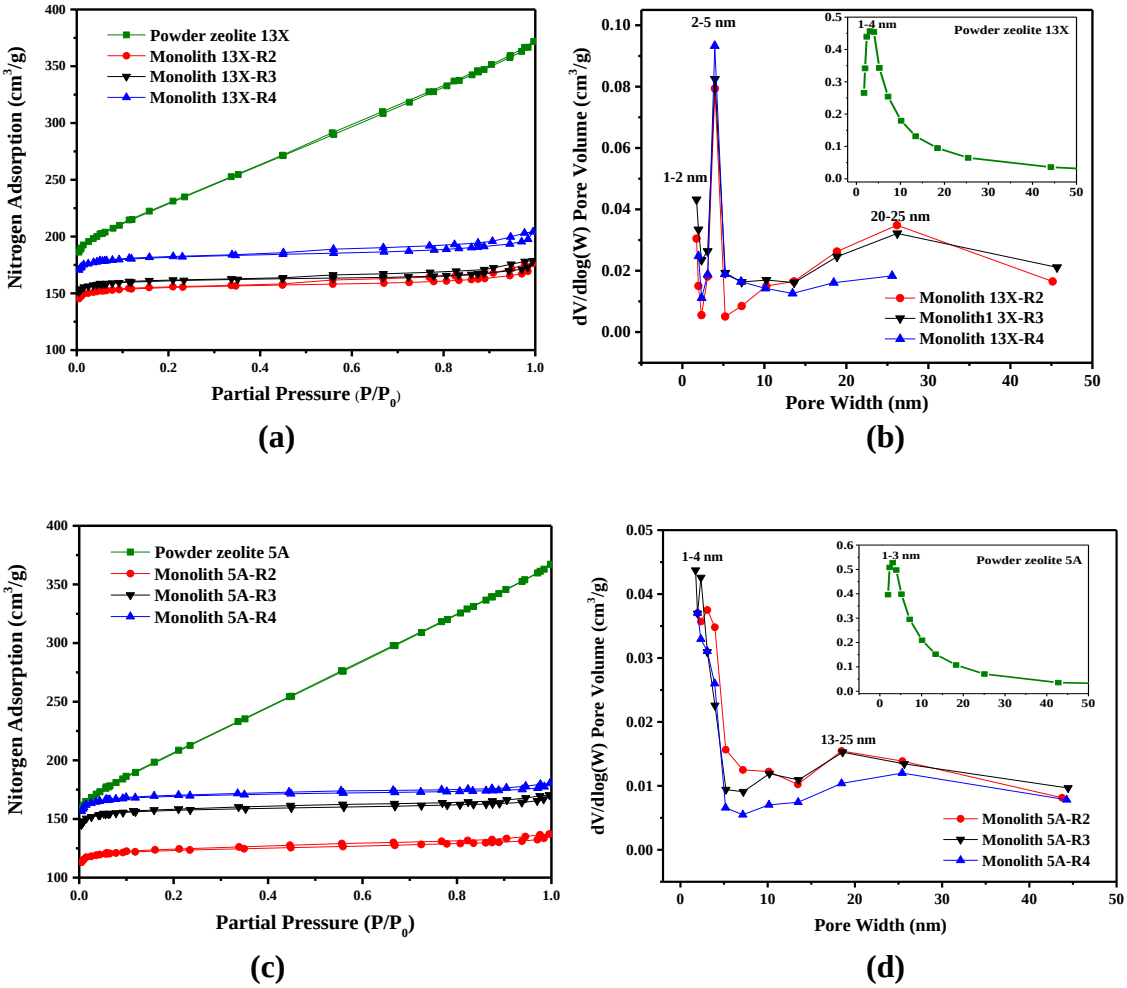

Figure 2. N_2 physisorption isotherms and pore size distribution for of 3D printed monoliths and powders for (a-b) 13X and (c-d) 5A zeolites, respectively. Pore size distribution derived from the DFT method using the desorption branch of the N_2 isotherm.

The size of the micropores calculated using the DFT method was 1.06 nm for 13X-R4 and 1.07 nm for 5A-R4 monoliths (Table 2). For all materials, the first peak appears in the

range from 0.5 to 2 nm which corresponds to micropore range. For 13X-R2 and 13X-R3 zeolite monoliths, the meso-sized pores were obtained in the range of 150-170 nm and 100-120 nm, respectively. This difference in the mesopore size distribution may be attributed to short heating and stirring time.[25] As expected, shaping zeolite particles into a self-standing monolith configuration using 3D printing method introduces mesoporosity into the structure. In addition, the formed mesopores in the monolith R2 monoliths are bigger in size than in the R3 and R4 monoliths mainly due to the smaller amounts of binder and plasticizer in the later samples.

Table 2 summarizes the BET surface area, micropore and mesopore volumes, and the corresponding diameters of 3D-printed monoliths and zeolite powders. The BET surface areas of 13X-R4 and 5A-R4 monoliths were found to be 635 and 543 m^2/g, respectively whereas the micropore volumes (at $P/P_0 = 0.99$) were calculated to be 0.24 and 0.25 cm^3/g, respectively, all of these values were relatively lower than those for zeolite 13X and 5A in the powder form, as expected as a result of lower zeolite content. The data presented in Table 2 show that the characteristics of the 13X and 5A monoliths were very similar. Although increasing the binder content resulted in reduced BET surface area and micropore volume, the mesopore volume increased with binder content. Notably, the mesopore volume of 13X monolith was higher than that of 5A monolith with similar composition (0.05 compared to 0.06 cm^3/g). It should be noted here that for the rest of our analysis we only focused on the monoliths with highest zeolite loading (R4) and compared their characteristics with their powder counterparts.

Table 2. N_2 physisorption data for 3D-printed monoliths and zeolite powders.

Sample	**S_{BET}[a]** (m^2/g)	**V_{micro}[b]** (cm^3/g)	**V_{meso}[c]** (cm^3/g)	**d_{microo}[d]** (nm)	**d_{meso}[d]** (nm)
Powder zeolite 13X	770	0.31	-	1.06	-
Monolith 13X-R2	498	0.22	0.020	1.06	2.5, 4, 6.3, 7.8
Monolith 13X-R3	517	0.25	0.018	1.06	2.8, 3, 3.6, 4.2, 6.8
Monolith 13X-R4	571	0.26	0.012	1.06	4.3
Powder zeolite 5A	705	0.29	-	1.07	-
Monolith 5A-R2	395	0.18	0.014	1.07	2.6, 3.2, 3.8, 4, 6.7
Monolith 5A-R3	504	0.23	0.012	1.07	2.8, 3.6
Monolith 5A-R4	543	0.25	0.009	1.07	2.5, 3.2

[a] Obtained at P/P_0 in the range of 0.05-0.3. [b] Estimated by t-plot. [c] Estimated by subtracting V_{micro} from the total volume at $P/P_0 = 0.99$. [d] Estimated using Horvath–Kawazoe method.

After forming paste, the function of plasticizer is no longer necessary and to achieve better mass transfer and the formation of secondary pore structure, removal of plasticizer is processed by calcination. Upon calcination, the organic content of the monolith (*i.e.*, methyl cellulose and PVA) was removed rendering the calcined monoliths containing zeolite and binder particles only. To verify this, the amounts of zeolite and bentonite clay were quantified by TGA. Figure 3 displays the mass degradation of as-synthesized (uncalcined) and calcined zeolite monoliths (highly loaded R4) obtained from TGA-DSC. The TGA data of methyl cellulose and PVA shown in Figure 3c, d, display a weight loss step at 360°C and 275°C, respectively. On the basis of these profiles, we believe that the weight losses below 200 °C correspond to moisture desorption. For uncalcined monoliths, the other weight losses appearing between 200 °C and 700 °C are associated with the

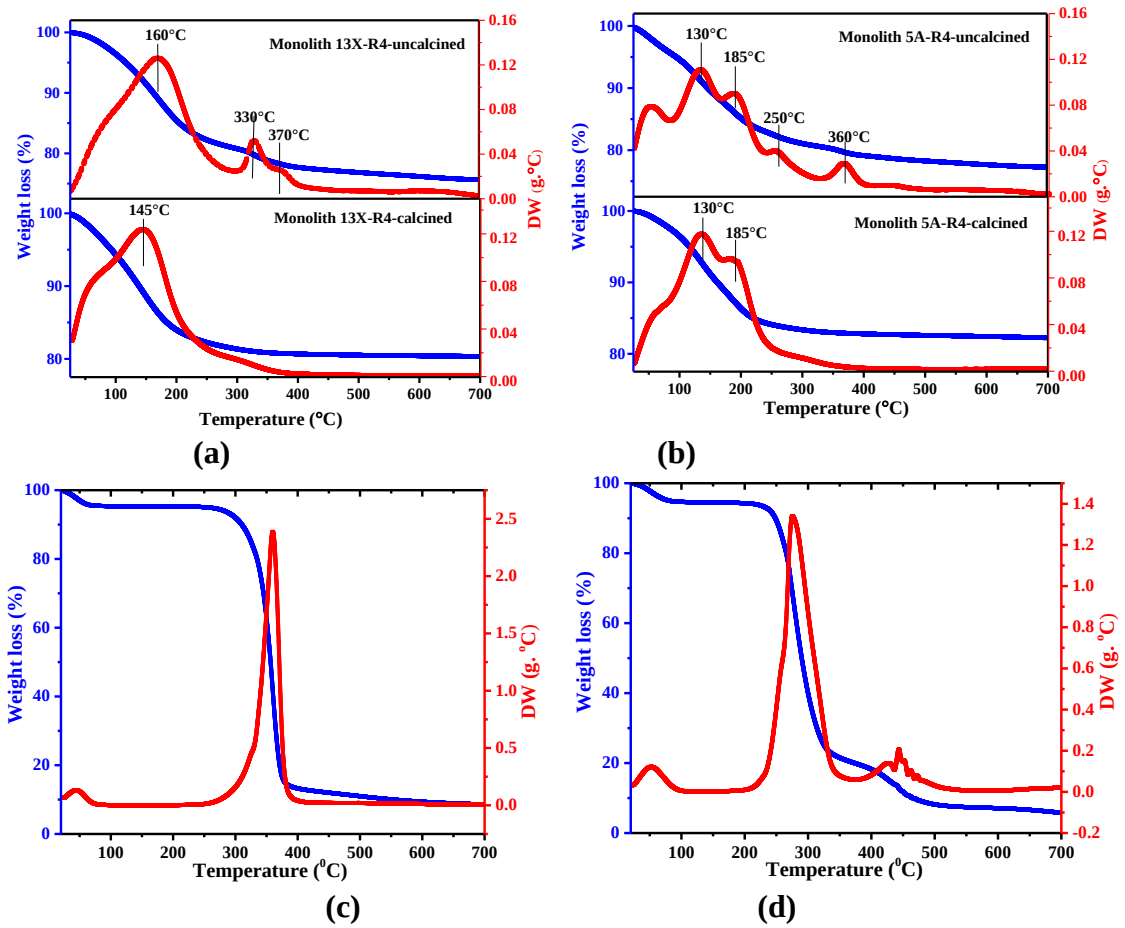

Figure 3**.** Thermogravimetry and differential thermogravimetry curves for uncalcined and calcined (a) 13X-R4, (b) 5A-R4 zeolite monoliths, (c), methyl cellulose and (d) PVA.

decomposition of organic additives, whereas for calcined samples, small weigh losses could be attributed to the loss of organic compounds that had been trapped in the pore network during sintering process and still existed in the structure after calcination. The total weight loss between 200 °C and 700 °C was 10 wt% and 8 wt% for uncalcined 13X-R4 and 5A-R4 calcined monoliths, respectively, while both samples exhibited ~4 wt% weight loss after calcination. The later implies that the total weight of zeolite and permanent binder (bentonite clay) in the final monoliths is ~96 wt% which is close to the nominal weight fractions used in the preparation step (see Table 1).

3.2. STRUCTURAL PROPERTIES OF 3D-PRINTED MONOLITHS

Figure 4 displays the XRD patterns of 13X-R4 and 5A-R4 zeolite monoliths after calcination along with their powder counterparts. As shown in this Figure, the good crystallinity of the zeolites was retained although slight differences in the peak intensities can be observed in the XRD patterns of 3D-printed monoliths with 90 wt% zeolite loading.

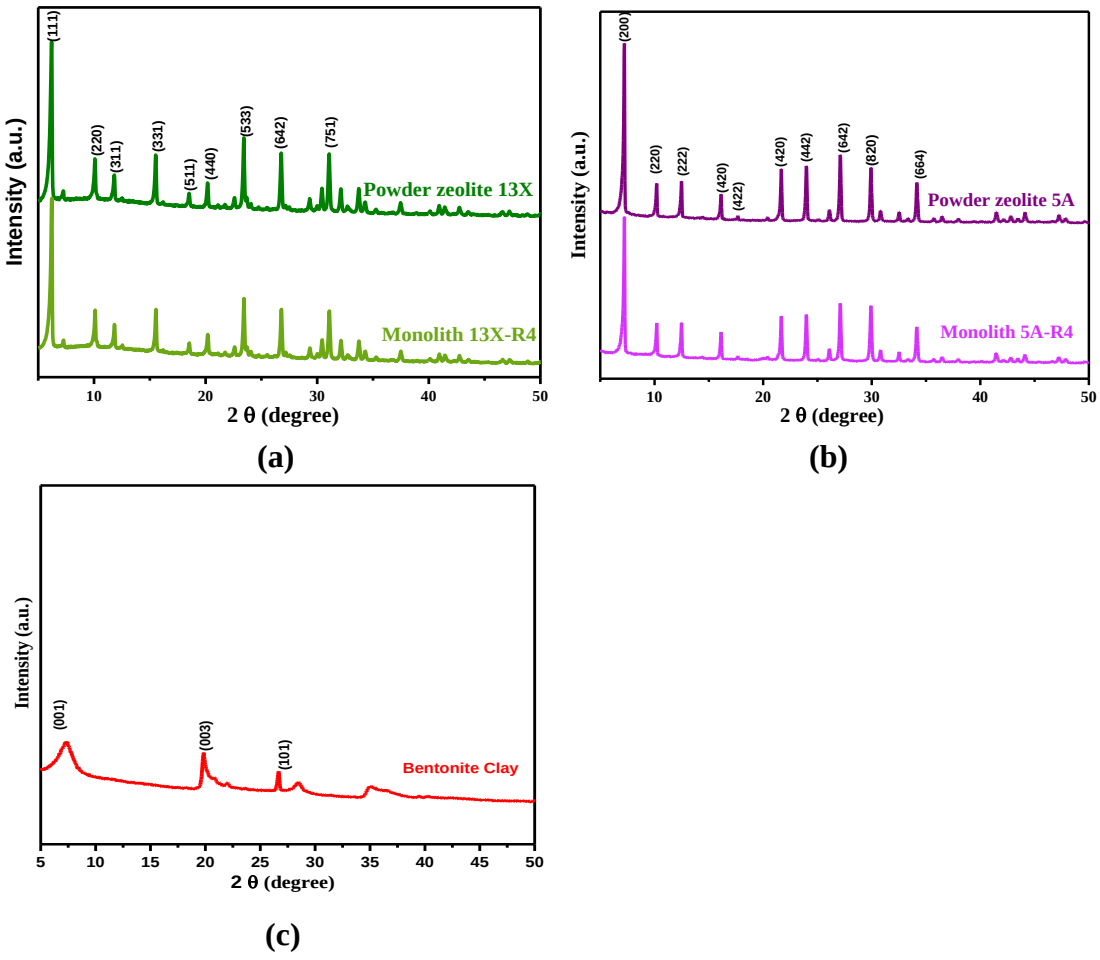

Figure 4. (a) XRD patterns of the calcined 3D printed monoliths and powders for (a) 13X, (b) 5A zeolite, and (c) bare bentonite clay (permanent binder).

This could be attributed to the presence of the binder (bentonite clay) or the change in the size of zeolite particles as a result of sintering during calcination process. In addition, these patterns reveal that the diffraction peaks of FAU and LTA frameworks were retained in the monolithic structures. The presence of peaks at 2 = 6.2°, 15.6°, and 30.9° in Figure 4a correspond to (111), (331), and (715) planes in FAU framework, respectively whereas the reflections at 2 = 7.2°, 16.1°, and 27.1° in Figure 4b are related to (200), (420), and (642) planes in LTA framework.[39] It is worth mentioning that the low intensity diffractions peaks of bentonite clay appeared at 2 ~ 20 and 27° (Figure 4c) were overlapped with those of zeolites at the same angle.

Low and high magnification SEM images of 13X-R4 and 5A-R4 monoliths prepared by 3D printing technique are presented in Figure 5a-h. The low magnification SEM images shown in Figures 5a and 5e reveal the uniform square channel cross-section of the structures with the wall thickness of ~0.65 mm and channel width of ~0.4 mm for both cases. The magnified views of the channel structures shown in Figures 5b-d and 5f-h clearly illustrate the macroporous nature of the walls with pores on the order of 5-50 μm. These images indicate that the 3D-printed monoliths retained their porous morphology and that the particles sintered together to form a porous network with voids having sizes on the scale of

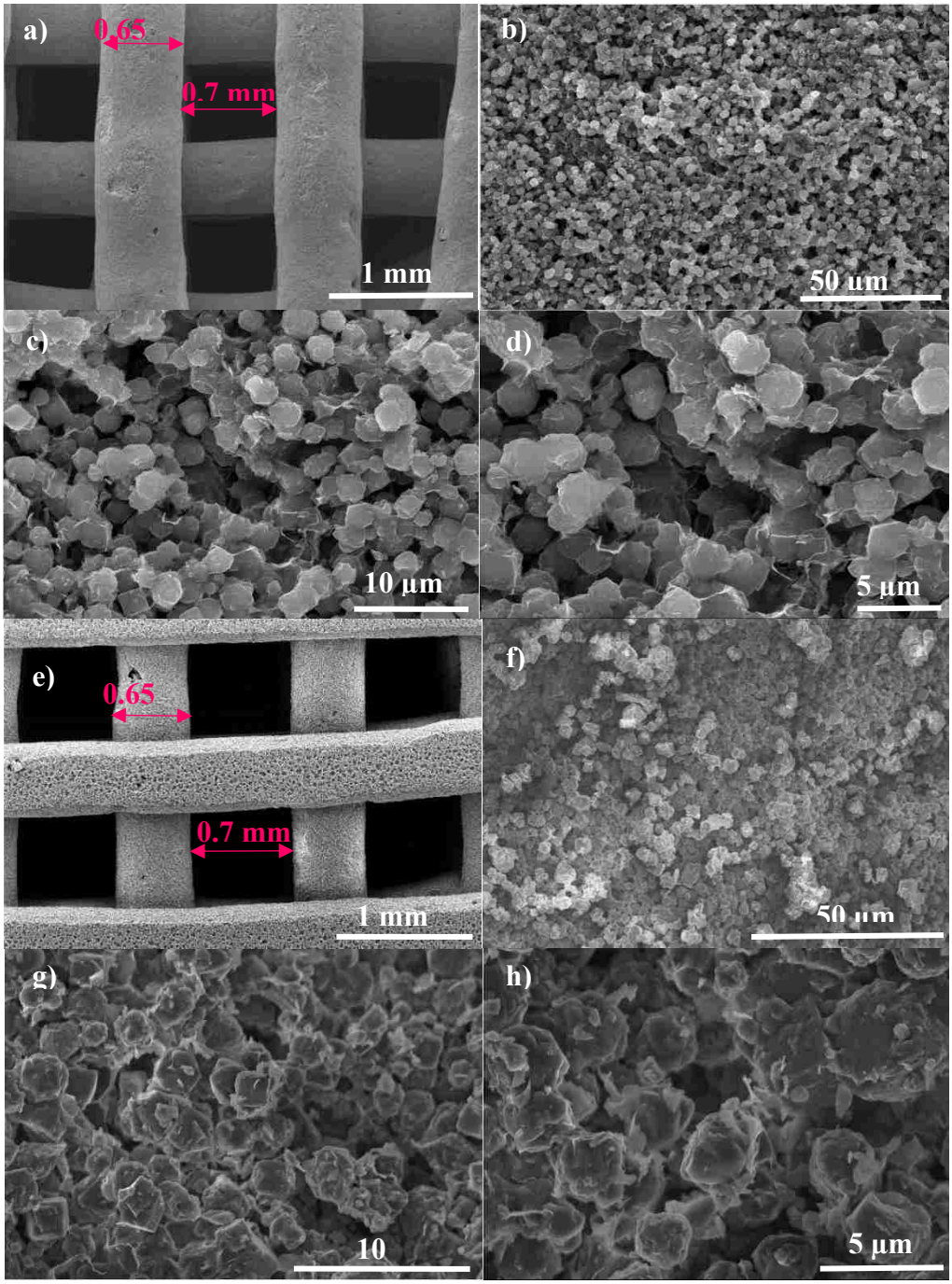

Figure 5**.** SEM images of (a-d) 13X-R4 and (e-h) 5A-R4 3D-printed monoliths.

micrometers. Moreover, it is apparent from these images that the particles distribution was not adversely affected by the paste preparation and printing conditions, and no particles agglomeration could be observed.

3.3. MECHANICAL STRENGTH OF 3D-PRINTED MONOLITHS

The mechanical strength and deformation of the samples was also assessed by compression test and the compressive strength of monoliths as a function of zeolite loading is presented in Figure 6. In addition, the corresponding compressive strength and the average Young's modulus values extracted from these data are presented in Table 3. The trend in Figure 6a suggests the proportional relationship between zeolite loading and compressive strength and also the displacement between particles that the material tend to retain upon loading, relative to the length of the monolith. The 13X-R4 that contains highest zeolite loading (90 wt %) showed maximum compressive strength (0.69 MPa) before catastrophic failure which can be attributed to its porosity and microporous texture.[31,40] Previously, Martin and Brown demonstrated the decrease in compressive strength with porosity for carbonated hydroxyapatite monoliths.[41] Since lower amount of binder and additives were used for preparation of 13X-R4, this monolith is denser than the 13X-R3 and 13X-R2 and its microporous texture requires high compressive force to deform micropore walls as compared to 13X-R3 and 13X-R2. In contrast, 13X-R2 exhibited the lowest compressive strength (0.3 MPa) as a result of higher mesopore volume than other monoliths.

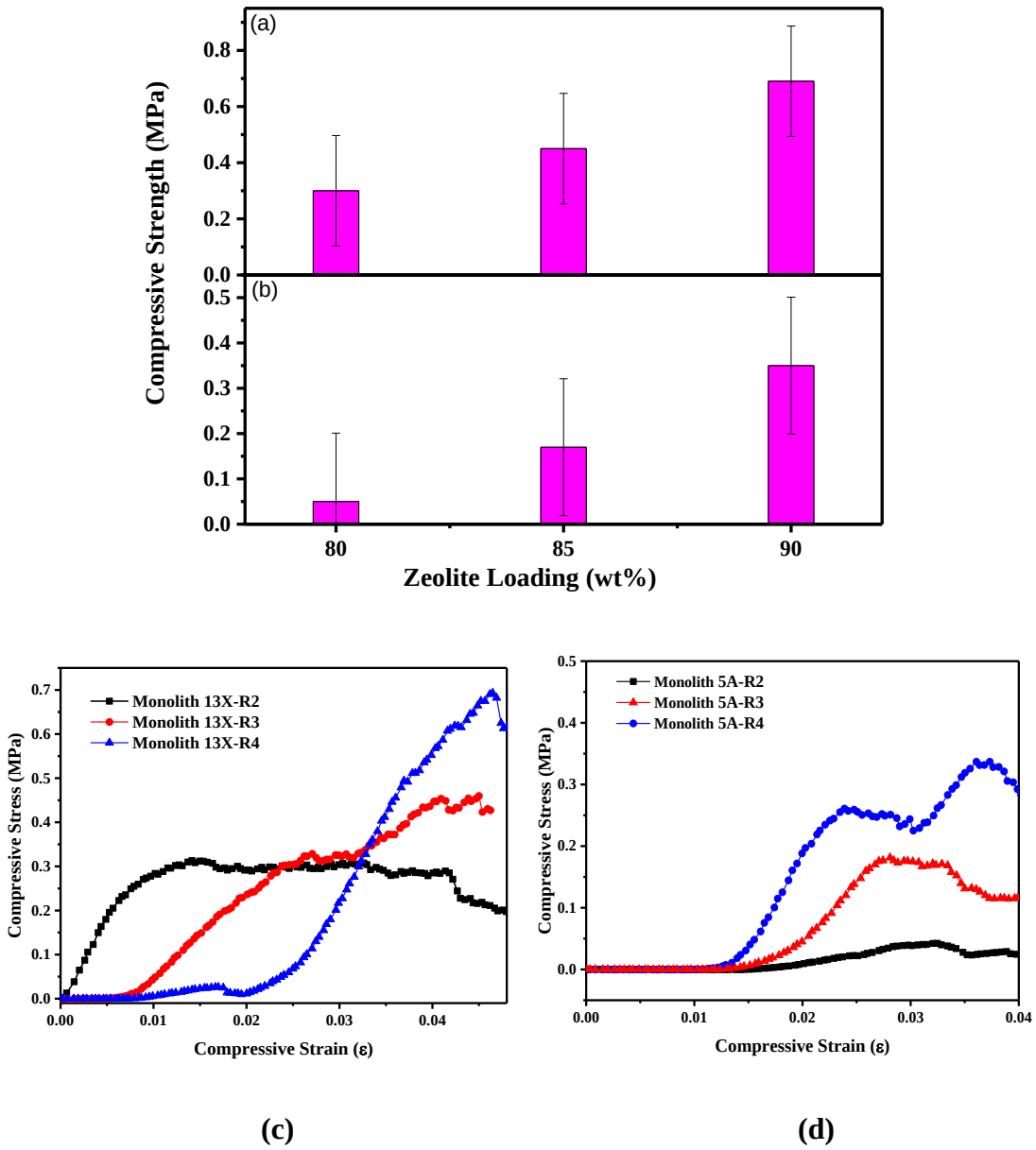

Figure 6**.** Compressive strength versus zeolite loading (wt %) of (a) 13X and (b) 5A 3D-printed monoliths, respectively. Stress-strain curves of 3D-printed monoliths of (c) 13X and (d) 5A.

Figure 6b illustrates the compressive strength of 5A-R2, 5A-R3 and 5A-R4 monoliths. Compressive strength shows similar increasing trend with zeolite loading as for 13X monoliths. However, compressive strength of 5A monoliths were much lower than that of 13X monoliths with the same zeolite loading which could be linked to their less dense

structure. Maximum compressive stress of 0.35, 0.15 and 0.5 MPa were recorded for 5A-R4, 5A-R3 and 5A-R2, respectively (see Table 3). The corresponding stress-strain curves are also shown in Figure 6c, d. Comparing the crush strength of the monoliths with that of 5A pellets used in NASA's CO_2 removal system revealed that the 3D monoliths have higher crush strength than the pellets.[42,43] It should be however noted that the single pellet crush tests on the NASA's 5A pellets were performed under humid conditions which could be a reason for having lower strength.

Table 3. Mechanical testing data for 3D-printed monoliths.

Sample	**Compression strength (MPa)**	**Young's modulus (MPa)**
Monolith 13X-R2	0.30	7.50
Monolith 13X-R3	0.45	10.0
Monolith 13X-R4	0.69	15.0
Monolith 5A-R2	0.05	1.65
Monolith 5A-R3	0.17	5.75
Monolith 5A-R4	0.35	9.45

3.4. EQUILIBRIUM ADSORPTION MEASUREMENTS

The CO_2 adsorption capacity of 3D-printed monoliths was determined by TGA experiments at 25 °C and two different concentrations, namely 0.3 and 0.5% relevant to the CO_2 partial pressure in enclosed environments. The adsorption capacities are displayed in Figure 7. It is evident from this Figure that the zeolite monoliths prepared by 3D printing technique display comparable capacity to the powder zeolites. In particular, for 0.5% CO_2/N_2, 13X-R4 showed a CO_2 uptake of 1.39 mmol/g which is 87% of that of 13X zeolite in the powder form, whereas, 5A-R4 exhibited 89% of the capacity of the 5A powder (1.43 mmol/g). Moreover, as can be seen from these results, increasing the zeolite/binder weight

ratio resulted in the increased CO_2 adsorption capacity. This expected proportional CO_2 adsorption to zeolite loading in monolithic adsorbents could be attributed to the fact that equilibrium adsorption mainly takes place in micropores of the monoliths. Analyzing the micropore volumes of monoliths obtained from N_2 physisoprtion (Table 2) and CO_2 adsorption capacities (Figure 7), it follows that the difference in adsorption uptake of monoliths are proportional to the difference in their micropore volumes. For instance, the adsorption capacity of 5A-R4 was 1.12 times higher than that of 5A-R3 while its micopore volume was 1.10 higher.

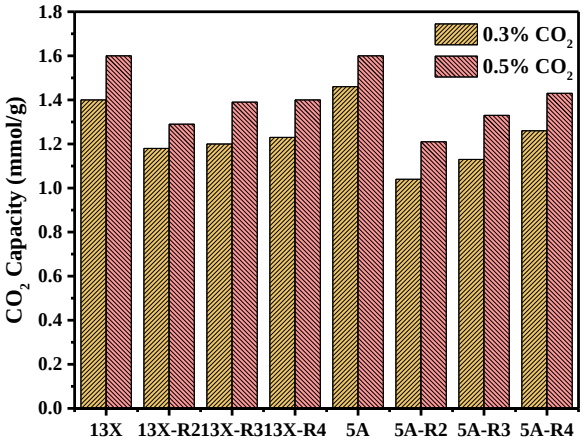

Figure 7**.** CO_2 adsorption capacities for 3D-printed monoliths and zeolite powders obtained at 25 °C using 0.3% and 0.5% CO_2 in N_2.

In addition to single point adsorption measurements, pure CO_2 and N_2 adsorption isotherms were obtained at 25 °C and 1 bar and the results are presented in Figure 8. The monoliths exhibited similar behavior to their powder counterparts displaying high affinity towards CO_2 with negligible N_2 adsorption. Consistent with TGA tests, the CO_2 isotherms for 3D-printed monoliths were comparable to those for zeolite powders. The monoliths 13X-R4 and 5A-R4 displayed a sharp CO_2 uptake at low pressures reaching 88% and 75% of their equilibrium capacities at 0.2 bar, respectively, followed by gradual increase until

full equilibrium at higher pressures. Compared to other self-standing zeolite monoliths prepared by Hassan et al.,[30] our 3D-printed monolith shows higher CO_2 uptake at room temperature.

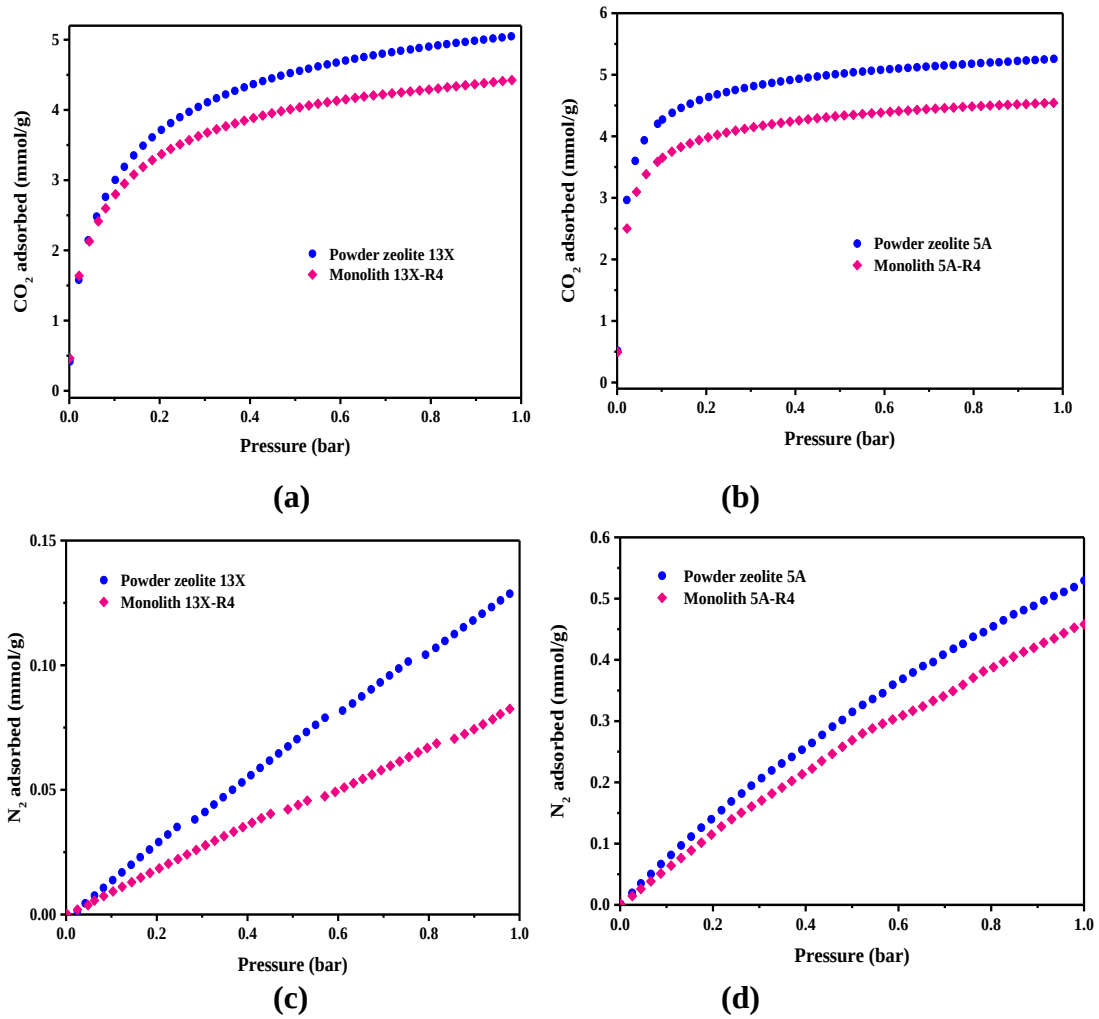

Figure 8. (a-b) CO_2 and (c-d) N_2 adsorption isotherms for 13X-R4 and 5A-R4 3D-printed monoliths and powders obtained at 25 °C.

3.5. CO_2 BREAKTHROUGH EXPERIMENTS

The dynamic adsorption performance of zeolite monoliths and powders were evaluated at 25 °C and atmospheric pressure using a feed gas containing 0.5% CO_2 in N_2 with the flow

rate of 60 mL/min and the corresponding CO_2 breakthrough profiles are presented in Figure 9. For both 13X and 5A, the zeolite powders retained CO_2 longer and exhibited longer breakthrough times than their monolithic counterparts. However, the concentration fronts of 13X-R4 and 5A-R4 monoliths were sharper than those of powders with the breakthrough width of 36 min and 61 min, respectively (compared to 40 min and 75 min, for 13X and 5A powders, respectively) indicating less mass transfer resistance in monolithic beds. Here

Table 4. Dynamic adsorption data for 3D-printed monoliths and zeolite powders.

Sample	**$t_{5\%}$** (min)	**$t_{50\%}$** (min)	**$t_{95\%}$** (min)	**Breakthrough width** (min)
Powder zeolite 13X	13	23	53	40
Monolith 13X-R4	9	19	48	36
Powder zeolite 5A	15	44	90	75
Monolith 5A-R4	9	36	70	61

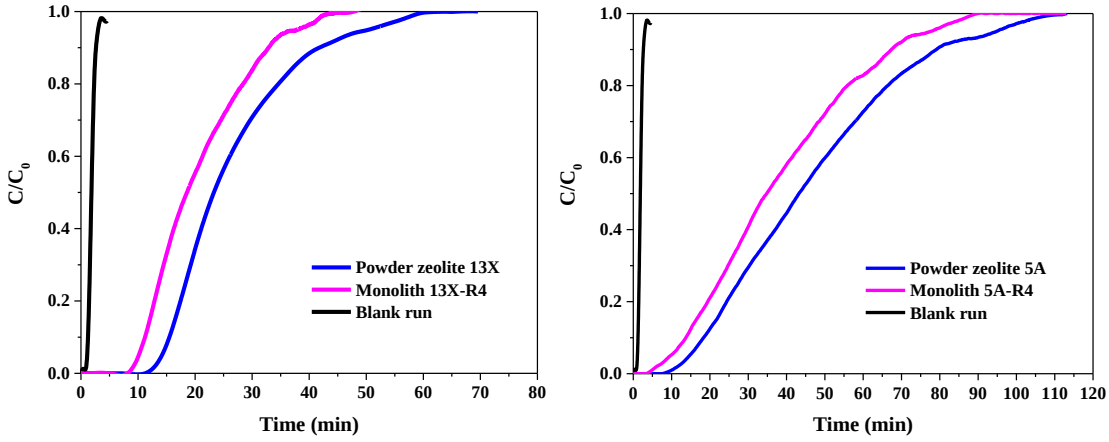

Figure 9. Breakthrough curves for (a) 13X-R4 and (b) 5A-R4 3D-printed monoliths and zeolite powders obtained at 25 °C and 1 bar.

breakthrough width is defined as the difference between the time to reach 5% and 95% of the final composition.[44] Table 4 tabulates the breakthrough times for the samples along with times to reach 50% and 95% of final concentration. Importantly, the dynamic capacities could be correlated to the zeolite loading and hence equilibrium adsorption capacity of the monoliths. The 13X powder attained 50% of the final concentration at 23 min which was 1.2 times longer than the time for 13X-R4 (23 min). This can be attributed to the difference in zeolite loading of the samples with 13X powder having 1.1 higher loading than the 13X monolith (see Table 1). The same trend could be realized for 5A samples.

4. CONCLUSIONS

In summary, the first example of 13X and 5A zeolite monoliths fabricated by 3D printing technique with high zeolite content is reported. The monolith walls consisted of a network of interconnected micro, meso, and macropores of zeolite and binder particles. The 3D-printed 5A and 13X monoliths with high zeolite loading (90 wt %) showed comparable CO_2 adsorption to their powder counterparts. More importantly, these novel structures gave rise to improved adsorption capacity and mechanical stability. By using 3D printing technique, it is possible to systematically tune the porosity, zeolite loading, and mechanical strength of monolithic structures. Our preliminary results demonstrate that the 3D printing technique offers an alternative approach for fabricating adsorbent materials in any configurations that can be used for various adsorptive-based separation processes.

ACKNOWLEDGEMENT

This work was financially supported by the NASA-EPSCoR (NNX15AK38A). The authors thank Dr. Rahaman's lab for using their 3D printer and Materials Research Center (MRC) of Missouri S&T for SEM and XRD. The authors also thank Dr. Karren More at

ORNL for helping us with the SEM images through CNMS user proposal (CNMS2015-339).

REFERENCES

I. Wang, X. *et al.* A solid molecular basket sorbent for CO_2 capture from gas streams with low CO_2 concentration under ambient conditions. *Phys. Chem. Chem. Phys.* **14,** 1485–92 (2012).

2. James, J. & Macatangay, A. Carbon dioxide–our common enemy. *Nasa/Jsc* 1–8 (2009).

3. Sherif, D. El, Knox, J. C., Marshall, N. & Flight, S. International space station carbon dioxide removal assembly (ISS CDRA) concepts and advancements. **2892,** 1–5 (2005).

4. Gall, E. T. & Nazaroff, W. W. New directions: Potential climate and productivity benefits from CO_2 capture in commercial buildings. *Atmos. Environ.* **103,** 378–380 (2015).

5. Cheng, H. H. & Tan, C. S. Removal of CO_2 from indoor air by alkanolamine in a rotating packed bed. *Sep. Purif. Technol.* **82,** 156–166 (2011).

6. Knox, J. C., Gostowski, R. & Watson, D. Development of carbon dioxide removal systems for advanced exploration systems. 1–17 (2012).

7. Huff, T., Knox, J., Marshall, N. & Flight, S. Evaluation of sorbent capacity following contamination in the ISS atmosphere. (2015).

8. Choi, S., Drese, J. H. & Jones, C. W. Adsorbent materials for carbon dioxide capture from large anthropogenic point sources. *ChemSusChem* **2,** 796–854 (2009).

9. Boot-Handford, M. E. *et al.* Carbon capture and storage update. *Energy Environ. Sci.* **7,** 130–189 (2014).

10. Occupational Safety and Health Administration, Occupational exposure to respirable crystalline silica -- Review of health effects literature and preliminary quantitative risk sssessment. *Docket OSHA-2010-0034* **1,** 1–433 (2010).

11. Mosca, A., Hedlund, J., Webley, P. A., Grahn, M. & Rezaei, F. Structured zeolite NaX coatings on ceramic cordierite monolith supports for PSA applications. *Microporous Mesoporous Mater.* **130,** 38–48 (2010).

12. Rezaei, F., Mosca, A., Webley, P., Hedlund, J. & Xiao, P. Comparison of traditional and structured adsorbents for CO_2 separation by vacuum-swing adsorption. *Adsorpt. J. Int. Adsorpt. Soc.* 4832–4841 (2010).

13. Rezaei, F. & Webley, P. Structured adsorbents in gas separation processes. *Sep. Purif. Technol.* **70,** 243–256 (2010).

14. Rezaei, F. *et al.* The effect of wall porosity and zeolite film thickness on the dynamic behavior of adsorbents in the form of coated monoliths. *Sep. Purif. Technol.* **81,** 191–199 (2011).

15. Ramos-Fernandez, E. V., Garcia-Domingos, M., Juan-Alcañiz, J., Gascon, J. & Kapteijn, F. MOFs meet monoliths: Hierarchical structuring metal organic framework catalysts. *Appl. Catal. A Gen.* **391,** 261–267 (2011).

16. Lee, T. S., Cho, J. H. & Chi, S. H. Carbon dioxide removal using carbon monolith as electric swing adsorption to improve indoor air quality. *Build. Environ.* **92,** 209–221 (2015).

17. Akhtar, F. *et al.* Aluminophosphate monoliths with high CO_2-over-N_2 selectivity and CO_2 capture capacity. *RSC Adv.* 55877–55883 (2014).

18. Lin, C. L., Lirio, S., Chen, Y. T., Lin, C. H. & Huang, H. Y. A novel hybrid metal-organic framework-polymeric monolith for solid-phase microextraction. *Chem. - A Eur. J.* **20,** 3317–3321 (2014).

19. Ahmed, A., Forster, M., Clowes, R., Myers, P. & Zhang, H. Hierarchical porous metal–organic framework monoliths. *Chem. Commun.* **50,** 14314–14316 (2014).

20. Ribeiro, R. P. P. L., Grande, C. A. & Rodrigues, A. E. Electrothermal performance of an activated carbon honeycomb monolith. *Chem. Eng. Res. Des.* **90,** 2013–2022 (2012).

21. Ko, Y. G., Lee, H. J., Kim, J. Y. & Choi, U. S. Hierarchically porous aminosilica monolith as a CO_2 adsorbent. *ACS Appl. Mater. Interfaces* **6,** 12988–12996 (2014).

22. Liu, L., Liu, Z., Huang, Z., Liu, Z. & Liu, P. Preparation of activated carbon honeycomb monolith directly from coal. *Carbon N. Y.* **44,** 1598–1601 (2006).

23. Öhrman, O., Hedlund, J. & Sterte, J. Synthesis and evaluation of ZSM-5 films on cordierite monoliths. *Appl. Catal. A Gen.* **270,** 193–199 (2004).

24. Heck, R. M., Gulati, S. & Farrauto, R. J. The application of monoliths for gas phase catalytic reactions. *Chem. Eng. J.* **82,** 149–156 (2001).

25. Sachse, A. *et al.* In situ synthesis of Cu–BTC (HKUST-1) in macro-/mesoporous silica monoliths for continuous flow catalysis. *Chem. Commun.* **48,** 4749–4751 (2012).

26. Chen, Q. *et al.* Poly (ethyleneimine)-loaded silica monolith with a hierarchical pore dtructure for H_2S adsorptive removal. *Ind. Eng. Chem. Res.* **49,** 11408–11414 (2010).

27. Rezaei, F. & Grahn, M. Thermal management of structured adsorbents in CO_2 capture processes. *Ind. Eng. Chem. Res.* **51,** 4025–4034 (2012).

28. Rezaei, F. & Webley, P. Optimum structured adsorbents for gas separation processes. *Chem. Eng. Sci.* **64,** 5182–5191 (2009).

29. Akhtar, F. & Bergström, L. Colloidal processing and thermal treatment of binderless hierarchically porous zeolite 13X monoliths for CO_2 capture. *J. Am. Ceram. Soc.* **94,** 92–98 (2011).

30. Hasan, F. A., Xiao, P., Singh, R. K. & Webley, P. A. Zeolite monoliths with hierarchical designed pore network structure: Synthesis and performance. *Chem. Eng. J.* **223,** 48–58 (2013).

31. Ojuva, A. *et al.* Mechanical performance and CO_2 uptake of ion-exchanged zeolite A structured by freeze-casting. *J. Eur. Ceram. Soc.* **35,** 2607–2618 (2014).

32. Kulkarni, A. R. & Sholl, D. S. Analysis of equilibrium-based TSA processes for direct capture of CO_2 from Air. *Ind. Eng. Chem. Res.* **51,** 8631–8645 (2012).

33. Sakwa-Novak, M. A., Yoo, C.-J., Tan, S., Rashidi, F. & Jones, C. W. Poly(ethylenimine)-Functionalized monolithic alumina honeycomb adsorbents for CO_2 capture from air. *ChemSusChem* **9,** 1–11 (2016).

34. Travitzky, N. *et al.* Additive manufacturing of ceramic-based materials. *Adv. Eng. Mater.* **16,** 729–754 (2014).

35. Tubío, C. R. *et al.* 3D printing of a heterogeneous copper-based catalyst. *J. Catal.* **334,** 110–115 (2016).

36. Rahaman, M. N. *et al.* Bioactive glass in tissue engineering. *Acta Biomater.* **7,** 2355–2373 (2011).

37. ASTM International, Single pellet crush strength of formed catalyst shapes. *D4179-01* 1–3.

38. Rownaghi, A. A. *et al.* Aminosilane-grafted zirconia–titiania–silica nanoparticles/Torlon hollow fiber composites for CO_2 capture. *ChemSusChem* **9,** 1166–1177 (2016).

39. Treacy, M. M. J. & Higgins, J. B. Collection of simulated XRD powder patterns for zeolites. *Elsevier Science*, Amsterdam, 13 (2001).

40. Brun, N. *et al.* Hard macrocellular silica Si(HIPE) foams templating micro/macroporous carbonaceous monoliths: applications as lithium ion battery negative electrodes and electrochemical capacitors. *Adv. Funct. Mater.* **19,** 3136–3145 (2009).

41. Martin, R. I. & Brown, P. W. Mechanical-properties of hydroxyapatite formed at physiological temperature. *J. Mater. Sci. Med.* **6,** 138–143 (1995).

42. Watson, D., Knox, J. C. & West, P. Sorbent structural impacts due to humidity on carbon dioxide removal sorbents for advanced exploration systems. *ICES-2015-166* (2015).

43. Knox, J. C. *et al.* Development of carbon dioxide removal systems for Ad- vanced exploration systems. *Am. Inst. Aeronaut. Astronaut.* 1–11 (2012).

44. Valdés-Solís, T., Linders, M. J. G., Kapteijn, F., Marbán, G. & Fuertes, A. B. Adsorption and breakthrough performance of carbon-coated ceramic monoliths at low concentration of n-butane. *Chem. Eng. Sci.* **59,** 2791–2800 (2004).

II. FORMULATION OF AMINOSILICA ADSORBENTS INTO 3D-PRINTED MONOLITHS AND EVALUATION OF THEIR CO_2 CAPTURE PERFORMANCE

Harshul Thakkar, Stephen Eastman, Ahmed Al-Mamoori, Amit Hajari, Ali A. Rownaghi, Fateme Rezaei*

Department of Chemical and Biochemical Engineering, Missouri University of Science and Technology, 1401 N Pine Street, Rolla, MO, 65409, United States

ABSTRACT

Amine-based materials have represented themselves as a promising class of CO_2 adsorbents; however, their large-scale implementation requires their formulation into suitable structures. In this study, we report formulation of aminosilica adsorbents into monolithic structures through 3D printing technique. In particular, 3D-printed monoliths were fabricated using pre-synthesized silica-supported tetraethylenepentamine (TEPA) and poly(ethylenimine) (PEI) adsorbents using three different approaches. In addition, a 3D-printed bare silica monolith was prepared and post-functionalized with 3-aminopropyltrimethoxysilane (APS). Characterization of the obtained monoliths indicated that aminosilica materials retained their characteristics after being extruded into 3D-printed configurations. Adsorptive performance of amine-based structured adsorbents was also investigated in CO_2 capture. Our results indicated that aminosilica materials retain their structural, physical, and chemical properties in the monoliths. In addition, the aminosilica monoliths exhibited adsorptive characteristics comparable to their corresponding powders. This work highlights the importance of adsorbent materials formulations into practical contactors such as monoliths, as the scalabale technology platform, that could facilitate rapid deployment of adsorption-based CO_2 capture processes on commercial scales.

Keywords:

3D printing technique, aminosilica adsorbents, monoliths, CO_2 capture, functionalization

1. INTRODUCTION

Despite significant advances in development of novel adsorbents and adsorption processes, adsorption-based CO_2 capture processes have yet to become commercially available on an industrial scale.[1,2] Part of the reason for that lies in the fact that most of the current body of research largely overlook development of scalable gas-solid contactors that not only exhibit high capture efficiency but also address the large-scale operational problems associated with traditional packing systems.[3] Such structured adsorbents, especially in the form of monolithic structures, have been shown to demonstrate superior mass and heat transfer characteristics than the corresponding pellets and beads while at the same time, dramatically reduce attrition and pressure drop of the adsorption column, resulting in a more cost-effective capture process.[3–9]

Various adsorbents have been investigated for CO_2 capture so far including carbon-based materials, zeolites, metal-organic frameworks (MOFs), organic-inorganic materials, and metal oxides.[4,10] Among them, amine-based adsorbents offer a great potential for large-scale implementation of capture processes mainly due to their superior advantages such as high adsorption capacity, relatively low regeneration energy requirement, long-term stability, and enhanced CO_2 uptake in the presence of water.[11] Most of the studies conducted on these materials often focus on evaluating their adsorption properties in the form of powders.

Most recently, several attempts have been undertaken to formulate this fascinating class of materials into practical configurations. For example, impregnation of pelletized mesoporous silica (MCM-41, MCM-48, and SBA-15) with PEI was demonstrated by Sharma et al.[12] The authors found that the PEI-impregnated pellets containing methyl

cellulose and activated carbon (as plasticizers) display higher CO_2 adsorption capacity than the impregnated powders and attributed this enhancement to the presence of activated carbon that is responsible for pore expansion in pelletized adsorbents. Klinthong et al.[13] used a binder solution containing 3 wt% polyallylamine (PAA) and 2 wt% NaOH to form pellets from powdered PEI-functionalized MCM-41. It was reported that the pellets prepared by this binder formula exhibit the CO_2 adsorption capacity slightly lower than the powdered adsorbent. In another study, porous silica gel beads were used as supports for several amines and a CO_2 adsorption capacity of 1.16 mmol/g at 50 °C was reported for silica gel beads modified with 15 wt% PEI.[14] Bisone et al.[15] immobalized several aminopolymers into spherical Al_2O_3 pellets and studied them for postcombustion CO_2 adsorption. More recently, pelletization of aminosilica materials was investigated by Rezaei et al.[16] through mechanical pressing of the powders. The authors demonstrated that shaping solid supported amine adsorbents into binderless pellets requires pressing the powders at low pressures (< 1000 psig) to ensure the materials retain their adsorption efficiency. In recent studies by Wilfong and co-workers[17,18] pelletization of TEPA-silica adsorbents was demonstrated through utilization of various additives and plasticizers such as fly ash, poly(vinyl chloride)(PVC), and poly(chloroprene)(PC). On the basis of mechanical strength and CO_2 adsorption performance, the authors concluded that pellets containing fly ash and PC show better adsorptive behavior and are more mechanically robust than PVC-based pellets.

The above examples focus mainly on formulation of aminosilica materials into pellets/beads while comparatively little work has been done on considering other geometries. In a recent study by Sakwa-Novak et al.[19] alumina honeycomb structures were

functionalized by PEI and studied for CO_2 capture from air. The PEI-impregnated alumina monoliths achieved a volumetric capacity of 350 mol $CO_2/m^3_{monolith}$ for 400 ppm CO_2 in N_2. Apart from this post-functionalization study, to the best of our knowledge, formulation of aminosilica materials into monolithic adsorbents has not been investigated in the past.

In our previous work, we fabricated zeolite 13X and 5A monoliths with high zeolite loadings (90 wt%) using a novel 3D printing technique.[20] In addition to high adsorption capacity and relatively fast kinetics, highly robust zeolite monoliths were obtained with tunable structural, chemical, and mechanical properties for use in gas separation processes. The 3D printing technique has recently gained immense interest in adsorption and catalysis due to its substantial benefits compared to conventional extrusion technique, including the possibility of precisely fabricating three-dimensional adsorbents/catalysts into desired configurations with controllable channel size, wall thickness, and density.[20–22]

Motivated by our previous work, the goal of this study was to employ the 3D printing method to fabricate novel aminosilica monoliths that could be used in CO_2 capture processes. We followed various formulation and paste preparation approaches to produce structures that exhibit comparable adsorptive characteristics to their powders counterparts. In the first approach, a bare silica monolith was fabricated first and then grafted by APS while in the next three approaches described in the following section, the pre-synthesized PEI- and TEPA-impregnated silica materials were used to fabricate the structures after mixing with a binder and an additive. The performance of the 3D-printed monoliths were then investigated in CO_2 capture.

2. EXPERIMENTAL SECTION

2.1. MATERIALS

Silica PD-09024 (PQ Corporation) was used to synthesize amine-functionalized powders as well as 3D-printed silica monoliths. Bentonite clay (Sigma-Aldrich) was used as a binder to achieve a desired mechanical strength required to prevent cracks on channels or external perimeter of the structure. Methyl cellulose (Thermo Fisher) was used as a plasticizer to adhere the binder and adsorbent particles. The aminopolymers (TEPA and PEI) were obtained from Sigma-Aldrich while aminosilane APS was purchased from Gelest. Ultra-high purity gases used in this study were all obtained from Airgas.

2.2. AMINOSILICA POWDERS PREPARATION

The PEI- and TEPA-impregnated and APS-grafted silica powders were synthesized according to the well-established synthesis procedures in the literature.[23,24] Briefly, using the wet impregnation process, amine-impregnated samples were synthesized by first dissolving a desired amount of amine in methanol, then adding degassed silica to the solution and letting it stir for 16-24 h at room temperature. Finally, the product was recovered by removing methanol using a rotary evaporator (rotovap), followed by drying at 105 °C overnight under vacuum. Grafting APS on silica surface was carried out by first mixing desired amounts of toluene and degassed silica, followed by adding a desired amount of APS to the mixture, stirring for 16-24 h at 85 °C, and finally vacuum filtering the solution and rinsing with toluene and ethanol before vacuum drying at 105 °C overnight.

2.3. AMINOSILICA MONOLITHS PREPARATION

2.3.1. Approach-1 (AP-1). In the first approach, bare 3D silica monoliths were printed by first mixing PD-silica, bentonite clay, and methyl cellulose with the weight ratios of 90:7:3 wt% using an IKA RW20 mixer at 250 rpm until a homogeneous powder mixture was obtained. DI water was then gradually added while mixing to form an extrudable paste. After that, the paste was loaded into a tube (10 cc, Norson EFD, USA) and the tube was tightened on the sampler holder of Aluminum Prusa I3 A Pro 3D Printer (Geeetech). The paste was extruded through 0.6 mm diameter nozzle (Tecchon) and well-defined structures with uniform channels were printed by depositing paste with external perimeter and infill density (50% of the diameter) in a layer-by-layer fashion. The fresh 3D-printed silica monoliths were then dried at 80 °C for 2-3 h to prevent development of cracks in the structure and then calcined at 550 °C to remove methyl cellulose. The 3D-printed monoliths were then functionalized with aminopolymers and aminosilane in a similar way as the silica powder, (see section 2.2).

2.3.2. Approach-2 (AP-2). In this approach, the pre-synthesized aminosilica materials were mixed with bentonite clay and methyl cellulose with the weight ratios of 90:7:3 wt% for 20 min to obtain a homogeneous powder mixture. Methanol was then added dropwise to the solid mixture until it formed a paste. This paste was then stirred for 30 min to obtain a homogeneous paste with a suitable viscosity. Then the paste was fed into the tube and extruded using the 3D printer. Finally, the obtained 3D-printed aminosilica monoliths were dried at 80 °C for 2-3 h. Calcination was not performed in this approach because of the degradation of amine moieties at high temperatures.

2.3.3. Approach-3 (AP-3). In approach-3, we adopted a procedure developed by Wilfong et al.[17] for pelletizing aminosilica adsorbents. According to this procedure, methanol and amine (PEI or TEPA, 1 wt%) were first mixed and allowed to stir for 30 min. Methyl cellulose (3 wt%) was then added gradually while heating the solution in an oil bath at 50 °C for 8 h until the methyl cellulose was dissolved. In the next step, pre-synthesized aminosilica and bentonite clay with the ratios of 90:7 wt% were mixed for 20 min and then the solution was poured into the powder mixture while stirring. To form the paste, extra methanol droplets were added to adjust the viscosity of the paste. Further steps in this procedure are the same as AP-2.

2.3.4. Approach-4 (AP-4). In approach-4, two different solutions were prepared. In the first solution, a mixture of amine (PEI or TEPA, 1 wt %), methyl cellulose (3 wt %), and methanol was formed and stirred in the oil bath at 50 °C for 8 h, whereas the second solution was obtained by mixing pre-synthesized aminosilica (90 wt %), bentonite clay (7 wt %), and methanol for 2 h at room temperature. In the next step, both solutions were combined and mixed for 45 min to form a homogenous paste. The remaining steps in this procedure are the same as AP-2.

Figure 1 visually illustrates the 3D-printed aminosilica monoliths obtained from our 3D printer. It should be pointed out here that the samples obtained from the above approaches look visually the same and are not distinguishable. APS-grafted silica monoliths were prepared only by AP-1 through post-functionalization of silica monoliths and the other approaches were not considered for this aminosilica material mainly because of the failure in paste preparation from a pre-synthesized APS-silica powder, despite several attempts in varying the paste composition or the type of solvent. On the other hand,

post-functionalization of 3D-printed silica monolith with PEI and TEPA failed to yield impregnated monoliths with high CO_2 adsorption capacity (>1 mmol/g), thus throughout this work, we only focused on characterizing and testing aminopolymer monoliths prepared by Approaches 2-4.

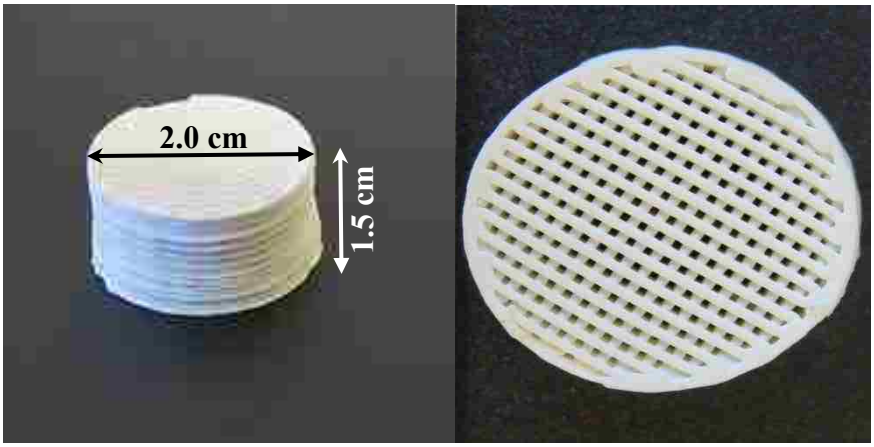

Figure 1. 3D-printed aminosilica monoliths.

2.4. CHARACTERIZATION OF AMINOSILICA MONOLITHS

To investigate the physical properties of the samples, N_2 physisorption isotherms were collected at 77 K using Micromeritics 3Flex gas analyzer. Micromeritics Prevac was utilized to outgas samples at 110 °C for 3 h prior to analyses. Surface area of all samples were evaluated by Brunauer–Emmett–Teller (BET) method whereas pore volume and pore size distribution values were derived using Hovarth-Kowazoe and Barrett-Joyner-Halenda (BJH) methods, respectively. To determine the successful incorporation of amine groups into the silica structure, FTIR spectra of the aminosilica powders and monoliths were obtained using a Nicolet-FTIR Model 750 Spectrometer. Moreover, structural morphology of the samples was studied by Hitachi S4700 Field Emission Scanning Electron

Microscopy (SEM). Elemental analysis was also conducted by a PerkinElmer elemental analyzer (Model 2400) to determine the amine loadings of the samples.

2.5. CO_2 ADSORPTION CAPACITY MEASUREMENTS

CO_2 capture capacity was measured via TGA (Q500, TA Instruments). All the amine-based powder and monolith adsorbents were degassed under N_2 with the flow rate of 40 mL/min at 110 °C prior to adsorption. Then samples were exposed to 10% CO_2 in N_2 with the flow rate of 60 mL/min at 25 °C under dry conditions. The CO_2 uptake over several samples was also measured at 50 and 75 °C. Moreover, to determine the stability of 3D-printed aminosilica monoliths, five consecutive adsorption-desorption cycles were performed on TGA with 30 min cycle time. Adsorption runs were conducted at 25 °C while desorption runs were carried out at 110 °C.

2.6. CO_2 BREAKTHROUGH EXPERIMENTS

The breakthrough experiments were performed in a fixed-bed column coupled with a BEL-Mass spectrometer (MS) using 10% CO_2/N_2 gas mixture. The schematic of the setup could be found in our previous publications.[20,25–27] Initially, N_2 was fed into the column at 60 mL/min for 2 h at 100 °C to drive off the moisture and pre-adsorbed gas molecules and then the bed was cooled down to 25 °C. For dry runs, after stabilizing the temperature, monoliths were exposed to 10% CO_2/N_2 with the flow rate of 60 mL/min until the materials reached their semi-equilibrium capacity. In addition, humid runs were carried out by first saturating the bed with water vapor for 30 min through passing a stream of humidified N_2 from a water saturator and then flowing the humidified 10% CO_2/N_2 gas mixture into the bed at 25 °C. This prehydrated mode experiment was performed to ensure the bed is saturated with water and it was then assumed that the amount of water preadsorbed in the

bed remained constant by flowing wet flue gas with RH 100% throughout the CO_2 adsorption test.[28]

3. RESULTS AND DISCUSSION

3.1. CHARACTERIZATION OF AMINOSILICA MONOLITHS

N_2 physisorption at 77 K experiments revealed typical type IV isotherms that showed H1-type hysteresis loops for aminosilica monoliths and their corresponding mesoporous powders, as presented in Figure 2a-f. The similarity between the shape of the isotherms for monoliths and related powders confirms the mesoporous nature of the aminosilica monoliths. The calcined 3D-printed silica monolith with surface area and pore volume of 312 m^2/g and 0.95 cm^3/g, respectively exhibited properties close to those of the bare silica powder (344 m^2/g and 1.04 cm^3/g, respectively), whereas for the uncalcined silica monolith both values were lower (i.e., 203 m^2/g and 0.65 cm^3/g, respectively), more likely due to the presence of methyl cellulose. The associated textural properties extracted from the isotherms are presented in Table 1. As a general trend, after amine functionalization, the N_2 uptake decreased dramatically compared to the bare silica, with the decrease being more pronounced for aminopolymer materials. Moreover, comparing the N_2 physisorption profiles of the powders and the corresponding monoliths, it follows that the uptake is lower for the monoliths which could be attributed to the presence of additives used in preparing the paste such as bentonite clay and methyl cellulose. Notably, the reduction in N_2 uptake was more pronounced in monoliths prepared by approaches 2-4, which could be justified by unclacined nature of these monoliths that still have methyl cellulose in their structure compared to the monoliths prepared by AP-1.

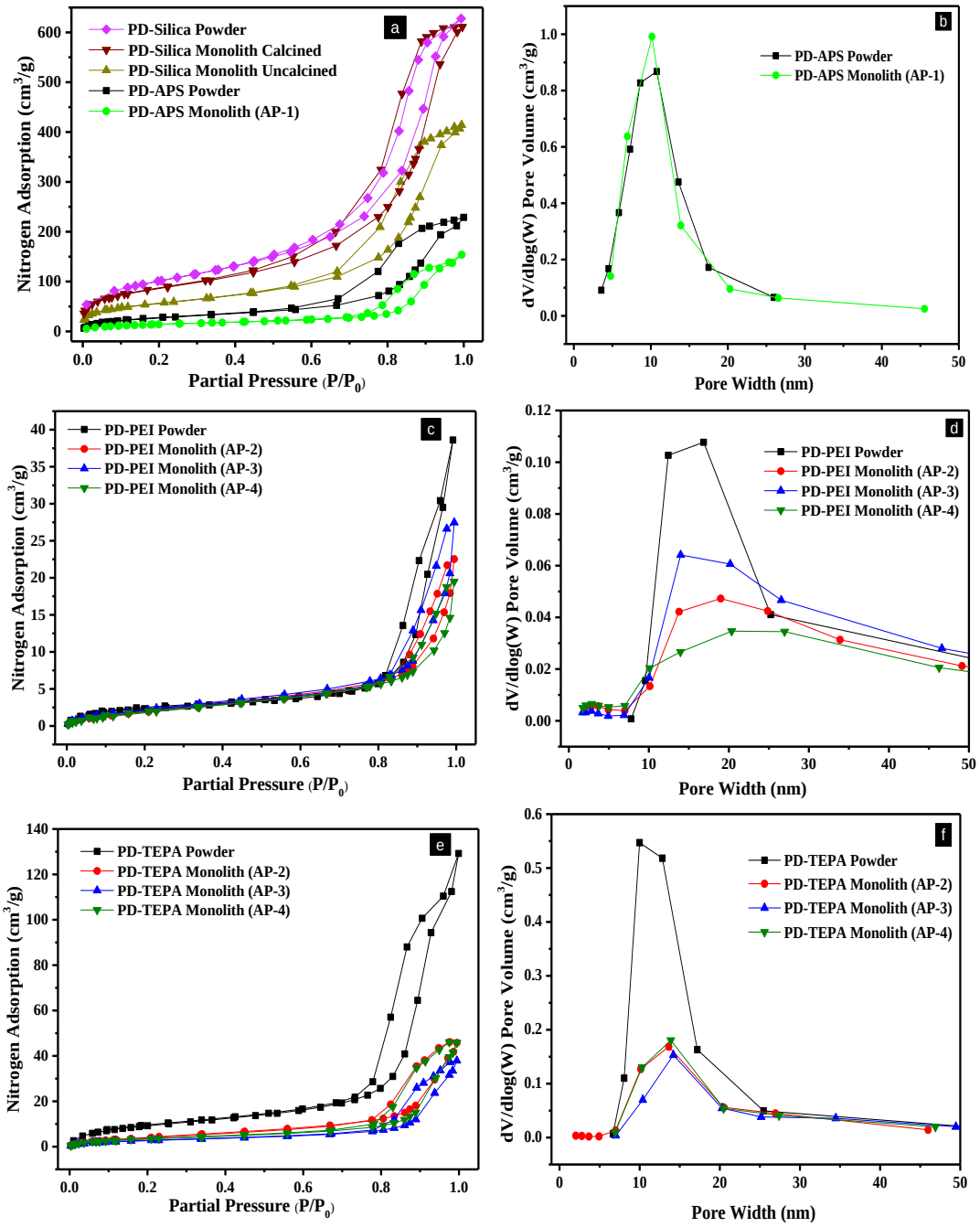

Figure 2. N_2 physisorption isotherms and pore size distribution curves for (a-b) PD-APS, (c-d) PD-PEI, and (e-f) PD-TEPA 3D-printed monoliths and their corresponding powders.

Corresponding pore size distribution (PSD) curves shown in Figure 2b, d, f reveal a uniform pore size in the structure of all 3D-printed monoliths with sizes similar to those of

powders, although the pore volumes were smaller. An average pore size ranging from 8 to 16 nm was estimated for the three types of aminosilica monoliths. Furthermore, as the data in Table 1 suggest, various approaches gave rise to nearly identical pore volumes and similar surface areas.

Table 1: Textural properties of aminosilica monoliths and corresponding powders.

Sample	**S_{BET}** (m^2/g)	**V_{total}** (cm^3/g)	**Pore width** (nm)
PD-silica Powder	344	1.04	11
PD-silica Monolith-uncalcined	203	0.65	9
PD-silica Monolith-calcined	312	0.95	10
PD-APS Powder	103	0.32	10
PD-APS Monolith (AP-1)	62	0.22	8
PD-PEI Powder	22	0.13	18
PD-PEI Monolith (AP-2)	10	0.04	14
PD-PEI Monolith (AP-3)	9	0.04	16
PD-PEI Monolith (AP-4)	8	0.03	12
PD-TEPA Powder	35	0.17	14
PD-TEPA Monolith (AP-2)	18	0.07	13
PD-TEPA Monolith (AP-3)	11	0.06	16
PD-TEPA Monolith (AP-4)	13	0.07	15

Figure 3 compares the FTIR spectra of the powder adsorbents and the monoliths prepared from various approaches. In the FTIR spectra of the samples, all the major bands that appeared in the spectra of the powders were essentially replicated for the monoliths, with the location of the peaks remaining unchanged. The strong absorption band near 1100 cm^{-1} in all spectra was attributed to Si-O-Si asymmetric stretching vibrations whereas the bands between 2800 and 3000 cm^{-1} were associated with C-H stretching vibrations. In addition, the peaks of N-H and C-N bonds appeared in the range between 1400 and 1700 cm^{-1}, respectively. The presence of an extra peak near 3700 cm^{-1} in the spectra of

monolithic samples could be attributed to OH stretching band of the bentonite clay, as can be observed in the FTIR spectra of pure bentonite clay shown in Figure 3d.

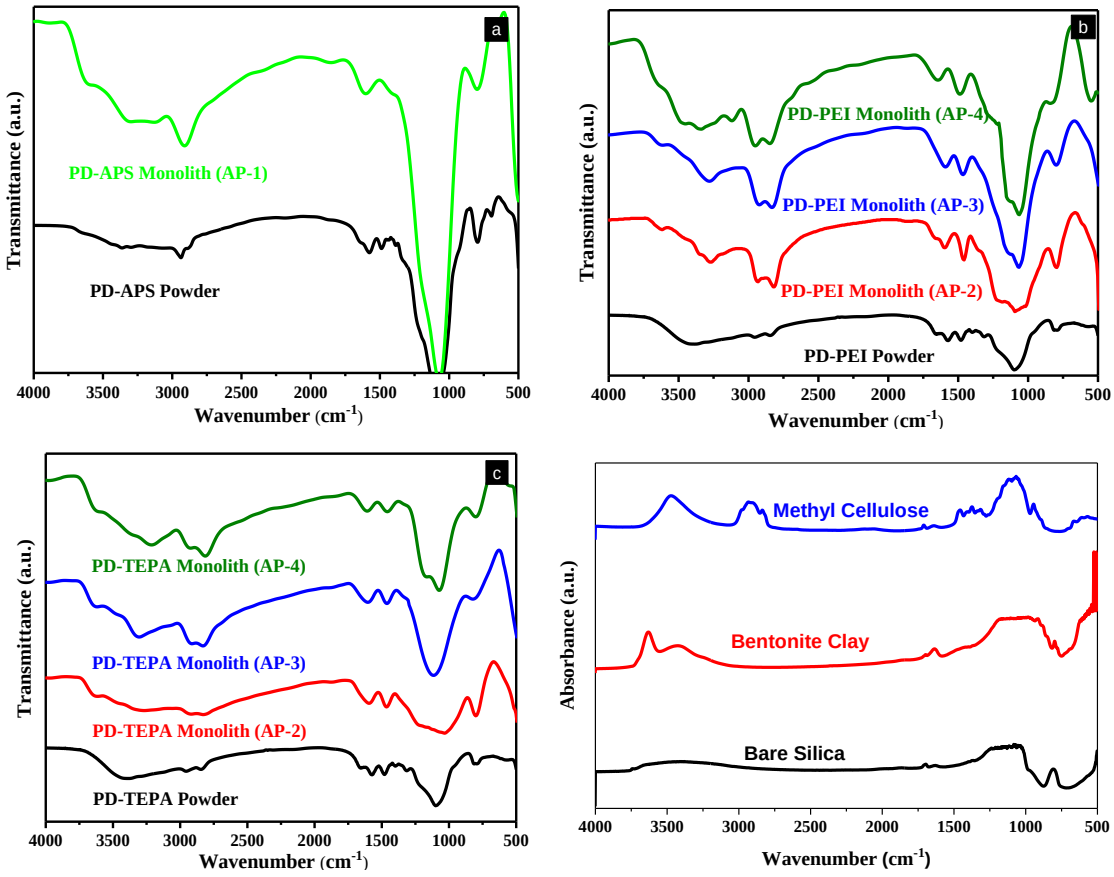

Figure 3. FTIR spectra of (a) PD-APS, (b) PD-PEI, and (c) PD-TEPA 3D-printed monoliths and their powder analogues (d) pristine powders.

SEM images illustrated in Figure 4a-d show the morphology of the 3D-printed aminosilica monoliths. Samples were mounted horizontally on the stubs and scope was operated at 5 KV accelerated voltage to achieve high resolution micrographs. High (5 µm) and low (1 mm) magnification micrographs were captured to determine the channel size and morphology of the aminosilica monoliths. As evident from Figure 4a and 4c, uniform channels with wall thickness and channel width of 0.7 and 0.90 mm for the bare silica and

0.75 and 0.85 mm for the aminosilica monoliths were obtained, respectively. A porous structure could be inferred from Figure 4b and 4c, with voids having sizes on the scale of micrometer. Figure 4b shows the agglomeration of the silica particles to form large aggregates due to particle sintering during calcination process, whereas the SEM image of uncalcined aminosilica monolith shown in Figure 4d reveals less degree of agglomeration while the monolith retained a relatively dense and porous structure.

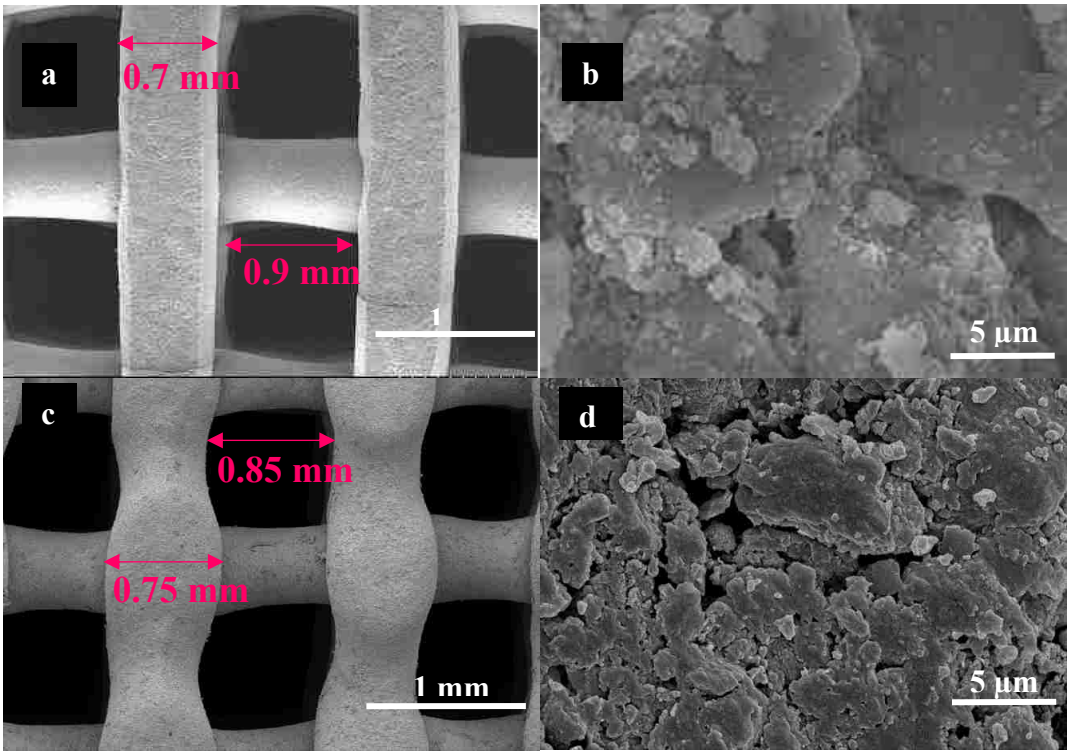

Figure 4**.** SEM images of (a,b) bare silica, and (c,d) aminosilica 3D-printed monoliths.

3.2. CO_2 ADSORPTION CAPACITY MEASUREMENTS

Equilibrium adsorption capacities of PD-silica, PD-APS, PD-PEI, and PD-TEPA 3D-printed monoliths and the corresponding powders, obtained at 25 °C are presented in Figure 5**.** Whereas the bare PD silica did not display any appreciable CO_2 capacity in both forms, the 3D-printed silica monolith grafted with APS (AP-1) showed a capacity almost the same as the PD-APS powder (1.13 mmol/g compared to 1.14 mmol/g, respectively), indicating their similar physical structure, as confirmed by textural properties shown in Table 1. On the other hand, PD-PEI and PD-TEPA monoliths showed some degree of capacity loss compared to their powder analogues. PD-PEI monolith (AP-4) exhibited 79% of the capacity of the PD-PEI powder reaching 1.22 mmol/g, whereas, the capacity of PD-TEPA monolith (AP-4) reached 2.23 mmol/g, corresponding to 87% of the capacity of its powder analogue. For both aminopolymers, the monoliths prepared by AP-4 showed the highest capacity, although the values were very close to one another for different approaches. The use of additional amine moieties (1 wt%) in AP-3 and AP-4 is responsible for higher amine loading of the monoliths prepared by these methods than those prepared by AP-2. Also, the higher uptake for AP-4 monoliths could be due to the fact that the pre-synthesized aminosilica dissolved in the methanol solution can allow the amine from another solution to impregnate the vacant pores of the silica, hence a higher amine loading and adsorption capacity compared to AP-3 in which pre-synthesized asdsorbent is not in the solution form. It should be noted here that the amount of additional amine (either PEI or TEPA) in AP-3 and AP-4 was varied from 1 to 5 wt% and an amount of 1 wt% was found to be an optimum concentration. The reduction in CO_2 uptake over impregnated monoliths compared to powders stems from the fact that the monolith is comprised of only 90 wt% and the

remaining 10 wt% of active adsorbent is binder and plasticizer which do not contribute to CO_2 capture.

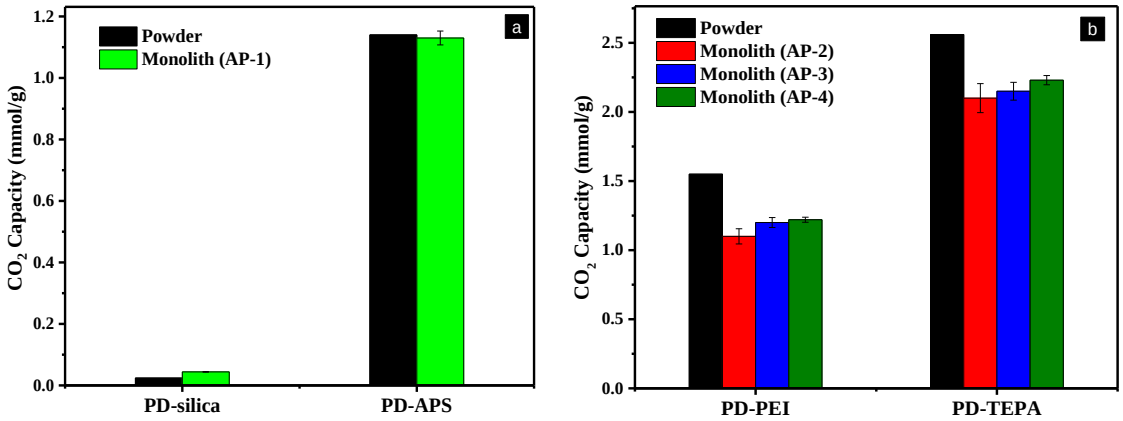

Figure 5**.** CO_2 adsorption capacities of (a) PD-silica and PD-APS, and (b) PD-PEI and PD-TEPA monoliths and corresponding powders obtained at 25 °C and 1 bar using 10% CO_2 in N_2.

Here, note that for the rest of our analysis, we have focused only on PD-APS (AP-1), PD-PEI (AP-4), and PD-TEPA (AP-4) monoliths and compared their characteristics with their powder counterparts since they exhibited the highest CO_2 capacities among all other monoliths. Table 2 lists the amine loading values obtained by elemental analysis for the adsorbents and as can be observed, the monoliths display slightly lower amine content to that of powders. This lower amine loading could be justified by considering the amine loading of 90 wt% in the 3D-printed monolithic structures prepared by AP-4. The calculated amine efficiencies (defined as the mmol of CO_2 captured per mmol of N) further confirm this observation. For APS-based adsorbents, both the amine loadings and amine efficiencies were quite similar for powder and monoliths samples. Notably, the amine efficiency of PEI-based samples was very low despite high amine content which could be

attributed to non-uniform distribution of the PEI in the pores of silica, as will be discussed later.

Table 2. Amine loading of aminosilica samples and CO_2 capacities obtained at 25 °C and 1 bar using 10% CO_2 in N_2.

Sample	**Amine content** (mmol N/g)	**CO_2 capacity** (mmol/g)	**Amine efficiency** (mmol CO_2/mmol N)
PD-APS Powder	4.95	1.14	0.23
PD-APS Monolith (AP-1)	4.83	1.13	0.24
PD-PEI Powder	14.5	1.55	0.11
PD-PEI Monolith (AP-4)	13.2	1.22	0.10
PD-TEPA Powder	12.8	2.56	0.20
PD-TEPA Monolith (AP-4)	11.5	2.23	0.19

In the literature, the competing thermodynamic (temperature dependence of CO_2 adsorption) and diffusional (CO_2 diffusion and/or aminopolymer chain mobility) effects have been reported for amine-impregnated adsorbents.[29–31] To investigate this trade-off, the adsorption capacities of the 3D-printed monoliths were measured at 25, 50 and 75 °C and as can be inferred from Figure 6, for PD-APS monolith (AP-1), the adsorption capacities decreased with increasing temperature implying no trade-off in this type of adsorbent which is expected for small monomers of APS grafted on the surface of silica support where diffusional effects play no significant roles. On the contrary, both TEPA and PEI experienced an increase in capacity upon temperature rise. PD-PEI monolith (AP-4) exhibited 34% increase in capacity when temperature raised to 50 °C and 85% increase upon further temperature increase to 75 °C, reaching 2.26 mmol/g, whereas for PD-TEPA monolith (AP-4), the capacity first exhibited a 14% rise to 2.55 mmol/g before a second increase to 3.14 mmol/g. This behavior could be attributed to the predominant diffusional

effects in amine-impregnated silica monoliths (PEI and TEPA monoliths) as a result of improved accessibility of amine sites due to enhanced chain mobility of PEI/TEPA at elevated temperatures. This further implies that the PEI/TEPA is not well dispersed in the support whereby chain mobility is highly restricted, in accordance with their low amine efficiency.

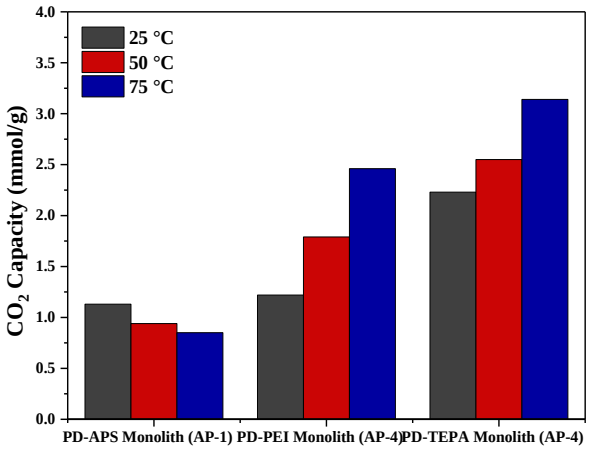

Figure 6. CO_2 adsorption capacities of 3D-printed aminosilica monoliths as a function of temperature.

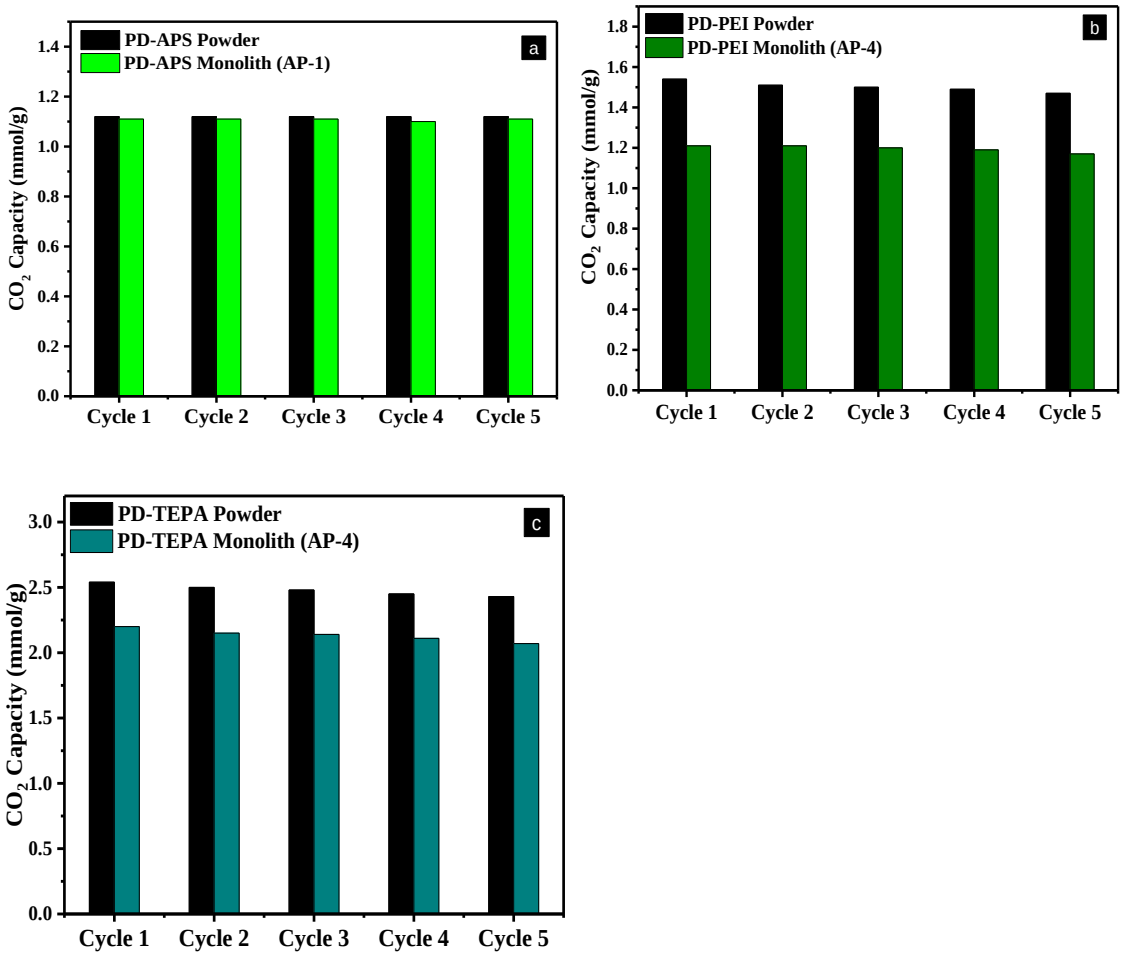

Figure 7. CO_2 cyclic capacities of (a) PD-APS, (b) PD-PEI, and (c) PD-TEPA 3D-printed monoliths and powders obtained at 25 °C.

Cyclic measurements were performed to ensure the regenerability of 3D-printed aminosilica monoliths and the results are shown in Figure 7. It can be found that PD-APS monolith retained its CO_2 capacity and no considerable capacity loss was observed after the fifth cycle while aminopolymeric materials in both powder and monolith forms experienced some degree of capacity loss. PD-PEI powder and monolith samples lost 3 and 5% of their initial capacity, respectively while for PD-TEPA powder and monolith samples, 4 and 6% capacity loss was observed, respectively. These findings are consistent

with previous studies which attributed this weight loss to both aminopolymer volatilization and oxidative degradation.[32–35]

3.3. CO_2 BREAKTHROUGH EXPERIMENTS

CO_2 breakthrough experiments were performed to investigate dynamic adsorption performance of the 3D-printed aminosilica monoliths. The corresponding concentration

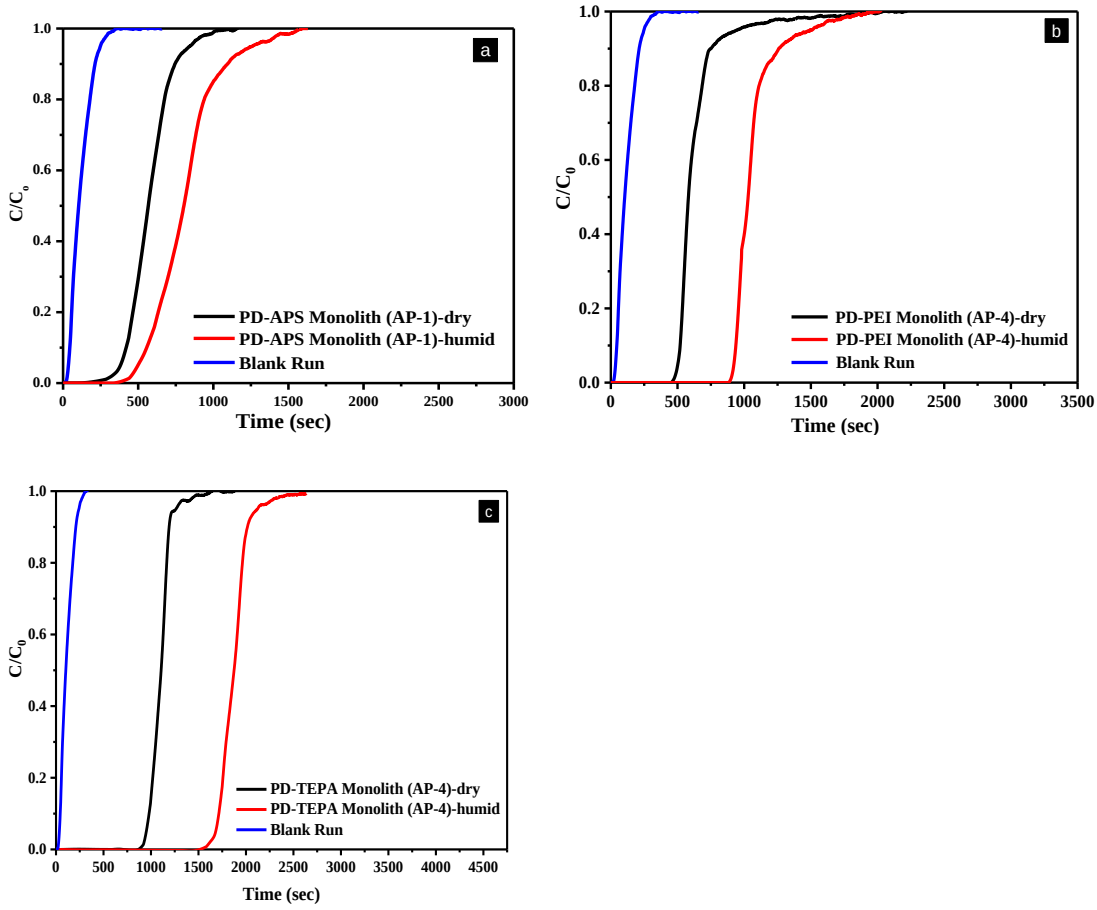

Figure 8. Breakthrough curves for (a) PD-APS, (b) PD-PEI, and (c) PD-TEPA 3D-printed monoliths obtained at 25 °C and 1 bar using dry and humid gas.

fronts for 3D aminosilica monoliths under dry and humid conditions are presented in Figure 8. As expected, due to the promotional effect of water on CO_2 adsorption of aminosilica

materials, the CO_2 breakthrough occurred at a longer time under humid condition than under dry condition implying higher uptake in the presence of water, similar to aminosilica powders.

The breakthrough width associated with each concentration front is estimated and presented in Table 3. The breakthrough width of PD-APS monolith in humid mode is 10 min which is longer than that of its dry mode analogue. Similarly, for PD-PEI and PD-TEPA monoliths, 75% and 17% increase in the breakthrough width were observed in the presence of water in comparison to dry conditions. In addition, the pseudo-equilibrium capacity, q_{pe}, defined as the capacity of the material at $t_{95\%}$ estimated from breakthrough profiles is listed in Table 3 for both dry and humid modes. Notably, the capacity of PD-APS (AP-1) increased from 1.09 to 1.61 mmol/g, whereas q_{pe} increased from 1.21 to 1.96 mmol/g for PD-PEI (AP-4) and from 2.23 to 3.12 mmol/g for PD-PEI (AP-4).

Table 3. Dynamic adsorption data for 3D-printed monoliths under dry and humid conditions.

Sample	$\mathbf{t_{5\%}}$ (min)	$\mathbf{t_{50\%}}$ (min)	$\mathbf{t_{95\%}}$ (min)	**Breakthrough width** (min)	$\boldsymbol{q_{pe}}$ (mmol/g)
PD-APS Monolith (AP-1)-dry	7	10	12	5	1.09
PD-APS Monolith (AP-1)-humid	8	13	18	10	1.61
PD-PEI Monolith (AP-4)-dry	9	10	14	4	1.21
PD-PEI Monolith (AP-4)-humid	15	18	22	7	1.96
PD-TEPA Monolith (AP-4)-dry	19	22	25	6	2.23
PD-TEPA Monolith (AP-4)-humid	28	31	35	7	3.12

4. CONCLUSION

We presented the formulation of aminosilica adsorbents into monolithic structures using the novel 3D-printing method. Various formulations were evaluated for three types

of amine-based adsorbents and their characteristics and adsorptive performance were systematically evaluated. Our results indicated that the 3D-printed aminosilica adsorbents exhibited characteristics similar to those of their powder counterparts. Additionally, their CO_2 adsorptive behavior was found to be very similar to their corresponding powders. For aminopolymers investigated here (i.e., PEI and TEPA), direct extrusion of the premade materials into monolith was found to be the best way to formulate these adsorbents, while for aminosilanes (APS), post-functionalization of bare silica monolith was a viable strategy for their formulation. More work needs to be done in order to further optimize the paste and printing conditions for this class of materials. Overall, on the basis of our findings, the 3D-printing technique appears to be a promising method for shaping amine-based adsorbents into practical contactors such as monoliths that could be easily applied to large-scale gas separation processes.

ACKNOWLEDGEMENT

The authors acknowledge the financial support from NASA-EPSCoR (NNX15AK38A).

REFERENCES

(1) Al-Mamoori, A.; Krishnamurthy, A.; Rownaghi, A. A.; Rezaei, F. Carbon Capture and Utilization Update. *Energy Technol.* **2017**, DOI: 10.1002/ente.201600747.

(2) Boot-Handford, M. E.; Abanades, J. C.; Anthony, E. J.; Blunt, M. J.; Brandani, S.; Mac Dowell, N.; Fernández, J. R.; Ferrari, M.-C. M.-C.; Gross, R.; Hallett, J. P.; Haszeldine, R. S.; Heptonstall, P.; Lyngfelt, A.; Makuch, Z.; Mangano, E.; Porter, R. T. J.; Pourkashanian, M.; Rochelle, G. T.; Shah, N.; Yao, J. G.; Fennell, P. S.; Fernandez, J. R.; Ferrari, M.-C. M.-C.; Gross, R.; Hallett, J. P.; Haszeldine, R. S.; Heptonstall, P.; Lyngfelt, A.; Makuch, Z.; Mangano, E.; Porter, R. T. J.; Pourkashanian, M.; Rochelle, G. T.; Shah, N.; Yao, J. G.; Fennell, P. S.; Fernández, J. R.; Ferrari, M.-C. M.-C.; Gross, R.; Hallett, J. P.; Haszeldine, R. S.; Heptonstall, P.; Lyngfelt, A.; Makuch, Z.; Mangano, E.; Porter, R. T. J.; Pourkashanian, M.; Rochelle, G. T.; Shah, N.; Yao, J. G.; Fennell, P. S. Carbon Capture and Storage Update. *Energy Environ. Sci.* **2014**, *7*, 130–189.

(3) Heck, R. M.; Gulati, S.; Farrauto, R. J. The Application of Monoliths for Gas Phase Catalytic Reactions. *Chem. Eng. J.* **2001**, *82*, 149–156.

(4) Hedin, N.; Andersson, L.; Bergström, L.; Yan, J. Adsorbents for the Post-Combustion Capture of CO_2 Using Rapid Temperature Swing or Vacuum Swing Adsorption. *Appl. Energy* **2013**, *104*, 418–433.

(5) Rezaei, F.; Webley, P. Structured Adsorbents in Gas Separation Processes. *Sep. Purif. Technol.* **2010**, *70*, 243–256.

(6) Hasan, F. A.; Xiao, P.; Singh, R. K.; Webley, P. A. Zeolite Monoliths with Hierarchical Designed Pore Network Structure: Synthesis and Performance. *Chem. Eng. J.* **2013**, *223*, 48–58.

(7) Küsgens, P.; Zgaverdea, A.; Fritz, H. G.; Siegle, S.; Kaskel, S. Metal-Organic Frameworks in Monolithic Structures. *J. Am. Ceram. Soc.* **2010**, *93*, 2476–2479.

(8) Akhtar, F.; Liu, Q.; Hedin, N.; Bergström, L. Strong and Binder Free Structured Zeolite Sorbents with Very High CO_2-over-N_2 Selectivities and High Capacities to Adsorb CO_2 Rapidly. *Energy Environ. Sci.* **2012**, *5*, 7664–7673.

(9) Ko, Y. G.; Lee, H. J.; Kim, J. Y.; Choi, U. S. Hierarchically Porous Aminosilica Monolith as a CO_2 Adsorbent. *ACS Appl. Mater. Interfaces* **2014**, *6*, 12988–12996.

(10) Choi, S.; Drese, J. H.; Jones, C. W. Adsorbent Materials for Carbon Dioxide Capture from Large Anthropogenic Point Sources. *ChemSusChem* **2009**, *2*, 796–854.

(11) Choi, S.; Gray, M. L.; Jones, C. W. Amine-Tethered Solid Adsorbents Coupling High Adsorption Capacity and Regenerability for CO_2 Capture from Ambient Air. *ChemSusChem* **2011**, *4*, 628–635.

(12) Sharma, P.; Seong, J. K.; Jung, Y. H.; Choi, S. H.; Park, S. Do; Yoon, Y. I. I.; Baek, I. H. Amine Modified and Pelletized Mesoporous Materials: Synthesis, Textural-Mechanical Characterization and Application in Adsorptive Separation of Carbondioxide. *Powder Technol.* **2012**, *219*, 86–98.

(13) Klinthong, W.; Huang, C. H.; Tan, C. S. Polyallylamine and NaOH as a Novel Binder to Pelletize Amine-Functionalized Mesoporous Silicas for CO_2 Capture. *Microporous Mesoporous Mater.* **2014**, *197*, 278–287.

(14) Minju, N.; Abhilash, P.; Nair, B. N.; Mohamed, A. P.; Ananthakumar, S. Amine Impregnated Porous Silica Gel Sorbents Synthesized from Water – Glass Precursors for CO_2 Capturing. *Chem. Eng. J.* **2015**, *269*, 335–342.

(15) Bisone, L.; Bittanti, S.; Canevese, S. M.; De Marco, A.; Garatti, S.; Notaro, M.; Prandoni, V. A Postcombustion Carbon Capture Process by Amines Supported on Solid Pellets with Estimation of Kinetic Parameters. *Ind. Eng. Chem. Res.* **2015**, *54*, 2743–2762.

(16) Rezaei, F.; Sakwa-Novak, M. A.; Bali, S.; Duncanson, D. M.; Jones, C. W. Shaping Amine-Based Solid CO_2 Adsorbents: Effects of Pelletization Pressure on the Physical and Chemical Properties. *Microporous Mesoporous Mater.* **2015**, *204*, 34–42.

(17) Wilfong, W. C. C.; Gray, M. L. L.; Kail, B. W. W.; Howard, B. H. H. Pelletization of Immobilized Amine Carbon Dioxide Sorbents with Fly Ash and Poly(vinyl Chloride). *Energy Technol.* **2016**, *4*, 610–619.

(18) Wilfong, W. C.; Kail, B. W.; Howard, B. H.; Fernandes de Aquino, T.; Teixeira Estevam, S.; Gray, M. L. Robust Immobilized Amine CO_2 Sorbent Pellets Utilizing a Poly(Chloroprene) Polymer Binder and Fly Ash Additive. *Energy Technol.* **2016**, *4*, 1–6.

(19) Sakwa-Novak, M. A.; Yoo, C.-J.; Tan, S.; Rashidi, F.; Jones, C. W. Poly(ethylenimine)-Functionalized Monolithic Alumina Honeycomb Adsorbents for CO_2 Capture from Air. *ChemSusChem* **2016**, *9*, 1859–1868.

(20) Thakkar, H. V.; Eastman, S.; Hajari, A.; Rownaghi, A. A.; Knox, J. C.; Rezaei, F. 3D-Printed Zeolite Monoliths for CO_2 Removal from Enclosed Environments. *ACS Appl. Mater. Interfaces* **2016**, *8*, 27753−27761.

(21) Tubío, C. R.; Azuaje, J.; Escalante, L.; Coelho, A.; Guitián, F.; Sotelo, E.; Gil, A. 3D Printing of a Heterogeneous Copper-Based Catalyst. *J. Catal.* **2016**, *334*, 110–115.

(22) Couck, S.; Lefevere, J.; Mullens, S.; Protasova, L.; Meynen, V.; Desmet, G.; Baron, G. V.; Denayer, J. F. M. CO_2, CH_4 and N_2 Separation with a 3DFD-Printed ZSM-5 Monolith. *Chem. Eng. J.* **2017**, *308*, 719–726.

(23) Didas, S. A.; Kulkarni, A. R.; Sholl, D. S.; Jones, C. W. Role of Amine Structure on Carbon Dioxide Adsorption from Ultradilute Gas Streams such as Ambient Air. *ChemSusChem* **2012**, *5*, 2058–2064.

(24) Rezaei, F.; Jones, C. W. Stability of Supported Amine Adsorbents to SO_2 and NO_x in Post-Combustion CO_2 Capture - 1. Single Component Adsorption. *Ind. Eng. Chem. Res.* **2013**, *52*, 12192–12201.

(25) Rownaghi, A. A.; Kant, A.; Li, X.; Thakkar, H.; Hajari, A.; He, Y.; Brennan, P. J.; Hosseini, H.; Koros, W. J.; Rezaei, F. Aminosilane-Grafted Zirconia–Titiania–Silica Nanoparticles/Torlon Hollow Fiber Composites for CO_2 Capture. *ChemSusChem* **2016**, *9*, 1166–1177.

(26) Brennan, P. J.; Thakkar, H.; Li, X.; Rownaghi, A. A.; Koros, W. J.; Rezaei, F. Effect of Post-Functionalization Conditions on the Carbon Dioxide Adsorption Properties of Aminosilane-Grafted Zirconia/Titania/Silica-Poly(amide-Imide) Composite Hollow Fiber Sorbents. *Energy Technol.* **2016**, *4*, 1–12.

(27) Rownaghi, A. A.; Rezaei, F.; Labreche, Y.; Brennan, P. J.; Johnson, J. R.; Li, S.; Koros, W. J. In Situ Formation of a Monodispersed Spherical Mesoporous Nanosilica – Torlon Hollow-Fiber Composite for Carbon Dioxide Capture. *ChemSusChem* **2015**, *8*, 3439–3450.

(28) Fan, Y.; Lively, R. P.; Labreche, Y.; Rezaei, F.; Koros, W. J.; Jones, C. W. Evaluation of CO_2 Adsorption Dynamics of Polymer/silica Supported Poly (Ethylenimine) Hollow Fiber Sorbents in Rapid Temperature Swing Adsorption. *Int. J. Greenh. Gas Control* **2014**, *21*, 61–71.

(29) Sayari, A. Amine-Containing Nanoporous Materials for CO_2 Removal. In *Technical Proceedings of the 2013 NSTI Nanotechnology Conference and Expo, NSTI-Nanotech 2013*; 2013; Vol. 3, pp 698–700.

(30) Belmabkhout, Y.; Serna-guerrero, R.; Sayari, A. Adsorption of CO_2-Containing Gas Mixtures over Amine-Bearing Pore-ExpandedMCM-41 Silica : Application for Gas Purification. *Ind. Eng. Chem. Res.* **2010**, *49*, 359–365.

(31) Chaikittisilp, W.; Khunsupat, R.; Chen, T. T.; Jones, C. W. Poly (Allylamine)-Mesoporous Silica Composite Materials for CO_2 Capture from Simulated Flue Gas or Ambient Air. *Ind. Eng. Chem. Res.* **2011**, *50*, 14203–14210.

(32) Sayari, A.; Heydari-Gorji, A.; Yang, Y. CO_2-Induced Degradation of Amine-Containing Adsorbents: Reaction Products and Pathways. *J. Am. Chem. Soc.* **2012**, *134*, 13834–13842.

(33) Heydari-gorji, A.; Sayari, A. Thermal, Oxidative, and CO_2-Induced Degradation of Supported Polyethylenimine Adsorbents. *Ind. Eng. Chem. Res.* **2012**, *51*, 6887–6894.

(34) Didas, S. S. A.; Zhu, R.; Brunelli, N. A. N.; Sholl, D. S.; Jones, C. W. Thermal, Oxidative and CO_2 Induced Degradation of Primary Amines Used for CO_2 Capture: Effect of Alkyl Linker on Stability. *J. Phys. Chem. C* **2014**, *118*, 12302–12311.

(35) Rezaei, F.; Lively, R. P. R.; Labreche, Y.; Chen, G.; Fan, Y.; Koros, W. J.; Jones, C. W. Aminosilane-Grafted Polymer/Silica Hollow Fiber Adsorbents for CO_2 Capture from Flue Gas. *ACS Appl. Mater. Interfaces* **2013**, *5*, 3921–3931.

III. 3D-PRINTED METAL-ORGANIC FRAMEWORK MONOLITHS FOR GAS ADSORPTION PROCESSES

Harshul Thakkar, Stephen Eastman, Qasim Al-Naddaf, Ali A. Rownaghi, Fateme Rezaei*

Department of Chemical and Biochemical Engineering, Missouri University of Science and Technology, Rolla, Missouri 65409-1230, United States

ABSTRACT

Metal-Organic Frameworks (MOFs) have shown promising performance in separation, adsorption, reaction and storage of various industrial gases, however, their large-scale applications have been hampered by the lack of a proper strategy to formulate them into scalable gas-solid contactors. Herein, we report fabrication of MOF monoliths using 3D printing technique and evaluation of their adsorptive performance in CO_2 removal from air. The 3D-printed MOF-74(Ni) and UTSA-16(Co) monoliths with MOF loadings as high as 80 and 85 wt %, respectively were developed and their physical and structural properties were characterized and compared with those of MOF powders. Our adsorption experiments showed that upon exposure to 5,000 ppm (0.5%) CO_2 at 25 ºC, the MOF-74(Ni) and UTSA-16(Co) monoliths can adsorb CO_2 with the uptake capacity of 1.35 and 1.31 mmol/g, respectively, which are 79 and 87% of the capacity of their MOF analogues under the same conditions. Furthermore, a stable performance was obtained for self-standing 3D-printed monolithic structures with relatively good adsorption kinetics. The preliminary findings reported in this investigation highlight the advantage of robocasting (3D printing) technique for shaping MOF materials into practical configurations that are suitable for various gas separation applications.

Keywords:

3D printing, self-standing monolith, MOF-74(Ni), UTSA-16(Co), CO_2 capture

1. INTRODUCTION

Formulation of solid materials into practical contactors that could be easily applied to large-scale processes offers numerous advantages in various fields relevant to separation, adsorption, reaction, and storage of a wide variety of gaseous streams. Traditionally, the adsorbents and catalysts have been shaped into beads or pellets for their large-scale implementation, however, the occurrence of frequent problems such as high pressure drop, poor mass and transfer requirements and loss of material due to attrition and dusting has led the researchers to consider devising other configurations that could address these issues.[1,2] In that regard, monolithic structures have gained a great deal of attention because the uniform flow pattern through their channels facilitates a lower pressure drop specially at higher gas throughputs while offering better mass and heat transfer characteristics due to their thin walls. These structures have long been used as three-way catalytic convertors for SO_x/NO_x removal from automotive exhaust and the removal of VOCs from various gas streams.[1]

The conventional extrusion technique is commonly used to manufacture monolithic structures, however, this method is costly and offers less flexibility in the design of structures with tailored geometry. Additive manufacturing (3D printing or robocasting) on the other hand, has been shown to offer a cost-effective solution to the limitations of the extrusion. Robust monoliths with desired wall thickness, channel size and density can be precisely obtained using 3D printing. This technique has been recently used by various researchers to develop structured adsorbents, catalysts and membranes.[3–5] Tubio et al.[6] developed heterogeneous Cu/Al_2O_3 catalysts using 3D printing technique and reported high catalytic efficiency and good recyclability for their printed monoliths. In our previous

works,[7,8] we applied the 3D printing technique to manufacture zeolites (13X and 5A) and aminosilica (PEI-, TEPA- and APS-silica) monoliths with high adsorbent loading (ca. 90 wt %) and applied them to CO_2 removal from air and flue gas. Our 3D-printed monoliths displayed comparable adsorption performance to their powders analogues. Most recently, Denayer and co-workers reported fabrication of ZSM-5[9] and SAPO-34[10] monoliths for separation of CO_2, CH_4 and N_2 and demonstrated excellent separation performance for their printed zeolite monoliths.

Metal-Organic Frameworks (MOFs) with tunable physical, structural and chemical properties have shown outstanding performance as adsorbents, membranes, and catalysts.[11–13] To enable their industrial gas separation use, they should be properly shaped into suitable contactors. Formulation of several MOFs such as MOF-5, UTSA-16 and MOF-74 into pellets or granules has been demonstrated by various research groups.[14–16] In addition, incorporation of MOFs into hollow fibers through conversion of hydroxyl double salt directly into the MOF without the use of any aqueous solution has been also attempted recently.[17] Growing MOF crystals on the walls of monolithic supports has been shown as a facile approach to shape this commonly studied class of adsorbents.[18–24] In our recent works,[21,22] we grew MOF-74(Ni) and UTSA-16(Co) films onto the wall of cordierite monoliths using various techniques and although a fairly high MOF loading (73 and 80 wt %, respectively) was obtained, the MOF-coated monoliths failed to exhibit a comparable CO_2 capture capacity to the MOF powders.

In general, such coating approach does not provide high adsorbent loading per unit volume of the bed and hence it is difficult to match the performance of coated monoliths with that of their powders counterparts. To address this issue, self-standing monoliths that

consist of a large weight fraction of MOF powder (> 80 wt%) mixed with a suitable binder and other additives have been developed.[25,26] For example, Kusgens et al.[25] fabricated HKUST ($Cu_3(BTC)_2$) monoliths with 80 wt % MOF loading using a two-step extrusion method. In another study, manufacturing of highly porous MIL-101(Cr) monoliths with high loading of 75 wt % was prepared by Hong et al.[26] and the authors reported enhanced CO_2 adsorption capacity at higher pressure and reduced temperature for their self-standing MOF monolith. Another approach was reported by Moitra et al.[27] by which macro-meso-microporous HKUST-1 monoliths were obtained by direct conversion of $Cu(OH)_2$-based monoliths while preserving the characteristic macroporous structure for application in continuous flow reactors. To the best of our knowledge, there are no reports on the fabrication of 3D-printed MOF monoliths.

Inspired by our earlier works on development of 3D-printed monolithic adsorbents and the advantages offered by 3D printing technology in general, we fabricated two types of 3D-printed MOF monoliths from MOF-74(Ni) and UTSA-16(Co), in this work. The obtained structures were physically and structurally characterized and compared with the MOF powders. In addition, we demonstrated their use in gas adsorption processes, in particular, in the removal of CO_2 from enclosed environments by performing equilibrium and dynamic adsorption experiments.

2. EXPERIMENTAL SECTION

2.1. MOF POWDERS AND 3D-PRINTED MOF MONOLITHS PREPARATION

Both MOF-74(Ni) and UTSA-16(Co) powders were synthesized, activated and evacuated according to the well-established procedures in the literature.[28–30] The 3D-printed MOF monoliths were fabricated according to a two-solution based procedure

depicted in Figure 1. Briefly, the first solution was prepared by dissolving MOF powders and bentonite clay (as a binder) in ethanol. The mixture was then allowed to stir for 2 h to obtain a homogeneous solution. The second solution was obtained by dissolving Poly(vinyl) alcohol (PVA)(as a plasticizer) in DI water and ethanol and mixing for 0.5 h at room temperature followed by sonication for 30 min. In the next step, both solutions were combined and mixed using an IKA RW20 mixer at 250 rpm for 2-3 h until an extrudable paste was obtained. The paste was then loaded into a syringe (3 cc, Norson EFD, USA) and extruded from a 0.85 mm diameter nozzle (Tecchon) by pressurizing (2-5 psig) air into the syringe. Well-defined monolithic configurations (designed by AutoCAD software) with uniform channels were printed in a layer-by-layer manner. The 3D-printed MOF structures with 1.5 cm height and 1.5 cm diameter were obtained and transferred to a conventional oven for heating at 100 ºC to prevent the development of cracks.

The weight ratios of the materials used in the solutions are reported in Table 1. It is important to note that the compositional ratios of binder and plasticizer to the MOF were varied and optimized to achieve a viscous and extrudable paste. Maximum MOF contents we used were 80 and 85 wt % for MOF-74(Ni) and UTSA-16(Co), respectively, since weight ratios larger than these amounts failed to yield either an extrudable paste or monoliths with good mechanical strength.

Table 1. Compositional ratio of 3D-printed MOF monoliths.

Monolith	**MOF** (wt %)	**Bentonite Clay** (wt %)	**PVA** (wt %)	**DI Water : Ethanol** (vol %)
MOF-74(Ni)	80	15	5	5 : 95
UTSA-16(Co)	85	10	5	2 : 98

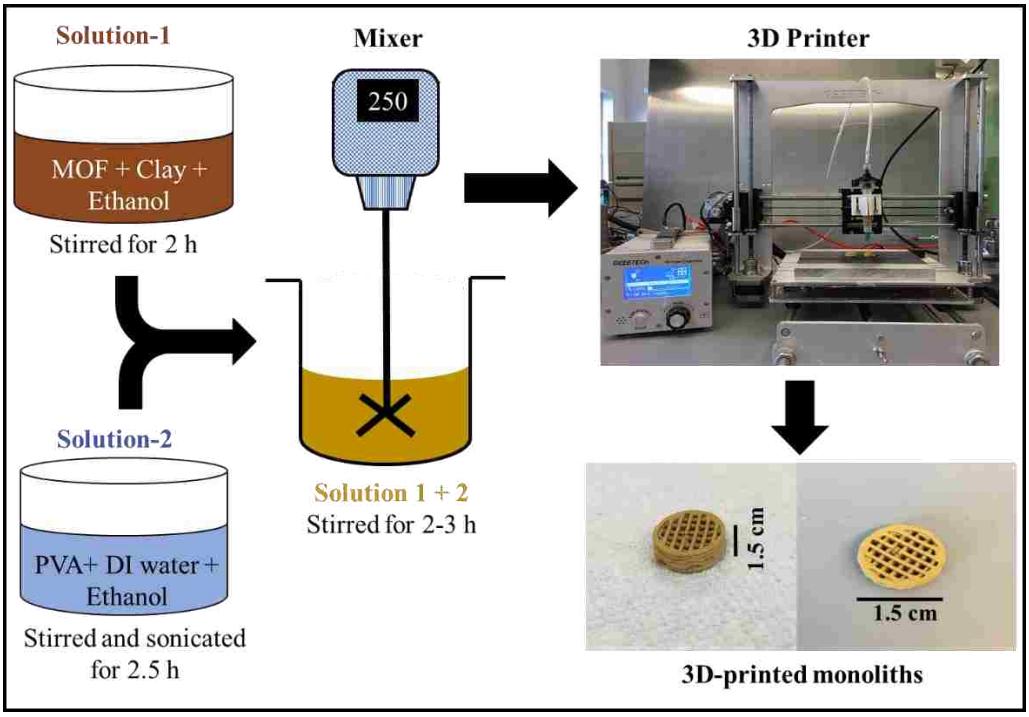

Figure 1. Schematic of 3D-printed MOF monoliths preparation procedure.

2.2. 3D-PRINTED MOF MONOLITHS CHARACTERIZATION

To probe the crystal structure of MOFs in the printed monoliths, X-ray diffraction (XRD) measurements were conducted using PANalytical X'Pert Multipurpose X-ray Diffractometer with a scan step size of 0.02°/step at the rate of 147.4 s/step. To investigate the textural properties of the samples, N_2 physisorption measurements were performed at 77 K on a Micromeritics 3Flex instrument. MOF-74(Ni) and UTSA-16(Co) samples in both powder and monolith forms were first outgassed on a Micromeritics PreVac at 250 °C and 110 °C for 6 h, respectively before the measurements. The total pore volume and pore size distribution (PSD) were estimated by Barrett-Joyner-Halenda (BJH) desorption method at a relative pressure of 0.99 while the surface area was calculated using the Brunauer−Emmet-Teller (BET) method. Field-emission scanning electron microscopy

(SEM) (Hitachi, Model S4700) was utilized to examine the structural morphology of the obtained monoliths. To quantify the amount of PVA and binder residual in the monoliths, thermogravimetric analysis (TGA) was carried out from 25 °C to 900 °C, at a rate of 20 °C/min under N_2 using TGA (Model Q500, TA Instruments).

2.3. MECHANICAL TESTING

An Instron 3369 mechanical testing instrument (Instron, Norwood, USA) was used to assess the mechanical integrity of the 3D-printed MOF monoliths. To prevent the development of cracks on the surface, the monoliths were polished with a 3M surface smoothing sand paper prior to tests. After polishing, they were placed between to metal plates and compressed with 500 N load cell at 2.5 mm/min while recording the applied load and piston movement. The compressive force was applied in axial direction until the monoliths broke.

2.4. CO_2 ADSORPTION EXPERIMENTS

To measure the CO_2 adsorption capacity of the MOF materials, TGA (Model Q500, TA Instruments) was utilized. First, MOF-74(Ni) and UTSA-16(Co) samples were outgassed at a rate of 10 °C/min to 250 °C and 110 °C, respectively under N_2 with flow rate of 40 mL/min to drive off pre-adsorbed moisture or any other impurities. To measure the CO_2 uptake, samples were cooled down to 25 °C and exposed to 5,000 ppm (0.5%) CO_2 in N_2 with flow rate of 60 mL/min. To determine the stability of the 3D printed MOF monoliths, cyclic runs with five consecutive adsorption-desorption cycles were performed on TGA with cycle time of 60 min under the same conditions. The CO_2 adsorption isotherms were also measured at 25, 50 and 75 °C on the 3Flex. Prior to adsorption

isotherms analysis, all samples were degassed at corresponding temperatures on PreVac (Micromeritics).

The breakthrough experiments were also conducted to determine the dynamic adsorption performance of 3D-printed MOF monoliths and their corresponding powders. The runs were carried out in a fixed bed column connected to a mass spectrometer (BELMass). The schematic of the experiment can be found in our previous publication.[31] Prior to breakthrough analysis, the column was loaded with 0.65 g of 3D-printed monoliths and powders counterparts and heated to their aforementioned temperatures under N_2 to remove moisture or any other adsorbed gases. After cooling down to 25 °C, the samples were exposed to 0.5% CO_2/N_2 with the flow rate of 40 mL/min and concentration data were recorded by the mass spectrometer.

3. RESULTS AND DISCUSSION

3.1. PHYSICAL AND STRUCTURAL PROPERTIES OF 3D-PRINTED MOF MONOLITHS

The XRD patterns of the MOF powders and monoliths are presented in Figure 2a-b. For the 3D-printed MOF-74(Ni) monolith, the X-ray reflections from planes (110) and (300) with diffraction peaks at $2\theta = 7^{\circ}$ and 12° confirm the MOF-74(Ni) crystal structure (Figure 2a). Similarly, as can be seen from Figure 2b, prominent diffraction peaks associated with the MOF structure were obtained in the spectrum of 3D-printed UTSA-16(Co) monolith when compared to the powder spectrum. As evident from these XRD patterns, high degree of crystallinity was retained for both MOF-74(Ni) and UTSA-16(Co) MOFs after extruding them into the monolith form although slight differences in the peak intensity were observed which could be attributed to the presence of binder and plasticizer in the monolith structure. Moreover, the diffraction peaks of bentonite clay ($2\theta = 20^{\circ}, 27^{\circ}$)

and PVA (19.5º, 22º) with low intensity were overlapped with the peaks of the MOFs and thus not visible in these spectra. The XRD patterns of both bentonite clay and PVA are presented in Figure 2c, d.

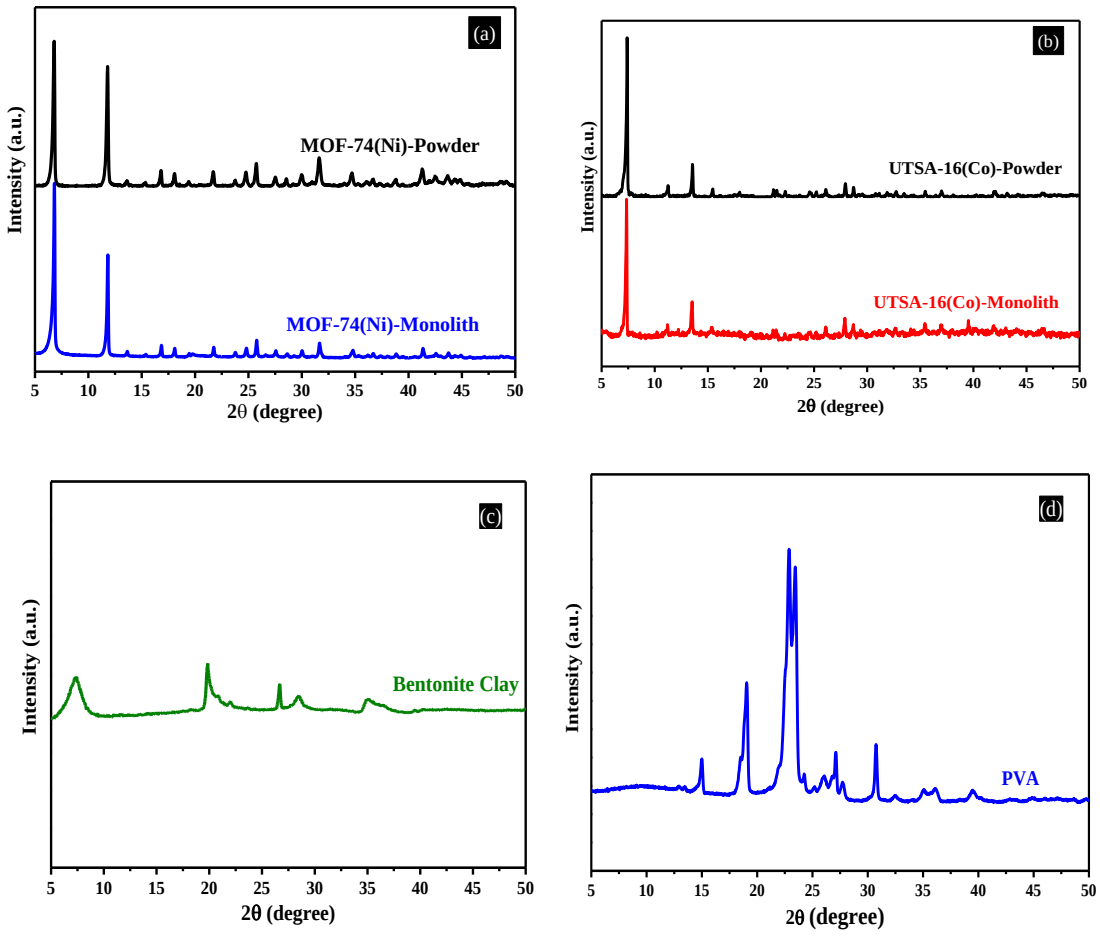

Figure 2: XRD patterns for 3D-printed monoliths with their powder counterparts (a) MOF-74(Ni), (b) UTSA-16(Co), bare powders (c) bentonite clay, and (d) PVA.

The N_2 physisorption isotherms and PSD curves of both monoliths and corresponding powders are shown in Figure 3a-d. As Figure 3a illustrates, MOF-74(Ni) in both powder and monolith form displayed type I isotherm indicative of microporous nature of the

material with smaller N_2 uptake for the monolith than the powder. In addition, comparison of the PSD profiles shown in Figure 3b confirms the uniform pore structure of the 3D-printed MOF-74(Ni) monolith, similar to the MOF powder with the pores having sizes in the range of 1-4 nm, but with smaller pore volume. For 3D-printed UTSA-16(Co) monolith, a hysteresis loop was appeared in the N_2 isotherms shown in Figure 3c, as opposed to the MOF powder, implying that some mesopores were formed in the MOF structure during printing. This could be attributed to the effect of water added while preparing the paste. According to previously reported results,[16,32] reaction of hydroxyl groups of water with citrate units of UTSA-16(Co) that consisted of –COOH groups opens the straight channels along the x-axis, hence resulting in the formation of larger pores. This however, was not the case for MOF-74 (Ni) monolith. The PSD profile of the UTSA-16(Co) monolith in Figure 3d reveals the mesoporous nature of this 3D-printed monolith with the mesopores having sizes on the order of ~20-25 nm.

Table 2 summarizes the corresponding surface area, pore volume and pore sizes of all MOF samples. The reduced surface area of 3D-printed monoliths up to 38% (from 1180 to 737 m^2/g) for MOF-74(Ni) and 30% (from 631 to 444 m^2/g) and UTSA-16(Co), can be attributed to the presence of additives (bentonite clay and PVA) used to shape the printed monoliths. The loss of porosity could also be due to the contact with water while preparing the paste. The decreased surface area of MOF-74(Ni) and UTSA-16(Co) monoliths found to be proportional to MOF loading (see Table 1).

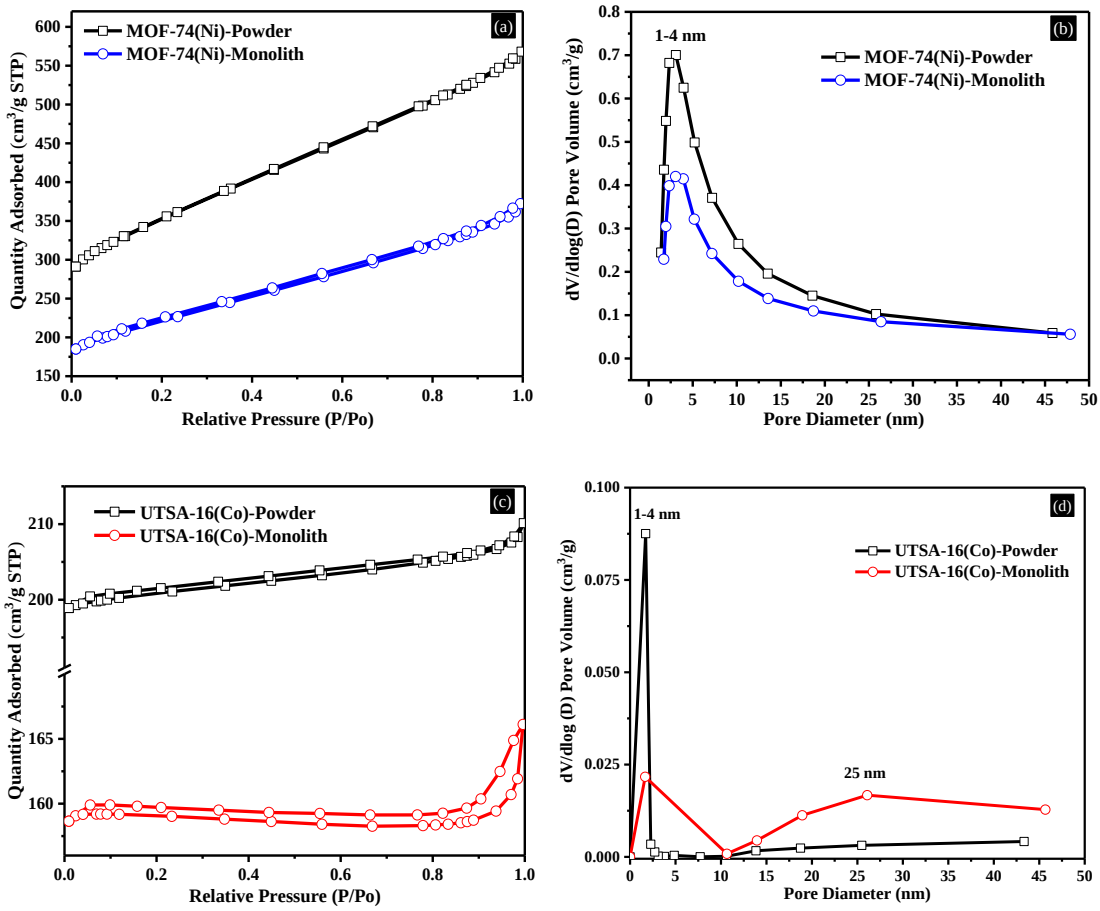

Figure 3. Nitrogen physisorption isotherms and pore size distribution curves for 3D printed MOF monoliths (a, b) MOF-74(Ni), and (c, d) UTSA-16(Co) and their corresponding powders.

The uniform pore sizes of 1.17 and 1.18 nm for MOF-74(Ni) and UTSA-16(Co), respectively were found for both forms. In addition, the pore volume of MOF-74(Ni) and UTSA-16(Co) monoliths were calculated to be 0.31 and 0.19 cm^3/g, respectively, which were found to be lower than that of their corresponding powders as a result of lower MOF content. We previously observed a similar trend for 3D-printed zeolite and aminosilica monoliths.[7,8] For 3D-printed UTSA-16(Co), the mesopore volume was calculated to be 0.06 cm^3/g monolith.

Table 2. Textural properties of 3D-printed MOF monoliths and their powder counterparts.

Sample	**S_{BET}[a]** (m^2/g)	**V_{micro}[b]** (cm^3/g)	**V_{meso}[c]** (cm^3/g)	**d_{microo}[d]** (nm)	**d_{meso}[d]** (nm)
MOF-74(Ni)-Powder	1180	0.51	-	1.17	-
MOF-74(Ni)-Monolith	737	0.32	-	1.17	-
UTSA-16(Co)-Powder	727	0.29	-	1.18	-
UTSA-16(Co)-Monolith	568	0.23	0.06	1.18	25

[a] Obtained at P/P_0 in the range of 0.05-0.3. [b] Estimated by t-plot. [c] Estimated by subtracting V_{micro} from the total volume at $P/P_0 = 0.99$. [d] Estimated using Horvath–Kawazoe method.

The SEM images of the powder and monolith samples are illustrated in Figure 4a-f. The low magnification SEM images (1 mm) in Figure 4a and 4d depict the cross sectional area with wall thickness and channel width of 0.4 and 0.7 mm respectively, for MOF-74(Ni) monolith and 0.8 and 1.1 mm respectively, for UTSA-16(Co) monolith. The reason for printing monoliths with different sizes was that the viscosity of the pastes were different for the two MOFs; for UTSA-16(Co) with higher viscosity (1659 kg/m^3),[33] a less viscous paste was prepared to avoid blockage and enhance extrusion. This was led to the expansion while depositing layers which eventually resulted in larger wall thickness and channel size for this MOF than for MOF-74 (Ni) with lower density (909 kg/m^3).[34] The high magnification SEM images of 3D-printed MOF-74(Ni) monolith captured at 5 and 1 µm resolution (Figure 4b and 4c) reveal the uniform distribution of MOF crystals with dimensions in the nano to micro size range. Similarly, the morphological investigation of the 3D-printed UTSA-16(Co) monolith revealed a porous structure with uniform distribution of MOF crystals and with voids and crystals having sizes on the micro-meso scale (Figure 4e and 4f).

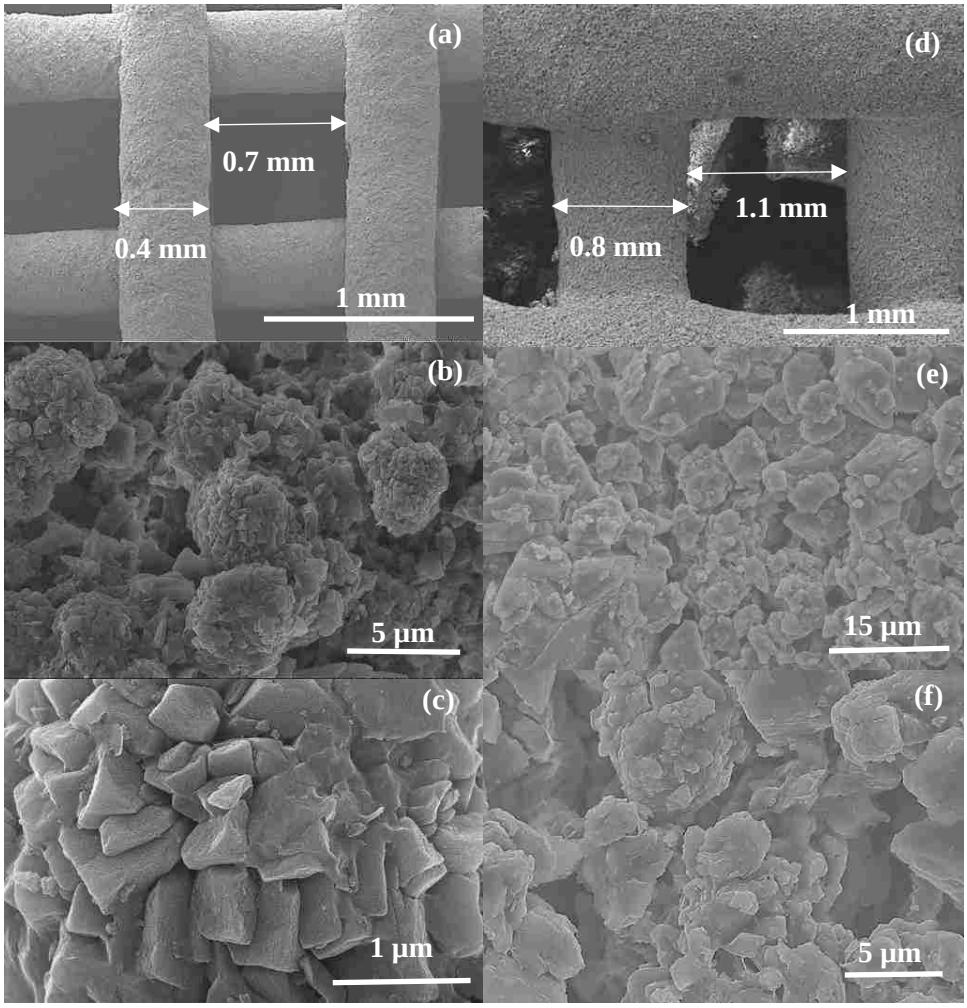

Figure 4. SEM images of 3D-printed (a-c) MOF-74(Ni) and (d-f) UTSA-16(Co) monoliths.

To measure and verify the amount of incorporated additives, thermogravimetric analysis experiments were conducted on TGA and the corresponding profiles are displayed in Figure 5a-b. The derivative weight (DW) peaks below 150 ºC in both Figures are assigned to the removal of moisture from all the samples. The differential peaks centered at 310-350 ºC in the curves of 3D-printed MOF monoliths are associated with the PVA

mass decomposition, as also evident from the profiles of pure PVA in Figure 5c. The weight loss in this range was about 5%, which is close to the nominal amount of PVA in

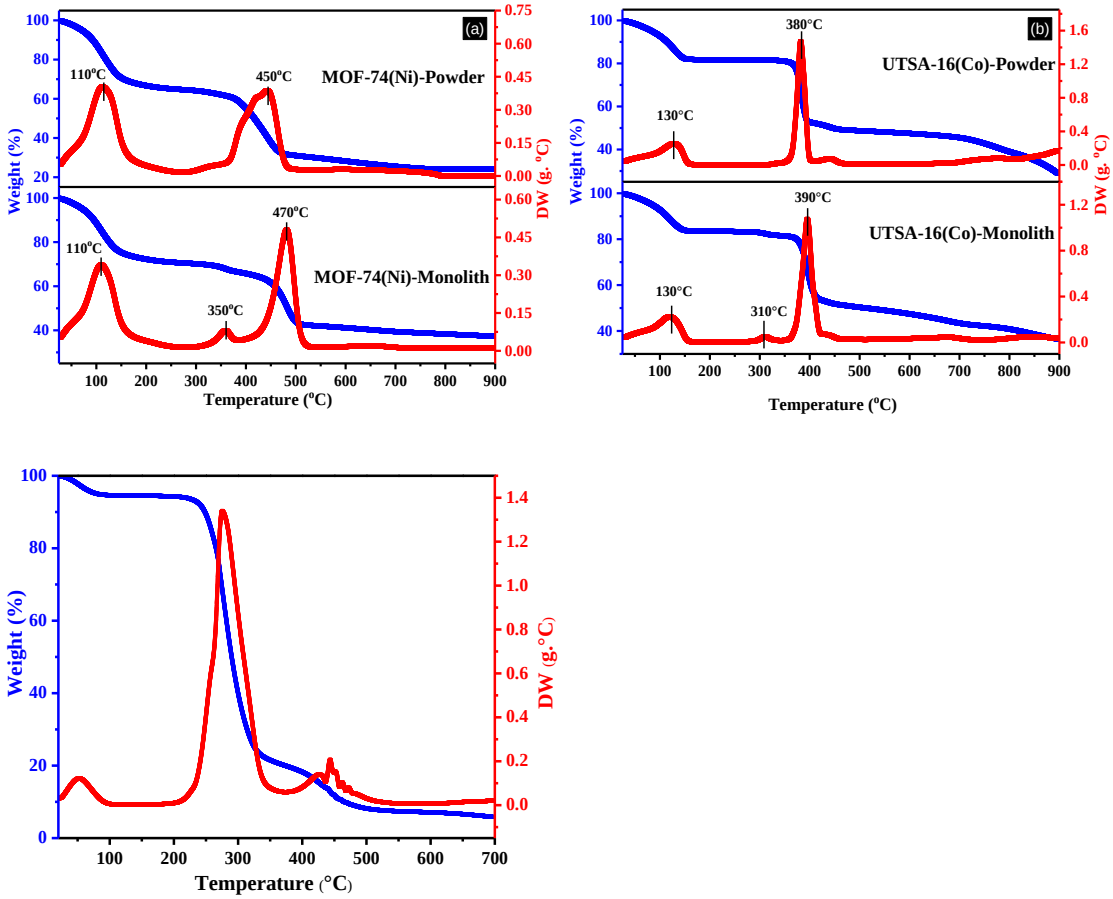

Figure 5. Thermogravimetry and differential thermogravimetry curves for 3D-printed (a) MOF-74(Ni) (b) UTSA-16(CO) monoliths and their corresponding powders and (c) PVA.

the printed monoliths. The other intensive peaks at 450-470 and 380-390 ºC are attributed to the thermal decomposition of MOF-74(Ni) and UTSA-16(Co) structures, respectively. At temperatures above 600 ºC, the difference in mass between the powders and 3D printed monoliths was found to be ~13% and ~8% in MOF-74(Ni) and UTSA-16(Co),

respectively, which was close to the nominal weight fractions of the binder used in preparation step (see Table 1).

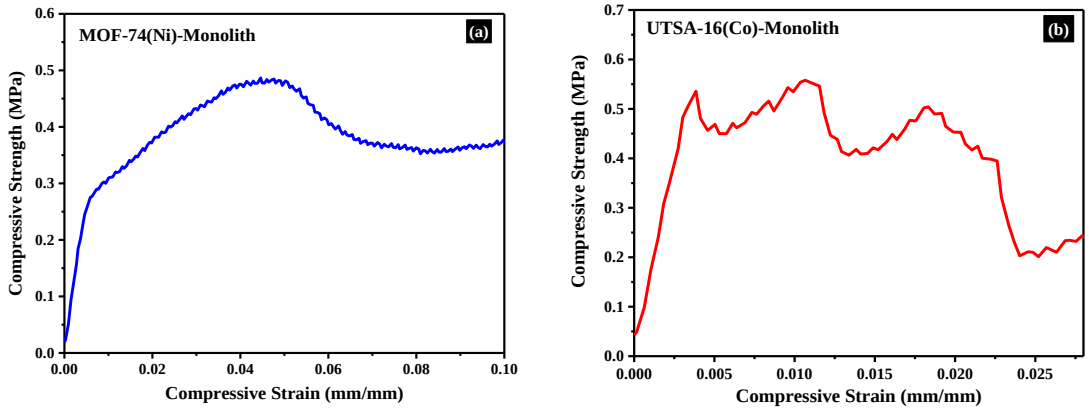

Figure 6. Comparison of stress-strain curves for (a) MOF-74(Ni) and (b) UTSA-16(Co) 3D-printed monoliths.

The mechanical testing results of 3D-printed monoliths are displayed in Figure 6 and the corresponding Young's modulus data calculated from the compressive strength-strain curves are tabulated in Table 3. As can be seen, the recorded compressive strengths before

Table 3. Mechanical testing data for 3D-printed MOF monoliths.

Sample	Compression strength (MPa)	Young's modulus (MPa)
MOF-74(Ni)-Monolith	0.48	12
UTSA-16(Co)-Monolith	0.55	25

catastrophic failure were found to be ~0.48 MPa (Figure 6a) and ~0.56 MPa (Figure 6b) for 3D-printed MOF-74(Ni) and UTSA-16(Co) monoliths, respectively. The higher strength of UTSA-16(Co) monolith could be associated with the dense nature of UTSA-16(Co) powder in comparison to the MOF-74(Ni), while its earlier fracture could be

attributed to its mesopore nature (see Table 2) that was generated due to the reaction of hydroxyl groups of water with the citrate units of UTSA-16(Co), as mentioned earlier.

3.2. CO_2 ADSORPTION PERFORMANCE OF 3D-PRINTED MOF MONOLITHS

The equilibrium CO_2 adsorption capacities of 3D-printed MOF monoliths and their corresponding powders were measured using TGA at 25 ºC and 1 bar at two different concentrations, namely 3,000 (0.3%) and 5,000 (0.5%) ppm CO_2 in N_2 to mimic the lower and upper bound levels of CO_2 in enclosed environments.[7] As Figure 7a-b shows, both 3D-printed MOF monoliths exhibited comparable capacities to their powder counterparts at both CO_2 concentrations. The CO_2 uptake of 3D-printed MOF-74(Ni) and UTSA-16(Co) monoliths were found to be 1.35 and 1.31 mmol/g, respectively at 0.5% CO_2/N_2, which were about 79% and 87% of that of MOF powders, consistent with the MOF loading of the monolith in both cases. The change in the porosity of the 3D-printed UTSA-16(Co) monolith did not influence its capture capacity which is in agreement with the results obtained by Masala et al.[30] under dry and wet conditions.

Furthermore, we assessed the stability of the 3D-printed MOF monoliths along with their powder analogues by performing cyclic tests at 25 ºC and 1 bar under pure CO_2 using TGA. The calculated capacities at five consecutive cycles are presented in Figure 8a-b. As can be clearly seen from this figure, like their powder analogues, both 3D-printed MOF-74(Ni) and UTSA-16(Co) monoliths retained their capacities with no considerable capacity loss after the fifth cycle. Although, rigorous tests should be conducted to analyze the stability of the MOF monoliths under realistic conditions (e.g. humid feed, more cycles, etc.) we believe that these preliminary results are indicative of stability of the printed monoliths.

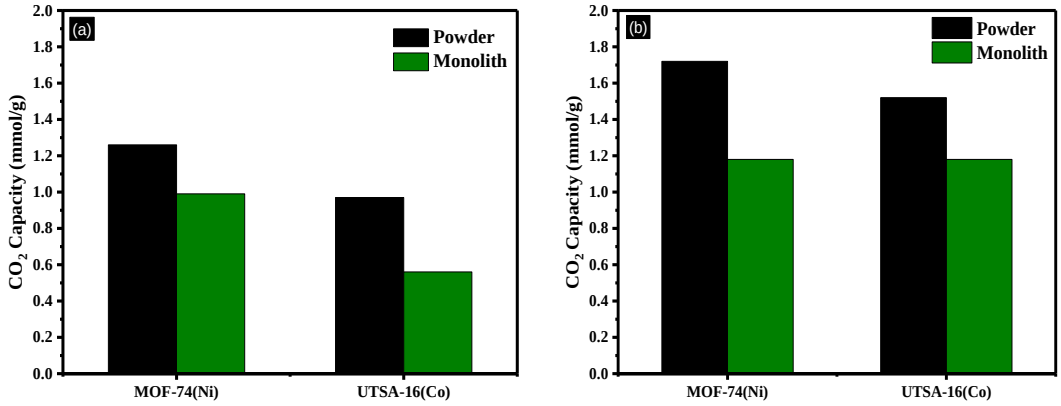

Figure 7. CO_2 capacity of 3D-printed MOF monoliths and corresponding powders under (a) 3,000 and (b) 5,000 ppm CO_2/N_2 at 25 ºC and 1 bar.

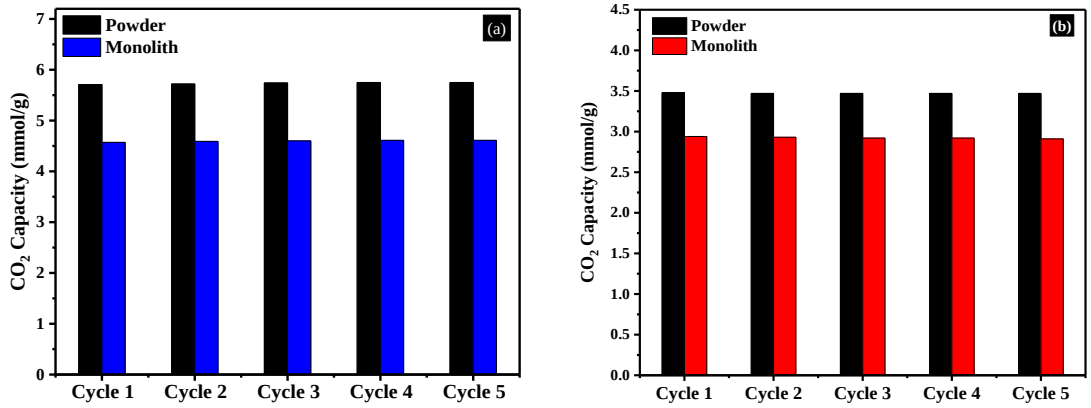

Figure 8. CO_2 Cyclic capacities of 3D-printed (a) MOF-74(Ni) and (b) UTSA-16(Co) monoliths with their corresponding powders at 25ºC and 1 bar.

In addition to single point capacity measurements, the CO_2 adsorption isotherms of 3D-printed MOF monoliths and powders were also measured at 25 °C, as shown in Figure 9a-b. Similar to the MOF powders, a relatively sharp uptake was observed at low partial pressures up to 0.15 bar followed by a gradual increase from 0.15 to 1.1 bar, which resembles the typical trend of CO_2 adsorption over microporous materials. Moreover, over the entire pressure range studied, both monoliths exhibited comparable capacity to their

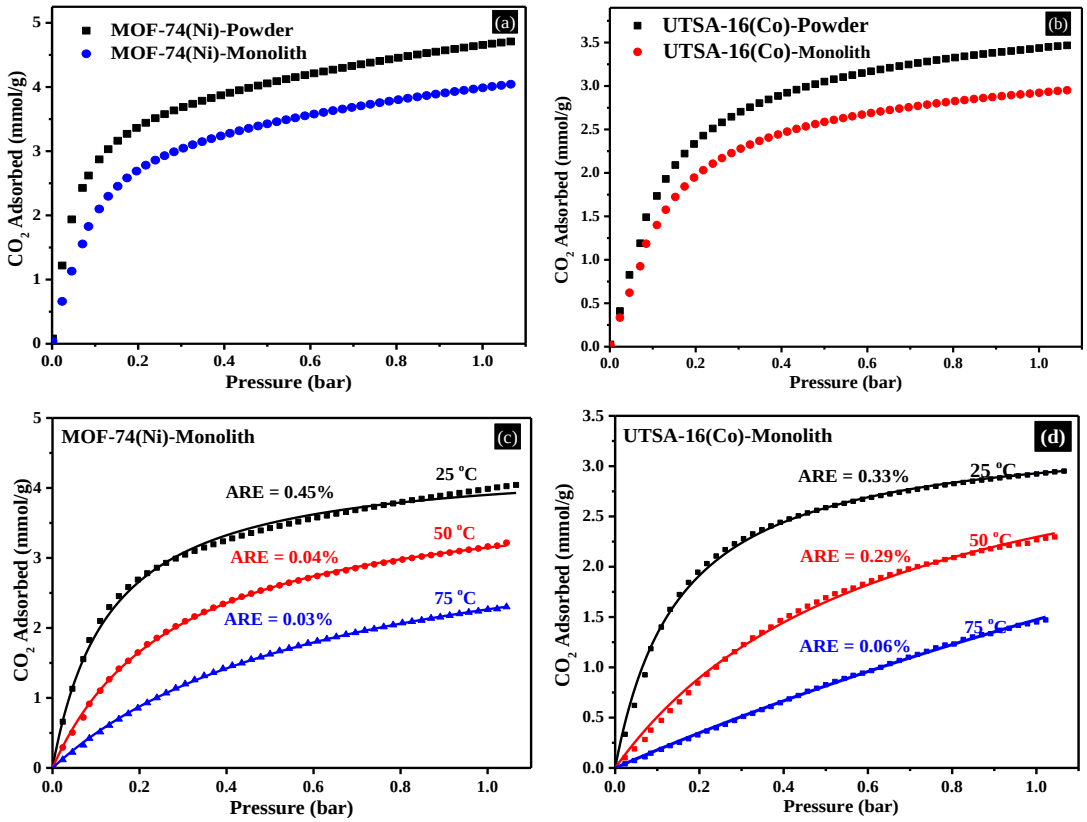

Figure 9. CO_2 adsorption isotherms of 3D-printed (a) MOF-74(Ni) and (b) UTSA-16(Co) monoliths and corresponding powders at 25°C. CO_2 adsorption isotherms of 3D-printed (c) MOF-74(Ni) and (d) UTSA-16(Co) monoliths at 25, 50 and 75 °C. Symbols show the experimental data and solid lines represent the fitted isotherms with average relative error (ARE).

corresponding powders. At 1.1 bar, a CO_2 uptake of 4.0 and 3.0 mmol/g was obtained for 3D-printed MOF-74(Ni) and UTSA-16(Co) monoliths, respectively in comparison to 4.7 and 3.5 mmol/g obtained for the powder analogues.

The CO_2 adsorption isotherms of printed monoliths measured at two other temperatures (50 and 75 ºC) are presented in Figure 9c-d. As expected, a decreasing trend in the quantity adsorbed with temperature was observed, while the isotherms stretched out more at higher temperatures. In addition, the single-site Langmuir model was used to fit the isotherms and the corresponding fitting parameters are listed in Table 4. As can be seen

from Figure 9c-d, relatively good fits with average relative error (ARE) of 0.45%, 0.04% and 0.03% were obtained for 3D-printed MOF-74(Ni) monolith isotherms and 0.33%, 0.29% and 0.06% for 3D-printed UTSA-16(Co) monolith at 25, 50 and 75 ºC, respectively.

Table 4. The fitting parameters of single-site Langmuir isotherm equation.

Adsorbent	**Temperature** (°C)	**q^*** (mmol/g)	**b** (bar^{-1})
MOF-74(Ni)-Monolith	25	4.41	7.63
	50	4.05	3.46
	75	3.74	1.52
UTSA-16(Co)-Monolith	25	3.77	6.53
	50	3.37	3.11
	75	2.64	1.12

Comparing the saturated capacity values (q^*) of the self-standing MOF monoliths with those of MOF-coated cordierite monoliths reported previously,[22] much higher values were obtained for our 3D-printed monoliths which further confirms their superior advantage. Furthermore, the isosteric heat of CO_2 adsorption (Q_{st}) was calculated using Van't Hoff equation from the fitting parameters and the corresponding curves are presented in Figure 10. As can be seen, for both cases, the Q_{st} shows a downward trend with CO_2 loading, consistent with previously published results. For 3D-printed MOF-74(Ni) monolith, Q_{st} was estimated to be in the range of 31-35 kJ/mol, while higher values of isosteric heats of adsorption have been previously reported for this MOF(38-43 kJ/mol).[35] For 3D-printed UTSA-16(Co) monolith, the estimated Q_{st} values varied from 29 to 33 kJ/mol which was slightly lower than previously reported values (38-40 kJ/mol).[32]

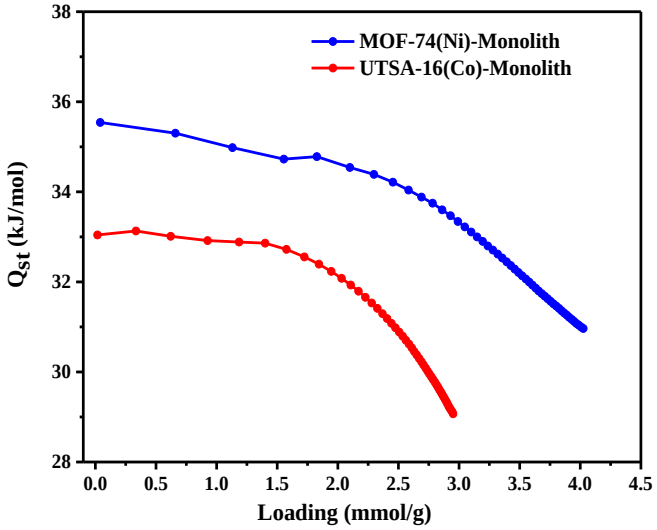

Figure 10**.** Isosteric heats of adsorption of CO_2 in 3D-printed MOF-74 (Ni) and UTSA-16(Co) monoliths.

The dynamic adsorption performance of 3D-printed UTSA-16(Co) monolith was investigated using 5,000 ppm CO_2/N_2 at 25 ºC and compared with its powder analogue. The corresponding breakthrough profiles are shown in Figure 11. A sharper front was obtained for 3D-printed UTSA-16(Co) monolith than the MOF powder under the same conditions. Additionally, an earlier CO_2 breakthrough time over the monolith (42 min) than over the MOF powder (57 min) was the result of its lower capacity, as discussed before. Table 5 tabulates the breakthrough times at 5, 50 and 95% normalized outlet concentration (C/C_0), breakthrough width and pseudo adsorption capacity (q_{pseudo}) estimated at 95% C/C_0. As evident from the data, the smaller breakthrough width (10 min) of the 3D-printed UTSA-16(Co) monolith indicates a faster adsorption kinetics than the corresponding powder (15 min). Moreover, the calculated q_{pseudo} values were found to be close to the equilibrium adsorption capacities (see Figure 7b).

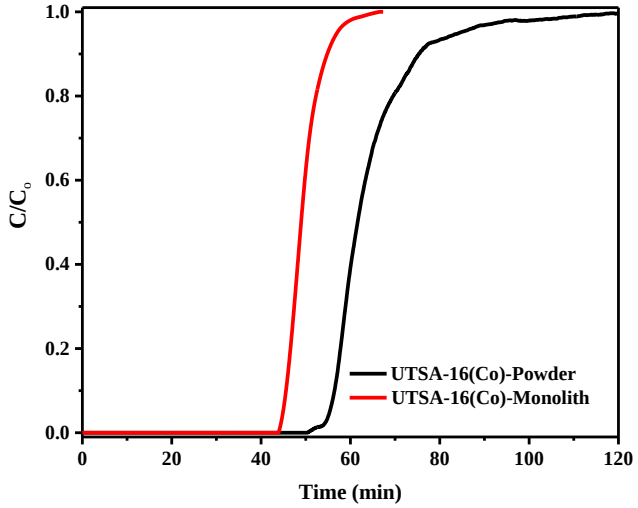

Figure 11**.** Breakthrough profiles of 3D-printed UTSA-16(Co) monolith and its corresponding powder using 5,000 ppm/N_2 at 25 °C.

Table 5. Dynamic adsorption data for 3D-printed UTSA-16(Co) monolith and powder.

Sample	$t_{5\%}$ (min)	$t_{50\%}$ (min)	$t_{95\%}$ (min)	**Breakthrough width** (min)	q_{pseudo} (min)
UTSA-16(Co)-Powder	57	62	72	15	1.48
UTSA-16(Co)-Monolith	42	46	52	10	1.25

4. CONCLUSION

In this preliminary investigation, the application of 3D printing technique to formulate MOF adsorbents into monolithic contactors that could eventually be applied to large-scale applications was investigated. The 3D-printed MOF-74(Ni) and UTSA-16(Co) monoliths with MOF loadings as high as 80 and 85 wt %, respectively, were fabricated using our lab-scale 3D printer and investigated for CO_2 removal from air. The physical, structural and mechanical properties of 3D printed monoliths were evaluated and compared to their powder counterparts. The obtained results reveal that the monoliths fabricated by 3D printing technique retain their physical properties and mechanical integrity. In addition,

3D-printed MOF-74(Ni) and UTSA-16(Co) monoliths exhibited comparable CO_2 capture capacity to the MOF powders with stable performance and relatively faster adsorption kinetics. Although more work needs to be done to optimize the formulation and fine-tune the characteristics of the monoliths, we believe this work provides a new proof-of-concept prospect for fabricating MOF monoliths that can be used for various adsorptive-based separation processes.

ACKNOWLEDGEMENT

This work was financially supported by the NASA-EPSCoR (NNX15AK38A). The authors thank Materials Research Center (MRC) of Missouri S&T for SEM and XRD.

REFERENCES

(1) Rezaei, F.; Webley, P. Structured Adsorbents in Gas Separation Processes. *Sep. Purif. Technol.* **2010**, *70* (3), 243–256.

(2) Rezaei, F.; Webley, P. Optimum Structured Adsorbents for Gas Separation Processes. *Chem. Eng. Sci.* **2009**, *64* (24), 5182–5191.

(3) Taranco, A.; Me, J.; Herna, L.; Ferna, R. Three Dimensional Printing of Components and Functional Devices for Energy and Environmental Applications. *Energy Environ. Sci.* **2017**, *10*, 846–859.

(4) Zhou, X.; Liu, C. Three-Dimensional Printing for Catalytic Applications : Current Status and Perspectives. *Adv. Funct. Mater.* **2017**, *1701134*, 1–13.

(5) Low, Z.-X.; Chua, Y. T.; Ray, B.; Mattia, D.; Metcalfe, I.; Patterson, D. A. Perspective on 3D Printing of Separation Membranes and Comparison To Related Unconventional Fabrication Techniques. *J. Membr. Sci.* **2017**, *523*, 596–613.

(6) Tubío, C. R.; Azuaje, J.; Escalante, L.; Coelho, A.; Guitián, F.; Sotelo, E.; Gil, A. 3D Printing of a Heterogeneous Copper-Based Catalyst. *J. Catal.* **2016**, *334* (January), 110–115.

(7) Thakkar, H. V.; Eastman, S.; Hajari, A.; Rownaghi, A. A.; Knox, J. C.; Rezaei, F. 3D-Printed Zeolite Monoliths for CO_2 Removal from Enclosed Environments. *ACS Appl. Mater. Interfaces* **2016**, *8*, 27753−27761.

(8) Thakkar, H.; Eastman, S.; Al-Mamoori, A.; Hajari, A.; Rownaghi, A. A.; Rezaei, F. Formulation of Aminosilica Adsorbents into 3D-Printed Monoliths and Evaluation of Their CO_2 Capture Performance. *ACS Appl. Mater. Interfaces* **2017**, *9*, 7489–7498.

(9) Couck, S.; Lefevere, J.; Mullens, S.; Protasova, L.; Meynen, V.; Desmet, G.; Baron, G. V.; Denayer, J. F. M. M. CO_2, CH_4 and N_2 Separation with a 3DFD-Printed ZSM-5 Monolith. *Chem. Eng. J.* **2017**, *308*, 719–726.

(10) Couck, S.; Cousin, J.; Remi, S.; Perre, S. Van Der; Baron, G. V; Ruch, P.; Denayer, J. F. M. 3D-Printed SAPO-34 Monoliths for Gas Separation. *Microporous Mesoporous Mater.* **2017**, doi.org/10.1016/j.micromeso.2017.07.014.

(11) Li, J.; Sculley, J.; Zhou, H. Metal-Organic Frameworks for Separations. *Chem. Rev.* **2012**, *112*, 869–932.

(12) Walton, K. S. Metal-Organic Frameworks: Recognizing the Unrecognizable. *Nat. Chem.* **2014**, *6* (4), 277–278.

(13) Zhang, Z.; Yao, Z.; Xiang, S.; Chen, B. Perspective of Microporous Metal-Organic Frameworks for CO_2 Capture and Separation. *Energy Environ. Sci.* **2014**, *7* (9), 2868–2899.

(14) Remy, T.; Peter, S. A.; Van Der Perre, S.; Valvekens, P.; De Vos, D. E.; Baron, G. V.; Denayer, J. F. M. Selective Dynamic CO_2 Separations on Mg-MOF-74 at Low Pressures: A Detailed Comparison with 13X. *J. Phys. Chem. C* **2013**, *117*, 9301−9310.

(15) Ren, J.; Musyoka, N. M.; Langmi, H. W.; Swartbooi, A.; North, B. C.; Mathe, M. A More Efficient Way to Shape Metal-Organic Framework (MOF) Powder Materials for Hydrogen Storage Applications. *Int. J. Hydrogen Energy* **2015**, *40* (13), 4617–4622.

(16) Grande, C. A.; Águeda, V. I.; Spjelkavik, A.; Blom, R. An Efficient Recipe for Formulation of Metal-Organic Frameworks. *Chem. Eng. Sci.* **2015**, *124*, 154–158.

(17) Pimentel, B. R.; Fultz, A. W.; Presnell, K. V; Lively, R. P. Synthesis of Water-Sensitive Metal − Organic Frameworks within Fiber Sorbent Modules. *Ind. Eng. Chem. Res.* **2017**, *56*, 5070−5077.

(18) Ramos-Fernandez, E. V.; Garcia-Domingos, M.; Juan-Alcañiz, J.; Gascon, J.; Kapteijn, F. MOFs Meet Monoliths: Hierarchical Structuring Metal Organic Framework Catalysts. *Appl. Catal. A.* **2011**, *391* (1–2), 261–267.

(19) Sachse, A.; Ameloot, R.; Coq, B.; Fajula, F.; Coasne, B.; De Vos, D.; Galarneau, A. In Situ Synthesis of Cu–BTC (HKUST-1) in Macro-/mesoporous Silica Monoliths for Continuous Flow Catalysis. *Chem. Commun.* **2012**, *48* (39), 4749–4751.

(20) Wang, Z.; Liu, J.; Grosjean, S.; Wagner, D.; Guo, W.; Gu, Z.; Heinke, L.; Gliemann, H.; Bräse, S.; Wöll, C. Monolithic, Crystalline MOF Coating: An Excellent Patterning and Photoresist Material. *ChemNanoMat* **2015**, *1*, 338–345.

(21) Rezaei, F.; Lawson, S.; Hosseini, H.; Thakkar, H.; Hajari, A.; Monjezi, S.; Rownaghi, A. A. A. MOF-74 and UTSA-16 Film Growth on Monolithic Structures and Their CO_2 Adsorption Performance. *Chem. Eng. J.* **2017**, *313*, 1346–1353.

(22) Lawson, S.; Hajari, A.; Rownaghi, A. A.; Rezaei, F. MOF Immobilization on the Surface of Polymer-Cordierite Composite Monoliths through in-Situ Crystal Growth. *Sep. Purif. Technol.* **2017**, *183*, 173–180.

(23) Darunte, L. A.; Terada, Y.; Murdock, C. R.; Walton, K. S.; Sholl, D. S.; Jones, C. W. Monolith-Supported Amine-Functionalized Mg_2(dobpdc) Adsorbents for CO_2 Capture. *ACS Appl. Mater. Interfaces* **2017**, *9*, 17042−17050.

(24) Shekhah, O.; Liu, J.; Fischer, R. a.; Wöll, C. MOF Thin Films: Existing and Future Applications. *Chem. Soc. Rev.* **2011**, *40* (2), 1081−1106.

(25) Küsgens, P.; Zgaverdea, A.; Fritz, H. G.; Siegle, S.; Kaskel, S. Metal-Organic Frameworks in Monolithic Structures. *J. Am. Ceram. Soc.* **2010**, *93* (27092), 2476–2479.

(26) Hong, W. Y.; Perera, S. P.; Burrows, A. D. Manufacturing of Metal-Organic Framework Monoliths and Their Application in CO_2 Adsorption. *Microporous Mesoporous Mater.* **2015**, *214*, 149–155.

(27) Moitra, N.; Fukumoto, S.; Reboul, J.; Sumida, K.; Zhu, Y.; Nakanishi, K.; Furukawa, S.; Kitagawa, S.; Kanamori, K. Mechanically Stable, Hierarchically Porous $Cu_3(btc)_2$(HKUST-1) Monoliths via Direct Conversion of Copper(ii) Hydroxide-Based Monoliths. *Chem. Commun.* **2015**, *51* (17), 3511–3514.

(28) Grant Glover, T.; Peterson, G. W.; Schindler, B. J.; Britt, D.; Yaghi, O. MOF-74 Building Unit Has a Direct Impact on Toxic Gas Adsorption. *Chem. Eng. Sci.* **2011**, *66* (2), 163–170.

(29) Wu, X.; Bao, Z.; Yuan, B.; Wang, J.; Sun, Y.; Luo, H.; Deng, S. Microwave Synthesis and Characterization of MOF-74 (M = Ni, Mg) for Gas Separation. *Microporous Mesoporous Mater.* **2013**, *180*, 114–122.

(30) Masala, A.; Vitillo, J. G.; Mondino, G.; Grande, C. A.; Blom, R.; Manzoli, M.; Marshall, M.; Bordiga, S. CO_2 Capture in Dry and Wet Conditions in UTSA-16 Metal − Organic Framework. *ACS Appl. Mater. Interfaces* **2017**, *9*, 455−463.

(31) Brennan, P. J.; Thakkar, H.; Li, X.; Rownaghi, A. A.; Koros, W. J.; Rezaei, F. Effect of Post-Functionalization Conditions on the Carbon Dioxide Adsorption Properties of Aminosilane-Grafted Zirconia /Titania/Silica-Poly (Amide-Imide) Composite Hollow Fiber Sorbents. *Energy Technol.* **2017**, *5*, 327–337.

(32) Chem, P.; Phys, C.; Grande, C. A.; Bordiga, S. New Insights into UTSA-16. *Phys. Chem. Chem. Phys.* **2015**, *18*, 220–227.

(33) Xiang, S.; He, Y.; Zhang, Z.; Wu, H.; Zhou, W.; Krishna, R.; Chen, B. Microporous Metal-Organic Framework with Potential for Carbon Dioxide Capture at Ambient Conditions. *Nat. Commun.* **2012**, *3*, 954.

(34) Yabing He, Rajamani Krishna, B. C. Metal–organic Frameworks with Potential for Energy-Efficient Adsorptive Separation of Light Hydrocarbons. *Energy Environ. Sci.* **2012**, *5*, 9107–9120.

(35) Dietzel, P. D. C.; Besikiotis, V.; Blom, R.; Application of Metal–organic Frameworks with Coordinatively Unsaturated Metal Sites in Storage and Separation of Methane and Carbon Dioxide. *J. Mater. Chem.* **2009**, *19* (39), 7362–7370.

IV. CO_2 CAPTURE FROM AIR USING AMINE FUNCTIONALIZED KAOLIN-BASED ZEOLITES

Harshul Thakkar, Ahlam Issa, Ali A. Rownaghi, Fateme Rezaei*

Department of Chemical and Biochemical Engineering, Missouri University of Science and Technology, 1101 N State St., Rolla, MO 65409, United States
Email: rezaeif@mst.edu

ABSTRACT

In this study, we developed several inexpensive zeolites such as ZSM-5 (MFI), zeolite Y (FAU) and SAPO-34 (CHA) from kaolin clay and applied them for CO_2 capture from air. These molecular sieves were functionalized with tetraethylenepentamine (TEPA) to further improve their CO_2 capacity. The obtained kaolin-based zeolites exhibited similar properties than those of zeolites prepared with other sources. They also exhibited a bimodal pore network consisting of both micropores and mesopores. The effect of amine loading on CO_2 capture was investigated and our results demonstrated that TEPA-modified zeolite Y with 10 wt% TEPA exhibited higher capacity than other zeolites due to its larger mesopore volume. The presence of mesopores in zeolite Y framework facilitated a better accessibility of CO_2 molecules to the amine sites.

Keywords: Kaolin-based zeolites, TEPA impregnation, CO_2 capture from air

1. INTRODUCTION

Direct extraction of CO_2 from air, commonly referred to as air capture, offers a viable option for reducing greenhouse gas levels. This “negative carbon” technology that focuses essentially on removing CO_2 from air has been shown to provide potential advantages over conventional CO_2 capture strategies that focus primarily on lowering the rate of emissions to the atmosphere.[1–4] Air capture process can be implemented using either aqueous

hydroxides such as calcium hydroxide solution, NaOH and KOH solutions, or solid adsorbents such as alkali and alkali-supported carbonates, anionic-exchange resins, amine-functionalized metal oxides, and metal-organic frameworks (MOFs).[5–7]

In particular, supported amine adosrbents, mainly aminosilica materials, have been shown as promising candidates for removing ultra-low CO_2 concentration from air.[8–10] In addition, with the aim of combining the advantages of supported amines and zeolites, several attempts have been undertaken to develop hybrid adsorbents by incorporating amine moieties into the framework of zeolites.[11] For example, Jadhav et al.[12] synthesized monoethanol amine (MEA)-modified 13X zeolite for CO_2 capture and the authors reported improvements in adsorption capacity (by a factor of 1.6 at 30 °C. In another investigation, Lee et al.[13] developed a series of amine-impregnated zeolite Y and evaluated them for CO_2 removal from indoor air. More recently, Xu et al.[14] incorporated MEA into β-zeolite and evaluated it for separation of CO_2, CH_4, and N_2. It was shown that the introduction of MEA significantly improved the selectivity of both CO_2/CH_4 and CO_2/N_2. In another study,[15] mesoporous SAPO-34 grafted with 3-aminopropyltrimethoxysilane (APS) was used for CO_2 capture and it was shown that although the capacity of NH_2-SAPO-34 was lowered compared to the bare mesoporous SAPO-34 (1.77 mmol/g compared to 3.2 mmol/g at 298 K and 1 bar), it exhibited a sharper breakthrough front.

The successful incorporation of amine moieties into the zeolite crystal structure and hence the subsequent improvement in capture capacity depends largely on the pore network and pore size in the zeolite framework. Modifying a microporous zeolite with amines likely results in blockage of most of the pores and hence reduction in available surface area for adsorption, whereas mesoporous zeolites with larger pore dimension can be readily

modified with amines with less degree of pore blockage and good amine distribution. In addition to zeolite pore structure, amine loading should be optimized to ensure high accessibility of CO_2 molecules to both zeolite and amine sites. High amine loading usually increases the diffusion limitations and pore blockage of mesoporous supports while low amine loading does not contribute to enhanced adsorption capacity that much.[16] Moreover, the amine structure (i.e. primary, secondary, tertiary) may affect the ultradilute CO_2 capture on modified zeolites, as it has been previously shown for aminosilica adsorbents.[17]

In a typical synthesis of zeolites, two different templates (i.e., triethylamine and tetraethylammoniumhydroxide,) and an additional source of silica (i.e., tetraethoxysilane) are generally used. A simpler and more environmentally friendly synthesis route that employs less chemicals appears to be an economic approach. In that regard, the synthesis of zeolites from kaolin has been shown to employ only a single template with no additional silica source.

Typical synthesis of zeolites requires sources of silicon (e.g. tetraethyl orthosilicate; TEOS) and aluminum (e.g. aluminium isopropoxide; $Al(O\text{-}i\text{-}Pr)_3$), organic molecules as templating agent such as tetrapropyl ammonium bromide (TPA-Br), tetrapropyl ammonium hydroxide (TPA-OH), trimethylamine (TEA) and a mineralizer (e.g. OH^- or F^-).[18–22] Unfortunately, these template agents are rather expensive. In recent years, efforts have also been undertaken to identify low cost sources of SiO_2 and Al_2O_3 to synthesize less expensive zeolites and kaolin clay has been identified as a suitable and an inexpensive sources of silica and alumina. Another advantage of using kaolin as the synthesis source is

that unlike traditional synthesis methods, only a single template with no additional source of silica is required.[22–25]

In this study, we developed several zeolites, namely ZSM-5 (MFI), zeolite Y (FAU), and SAPO-34 (CHA) from kaolin clay and further impregnated with tetraethylenepentamine (TEPA). The structural, physical, and chemical properties of the amine-modified zeolites were characterized and the effect of amine loading on CO_2 adsorption capacity was investigated. Moreover, the dynamic performance and stability of the impregnated adsorbents were evaluated and compared with that of the bare zeolites. The novelty of the present work lies in the development of kaolin-based zeolites with bimodal pore structure that could be functionalized with aminopolymers to enhance their adsorption performance.

2. EXPERIMENTAL SECTION

2.1. SYNTHESIS OF KAOLIN-BASED ZEOLITES

ZSM-5: ZSM-5 was synthesized according to a procedure developed by Mohiuddin et al.[26] Kaolin (Sigma Aldrich) was first calcined at 750 °C for 2 h at the rate of 5-8 °C/min in a Thermo Scientific Thermolyne furnace in order to achieve a meta-kaolin phase. The meta-kaolin was then leached by mixing with hydrochloric acid (37 wt % HCL, Sigma Aldrich) with weight ratio of 1:17 solid to acid for 2.5 h at 115 °C. After washing and filtrating, the material was dried in the oven at 100 °C overnight. In the next step, gel formation was conducted by aging the mixture of leached meta-kaolin, N-butyl amine (NBA, Sigma Aldrich), distilled water, and NaOH (Sigma Aldrich) with molar ratios of Na_2O/SiO_2 = 0.18, SiO_2/Al_2O_3 = 33, SiO_2/NBA = 7, and H_2O/SiO_2 = 30 for 24 h at room temperature. During hydrothermal treatment, the gel was transferred into the stainless steel autoclave and heated at 165 °C for 24 h in an oil bath. After the hydrothermal reaction, a

solid cake was recovered from the slurry by filtration and washed with distilled water. A crystalline product was obtained by drying the solid cake at 120 °C in air for 2 h followed by calcination at 550 °C for 2 h to remove the template (NBA). H-type ZSM-5 zeolite was prepared through the ion exchange of the calcined product with aqueous ammonium nitrate (NH_4NO_3) at 80 °C followed by filtration, drying and calcination at 550 °C for 2 h.

Zeolite Y: Zeolite Y (ZY) was prepared from kaolin by following a previously reported procedure.[27] Briefly, the kaolin was calcined at 900 °C for 1 h to obtain a meta-kaolin phase. Then, desired amounts of NaOH and sodium silicate were mixed with the 1 g of meta-kaolin to obtain a reaction mixture with different molar ratios: SiO_2/Al_2O_3 = 5-15, Na_2O/SiO_2 = 0.5-1, and H_2O/Na_2O = 20-30. It was observed that ageing is essential to achieve a pure phase ZY. As the aging time was increased from 1 to 10 days, the crystallinity was found to increase and a highly crystalline ZY was obtained. The mixture was then transferred into a stainless steel autoclave and heated at 95-105 °C for 16 h in an oil bath. Then, the cake was filtered, washed and dried at 100 °C overnight. Finally, the ion exchange step was carried out by mixing NH_4NO_3 with zeolite NaY with 1:10 weight ratio of solid to liquid at 95 °C on reflux.

SAPO-34: In the typical synthesis of the zeolite SAPO-34, pretreated kaolin clay (10.9 g, calcined at 750 °C for 2 h) and triethylamine (18.7 g, TEA, 99 wt%, as the micropore template) were mixed with orthophosphoric acid (18.6 g, H_3PO_4, 85 wt%). Then, deionized water (50 g) was added to the mixture. After stirring for 2-4 h and aging for 24 h at room temperature, the mixture was transferred into a stainless-steel autoclave and heated at 185 °C for 72 h under autogenous pressure. In the next step, the product

was filtrated, washed, and dried at 110 °C. Then, the sample was calcined at 600 °C for 4.5 h to remove the template.[23,28]

2.2. AMINE FUNCTIONALIZATION

Amine impregnation of kaolin-based zeolites was carried by the wet impregnation method according to the literature.[17,29] Briefly, about 1 g of zeolite sample was degassed at 250 °C overnight and then a desired amount of TEPA was dissolved into methanol for 2 h at room temperature. Then, the degassed zeolite was added to the methanol-amine solution and was allowed to stir for 24 h. The solution was then transferred to rotary-evaporator to extract methanol, followed by drying at 80 °C under vacuum overnight. The amine amount was varied from 5 to 20 wt% to evaluate its effect on CO_2 capture capacity.

2.3. CHARACTERIZATION OF KAOLIN-BASED ZEOLITES

XRD analysis was carried out using PANalytical X'Pert Multipurpose X-ray Diffractometer. The diffraction patterns of the bare and amine-modified samples were collected to assess their crystal structure using Cu Kα (1.540598 Å) radiation in the 2θ range from 5° to 50°. To confirm successful impregnation of TEPA, FTIR spectra were obtained on Nicolet Nexus 470 spectrometers. Nitrogen physisorption measurements were performed at 77 K on a Micromeritics 3Flex gas analyzer to investigate the physical properties of the kaolin-based molecular sieves. Preparation of amine functionalized zeolite samples was accomplished by degassing samples at 80 °C for 2-3 h. The obtained isotherms were used to evaluate the micro and mesopore volumes, surface area, and pore size distribution (PSD). The total pore volume was estimated at a relative pressure of 0.99, while the surface area was calculated using the Brunauer−Emmet-Teller (BET). To determine amine loading and evaluate amine efficiency, thermogravimetric analysis was

carried on TGA (Q500, TA Instruments) by varying temperature from 25 °C until 700 °C at the rate of 10 °C/min. The recorded weight loss was then used to calculate the amine loading.

2.4. CO_2 ADSORPTION MEASUREMENTS

To examine the efficacy of functionalized zeolites for capture of CO_2 from air, adsorption capacity measurements were performed on TGA (TA instrument, TGA Q500) by exposing the materials to 5,000 ppm CO_2 in dry N_2 (0.5% CO_2/N_2) at room temperature. The samples were first outgassed at 100 °C for 1 h in pure N_2 to remove pre-adsorbed molecules, moisture, and volatile compounds from the adsorbents. Temperature was then decreased to 25 °C and stabilized for 30 min prior to adsorption step. To check the stability of the materials, cyclic capacity measurements were also performed over five consecutive adsorption-desorption cycles by swinging the temperature between room temperature during adsorption and 100 °C during desorption.

2.5. CO_2 BREAKTHROUGH MEASUREMENTS

The dynamic performance of TEPA-impregnated zeolites was evaluated by performing breakthrough experiments in a fixed-bed column connected to a mass spectrometer (BELMASS Japan Inc.). The schematic of the breakthrough setup can be found in our previous publications.[30,31] About 0.5 g of the adsorbent was placed into a 2 cm × 30 cm glass column and outgassed at 100 °C for 2 h in N_2 with the flow rate of 40 mL min^{-1} to remove pre-adsorbed impurities. After this step, the adsorbent was exposed to 0.5% CO_2/N_2 with a flow rate of 40 mL min^{-1} at 25 °C and 1 bar.

3. RESULTS AND DISCUSSION

3.1. EFFECT OF TEPA CONTENT ON CO_2 ADSORPTION CAPACITY

Figure 1 shows normalized CO_2 adsorption capacity (obtained by dividing the capacity values by the highest capacity for each zeolite) as a function of TEPA loading for the three clay-based zeolites. As can be seen, for ZSM-5 and SAPO-34, the CO_2 adsorption capacity decreased with increasing amine loading from 5 to 20 wt%, whereas for ZY, a completely opposite trend was observed where the capacity increased with TEPA content. This observation could be correlated to the porosity of bare zeolites and as Table 1 shows, both ZSM-5 and SAPO-34 were essentially micoporous while ZY had a bimodal pore network consisting of both micro and mesopores. Increasing amine loading in the former zeolites resulted in pore blockage and subsequent decrease in CO_2 capacity, on the contrary, the presence of mesopores with larger mesopore volumes facilitated the TEPA impregnation

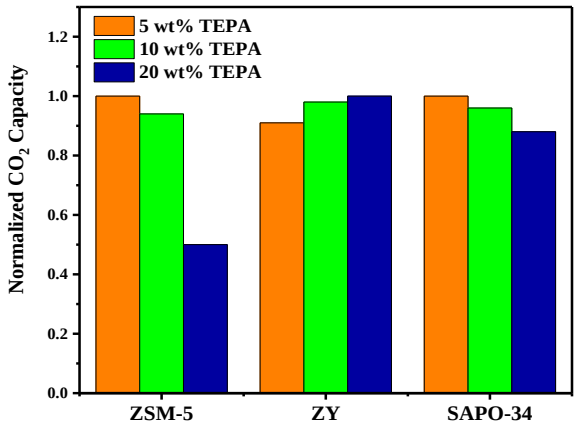

Figure 1. Normalized CO_2 adsorption capacity of ZSM-5, ZY, and SAPO-34 synthesized from kaolin as a function of amine loading at 25 ºC using 5000 ppm CO_2/N_2.

and better distribution of TEPA polymer chains in the pores. Further increase in amine loading can eventually fill the micropores and decrease the CO_2 uptake for this zeolite.

Based on these screening results, we selected 10 wt% TEPA-zeolite adsorbents for the rest of analyses.

3.2. CHARACTERIZATION OF BARE AND TEPA-ZEOLITES

Figure 2 displays the XRD patterns of kaolin-based zeolites. These XRD patterns reveal that all the characteristics peaks of the three zeolites were replicated confirming the successful formation of ZSM-5, ZY and SAPO-34 from kaolin. The peaks at 2θ = 7.9º, 8.9º, 23.3º, 24.5º and 26.8º which correspond to the planes (101), (200), (301), (501) (303), and (503) respectively, were associated with the ZSM-5 (MFI) framework.[32] Crystal structure of ZY consisted of planes (111), (220), (331), and (533) which were confirmed by peaks at 12º, 17º, 22º, and 26º as the characteristic peaks in FAU framework.[33] Low intensity peaks near 2θ = 21º, 26º, and 32º observed in the XRD spectrum of ZY were associated with zeolite P. The formation of zeolite P as an impurity in the zeolite Y can be attributed to insufficient aging time.[34] Diffraction pattern for SAPO-34 with corresponding planes (100), (101), (111), (201), (202), (301), and (311) represented the CHA zeolite structure when compared to the XRD pattern of SAPO-34 obtained from calcined kaolin microsphere.[23] The lower intensity of the XRD peaks of SAPO-34 could be associated with prolonged heating or stirring time.

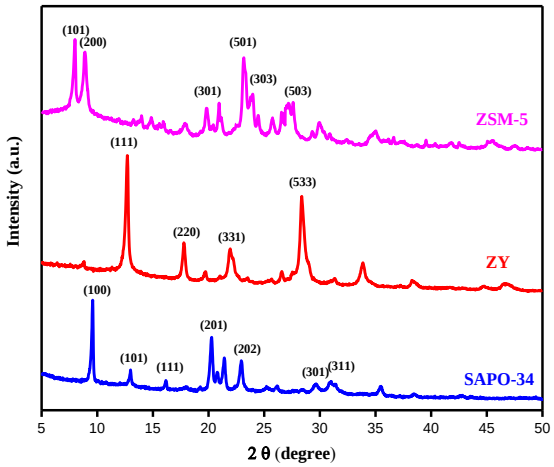

Figure 2**.** XRD patterns of ZSM-5, ZY, and SAPO-34 zeolites synthesized from kaolin clay.

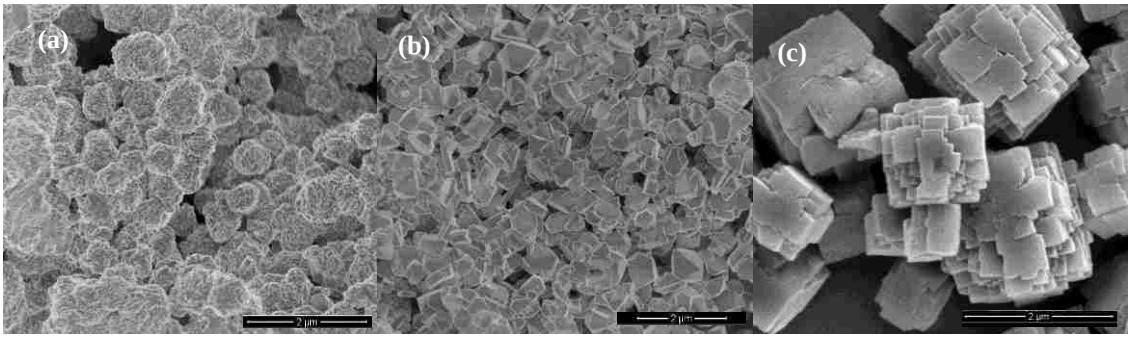

Figure 3**.** SEM images of (a) ZSM-5, (b) ZY, and (c) SAPO-34 zeolites synthesized from kaolin clay.

Figure 3 displays the SEM images of bare zeolites synthesized from kaolin clay. For all three cases, particles with uniform size were obtained. Further, the morphology of the obtained zeolite particles was found to be similar to that of zeolites prepared from other sources.[15,35–37] These SEM images further confirm the successful synthesis of zeolites for kaolin clay.

FTIR spectra of brae and TEPA-functionalized zeolites synthesized from kaolin are shown in Figure 4. The transmittance bands appeared in the range of 1400 to 1750 cm^{-1} were attributed to N-H and C-N stretching vibrations, respectively. In addition, a broad

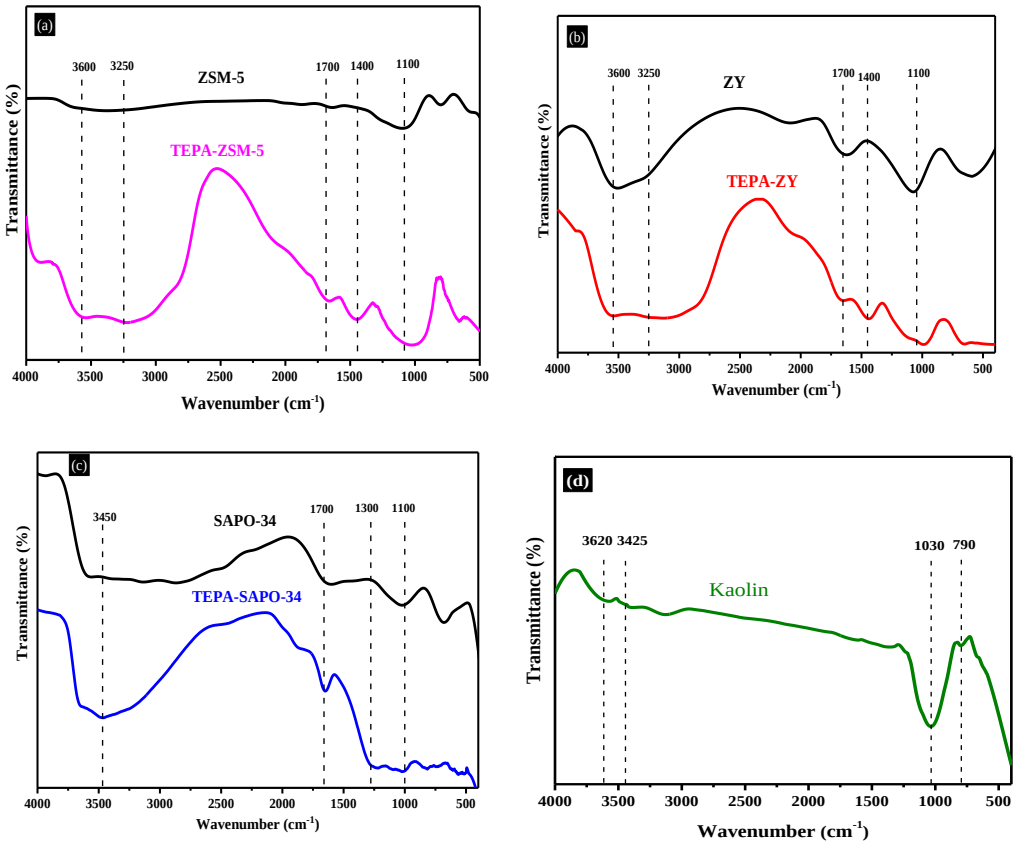

Figure 4. FTIR spectra of bare and TEPA-functionalized (a) ZSM-5, (b) ZY, (c) SAPO-34 synthesized from kaolin and (d) bare kaolin.

band at 2700-3800 cm^{-1} could also be attributed to the NH_3^+ stretching vibration.[38] The appearance of these bands at 1400-1750 and 2700-3800 cm^{-1} clearly confirmed the successful incorporation of TEPA into the zeolites framework since they do not appear in the spectra of bare zeolites or pristine kaolin (Figure 4d). Moreover, the peak at ~1700 cm^{-1} corresponded to – NH_3 + O-Si/NH_2 + O-Si while peaks between 3250 cm^{-1} and 3600 cm^{1}

were associated with silanol and hydroxyl groups, respectively and could be attributed to physisorbed moisture. Overall, by comparing the FTIR spectra of the bare and functionalized zeolites it is apparent that the amine moieties were indeed incorporatd into the pores of kaolin-based zeolites.

To determine the physical properties of zeolites synthesized from kaolin, N_2 physisorption was carried out on 3Flex (Micromeritics) at 77 K. Figure 5 displays adsorption and desorption isotherms which were of type IV for all zeolite samples indicating the occurrence of capillary condensation inside the mesopores.[39,40] Initially, at low relative pressures (P/P_0) up to 0.4, microporous nature of all zeolite samples was observed whereas gradual increase in N_2 uptake at higher partial pressures confirmed the presence of mesopores in the framework as a result of decomposition of surfactant during calcination process. Moreover, pore size distribution (PSD) curves presented in Figure 5 confirmed that the bimodal nature of the pores and structural and physical properties of TEPA-functionalized zeolites were retained. The first peak appeared in the range of 1-4 nm which revealed the microporous nature of all samples and also provides evidence of mesopores close to the range of micropores whereas the peak in the range of 40 nm clearly displayed mesoporousity in all samples. Moreover, the TEPA-functionalized zeolites displayed lower intensive peaks which can be associated with reduced pore size after amine impregnation.

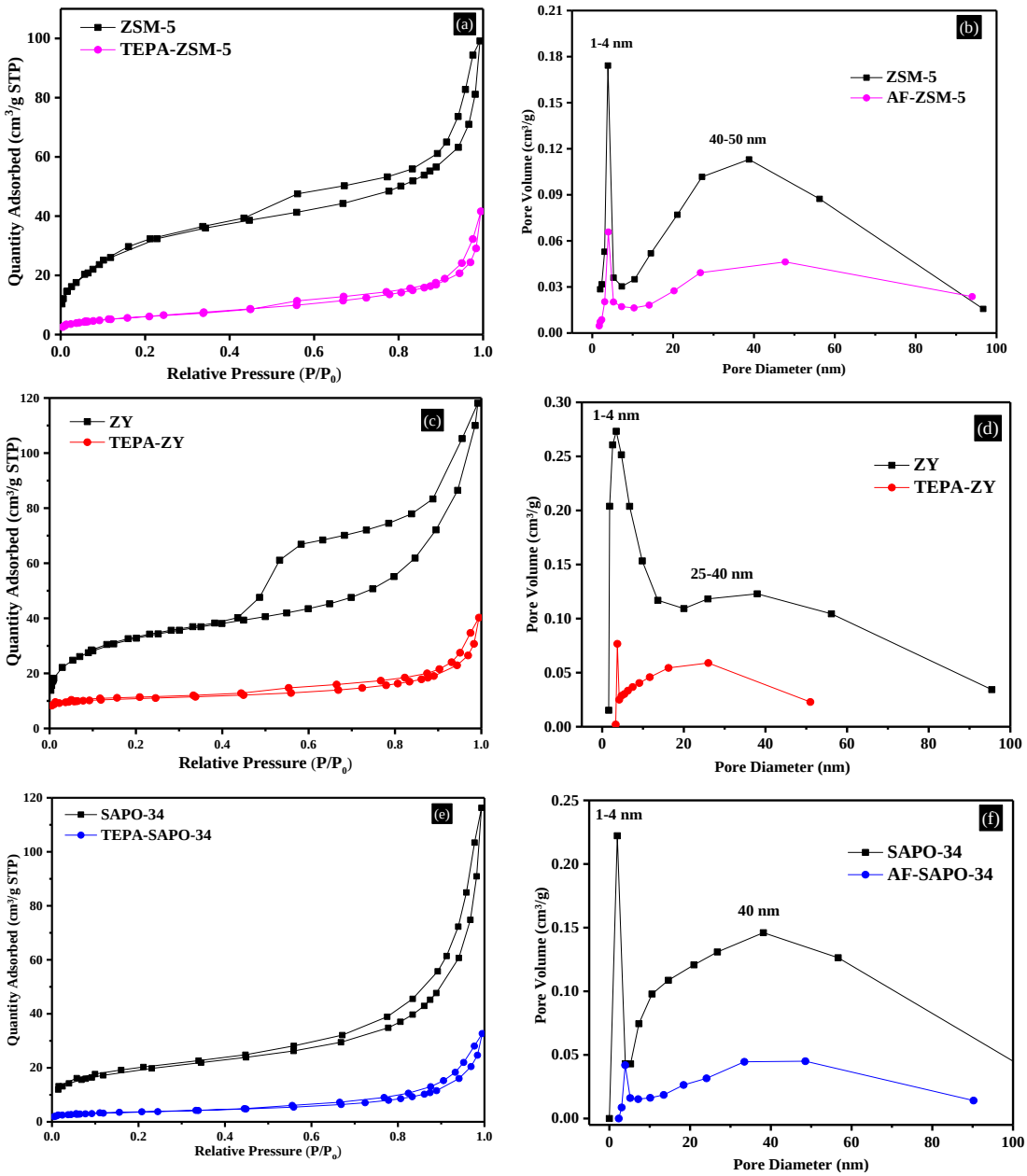

Figure 5. N_2 physisorption isotherms and PSD for bare and amine functionalized (a-b) ZSM-5, (c-d) ZY, and (e-f) SAPO-34. The isotherms of bare ZSM-5, ZY, and SAPO-34 have been lowered on the y-axis by 70, 60, and 120, respectively.

The corresponding surface area and pore volume values for the bare and functionalized zeolites are listed in Table 1. The slightly lower surface area of bare kaolin-based samples in comparison to the commercial zeolites (which is typically in the range 400 – 600 m^2/g) may be attributed to the presence of non-porous phases in kaolin structure that are not

decomposed completely during calcination of kaolin.[41] The mesopore volume of bare ZY (V_{meso}) was comparable to its micropore volume (0.10 vs 0.11 cm^3/g), whereas for ZSM-5 and SAPO-34 V_{meso} was significantly lower than V_{micro} (22% and 21%, respectively). Textural properties shown in Table 1 describe a general decreasing trend for surface area and pore volume after TEPA impregnation of TEPA, in accordance with filling the pores by polymer chains of the TEPA and in agreement with previously reported observations.[17,42–44] Notably, ZY partially retained its mesoporosity after TEPA impregnation.

Table 1: Textural properties of bare and functionalized kaolin-based zeolites.

Sample	**S_{BET}[a] (m^2/g)**	**V_{micro}[b] (cm^3/g)**	**V_{meso}[c] (cm^3/g)**	**d_{micro}[d] (nm)**	**d_{meso}[d] (nm)**
ZSM-5	275	0.18	0.04	1.7	3,25,42
TEPA-ZSM-5	22	0.16	0.01	1.1	4,6,8,17,31,48
ZY	335	0.11	0.10	1.2	3,8,15,23,32
TEPA-ZY	18	0.10	0.05	1.0	3,5,9,14,28
SAPO-34	449	0.19	0.04	1.6	3,6,10,16,38
TEPA-SAPO-34	35	0.12	0.03	1.1	5,16,26,33,49

(a) Obtained at P/P_0 values in the range of 0.05-0.3; (b) Estimated by t-plot.; (c) Estimated by subtracting V_{micro} from total pore volume; (d) Estimated using the Howarth-Kowazoe method.

Table 2 presents the calculated amine efficiencies (defined as mmol CO_2 per mmol N) obtained by TGA analysis. As can be seen, a higher amine loading was observed in zeolite Y (FAU) than in other zeolites which could be associated with its higher mesopore volume, as shown in Table 1, thus leading to uniform impregnation of TEPA into the mesopores.

As a result, a higher CO_2 capacity (1.12 mmol/g) and hence amine efficiency (0.21 mmol CO_2/mmol N) was obtained for TEPA-ZY. On the contrary, TEPA-ZSM-5 and TEPA-SAPO-34 exhibited very low amine efficiency, despite comparable amine loadings to TEPA-ZY, mainly due to their low mesopore volume which resulted in filling and blocking most of the micropores during TEPA impregnation, thus giving rise to less accessibility of both amine and zeolite sites for CO_2 molecules.

Table 2. Amine loading of TEPA-impregnated zeolites and CO_2 capacities obtained at 25 ºC using 5000 ppm CO_2/N_2.

Sample	**Amine content** (mmol N/g)	**CO_2 capacity** (mmol/g)	**Amine efficiency** (mmol CO_2/mmol N)
TEPA-ZSM-5	4.83	0.15	0.03
TEPA-ZY	5.27	1.12	0.21
TEPA-SAPO-34	4.13	0.45	0.10

Figure 6 presents the comparison between the CO_2 adsorption capacity of bare and functionalized clay-based zeolites when exposed to 5,000 ppm CO_2/N_2 at 25 ºC. Notably, the capacity of ZY zeolite increased 22% after incorporation of 10 wt% TEPA (from 0.9 to 1.1 mmol/g) whereas the other two zeolites showed an opposite trend whereby a 50% and 25% capacity loss was observed for ZSM-5 and SAPO-34, respectively after TEPA incorporation with the same weight loading (i.e. 10 wt%). As mentioned previously, such capacity loss after TEPA impregnation stems from the microporous nature of ZSM-5 and SAPO-34 samples, as opposed to more mesoporous nature of ZY, which results in pore filling and/or obstructing the other micropores and will eventually hinder diffusion of CO_2 molecules in the zeolite framework. Kim et al.[15] reported the same behavior for microporous SAPO-34 functionalized with APS. The APS-grafted SAPO-34 showed a substantial decrease (82%) in the adsorption capacity; the authors attributed this dramatic

capacity loss to the partial blockage of pores by the grafted amine molecules. The obtained CO_2 capacity for TEPA-ZY zeolite was comparable to some of other similar materials used for air capture.[8,45] By increasing the mesoporosity of the zeolite support and hence incorporation of larger amount of aminopolymer (i.e., TEPA), the capacity could be significantly improved. Indeed, zeolite supported amine adsorbents are advantages over

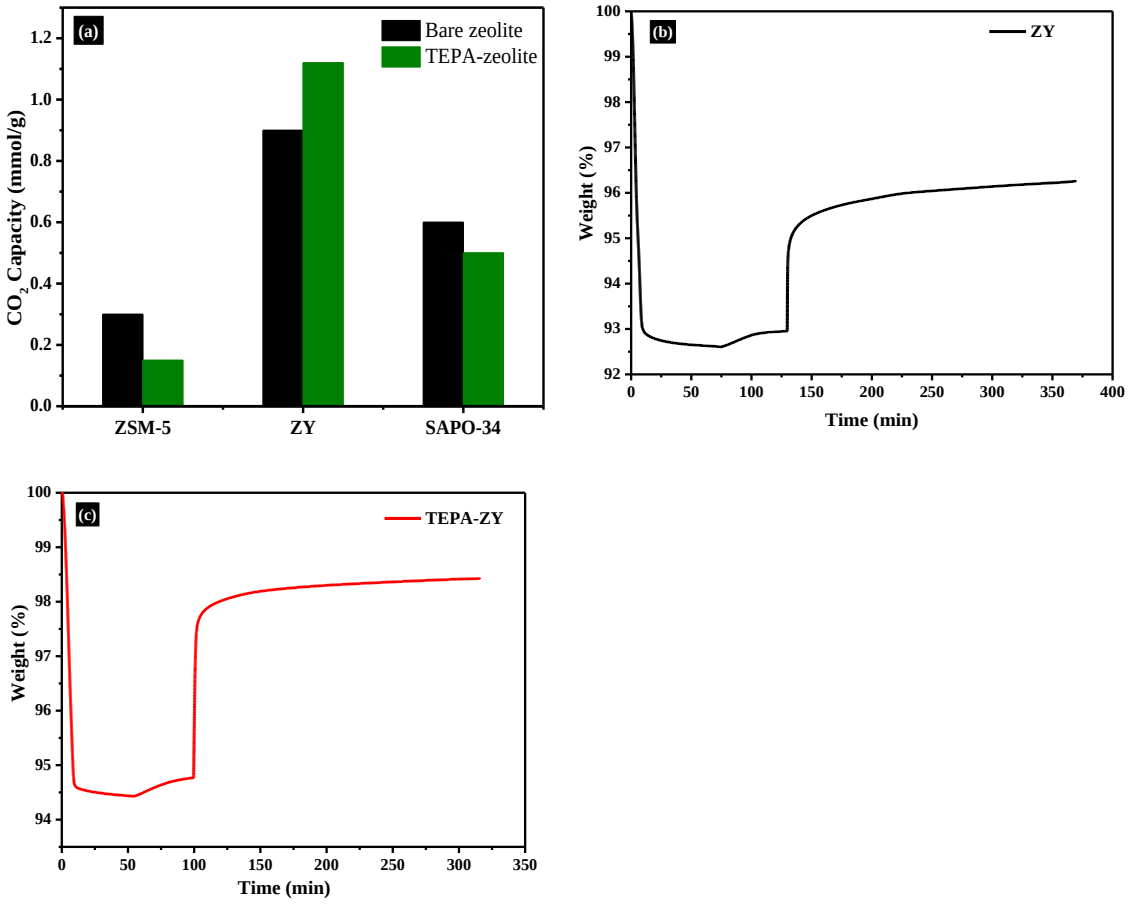

Figure 6. CO_2 adsorption capacity of (a) bare and TEPA-functionalized ZSM-5, ZY and SAPO-34, (b) TGA profile of ZY, and (c) TGA profile of TEPA-ZY at 25 ºC using 5000 ppm CO_2/N_2.

other oxide supports such as alumina and silica materials because zeolite support itself can contribute to CO_2 adsorption, however, to take advantage of both zeolite sites and amine

groups, a zeolite with a hierarchical pore structure containing both micropores and mesopores is required. It should also be mentioned here that the 0.5% CO_2 capacity of bare clay-based zeolites at 25 °C was compared with their commercial analogues, as shown in Table 3 and a comparable CO_2 uptake to that of commercial zeolites was found for the new materials. The TGA profiles of bare ZY and TEPA-ZY are presented in Figure 6(b-c).

Table 3. CO_2 capacities of commercial zeolites obtained at 25 ºC using 5000 ppm CO_2/N_2.

Sample	**CO_2 capacity** (mmol/g)
ZSM-5	0.6
ZY	1.2
SAPO-34	1.0

The stability of clay-based bare ZY and TEPA-ZY was assessed through cyclic capacity measurements and the results are displayed in Figure 7. It is apparent that TEPA-ZY showed no noticeable capacity loss after five consecutive adsorption-desorption cycles, similar to its pristine zeolite counterpart and a stable cyclic performance was obtained for this material. Typically, when amine content is high (e.g. 50 wt%), some degree of amine loss is expected from polyamines supported adsorbents due to evaporation of low molecular weight oligomers or amine leaching,[46,47] however, this was not the case in this study since a relatively low amine content (i.e. 10 wt%) was used to impregnate the clay-based zeolites. The cyclic TGA profiles of bare ZY and TEPA-ZY are presented in Figure 7b-c.

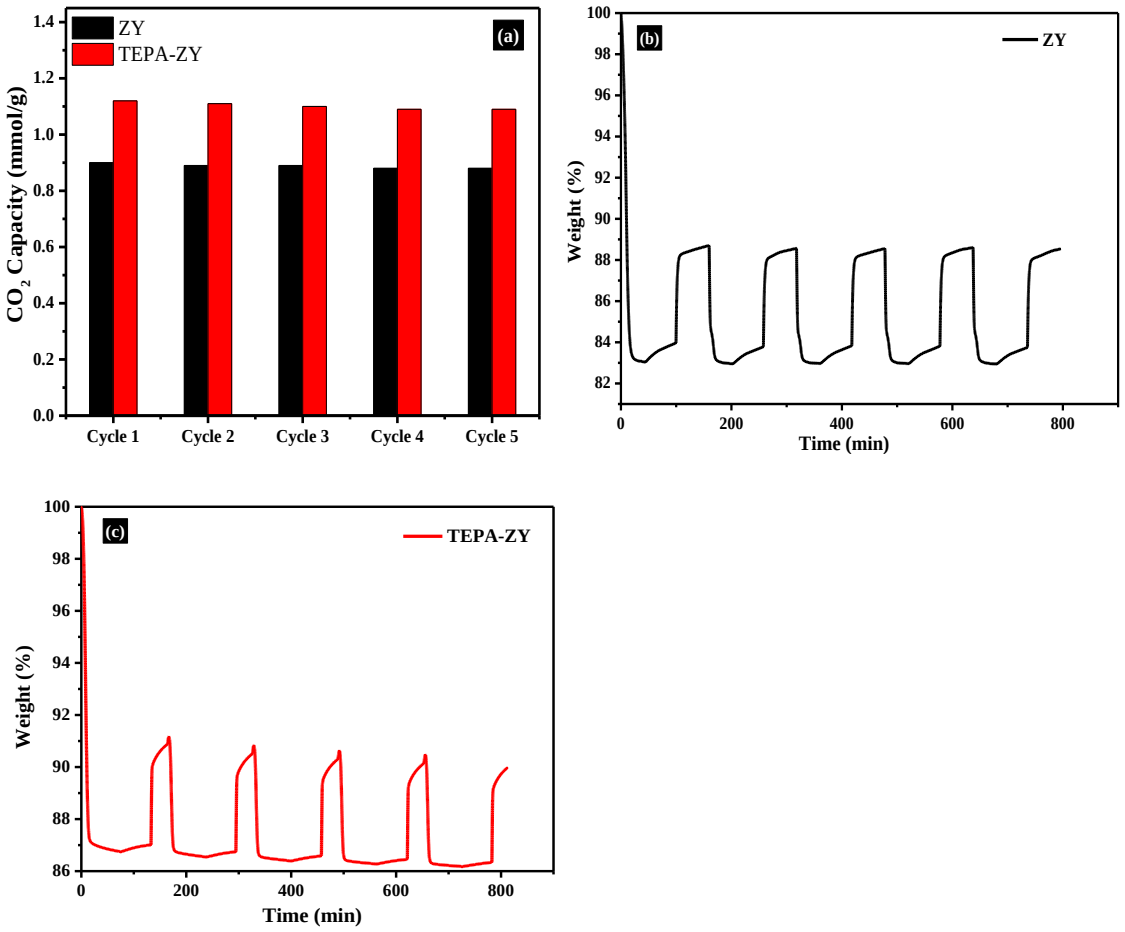

Figure 7. Cyclic adsorption capacity measurements of (a) bare ZY and TEPA-ZY; TGA capacity profile of (b) ZY and (c) TEPA-ZY at 25 ºC using 5000 ppm CO_2/N_2.

To evaluate the dynamic adsorption performance of bare and TEPA-impregnated zeolites, breakthrough experiments were conducted and the corresponding profiles are presented in Figure 8. As can be noticed, all TEPA-impregnated zeolites displayed a steep concentration front indicating relatively rapid adsorption kinetics. The pseudo-equilibrium capacity values, $q_{95\%}$, estimated from the breakthrough profiles (shown in Table 4) were found to be close to those obtained from the TGA measurements. The breakthrough width obtained for all functionalized zeolite samples was found to be shorter than that for bare

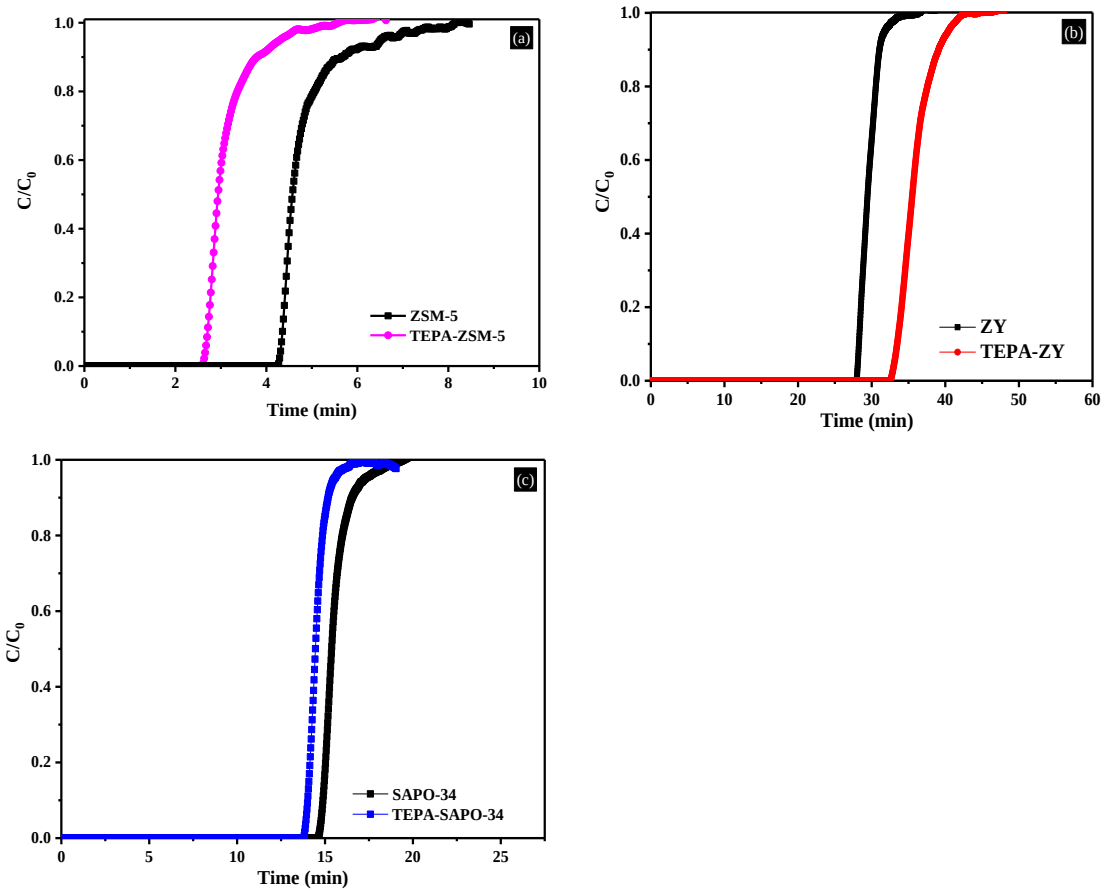

Figure 8. CO_2 breakthrough curves of bare and TEAP-impregnated (a) ZSM-5, (b) ZY and (c) SAPO-34 at 25 ºC using 5000 ppm CO_2/N_2.

Table 4: Dynamic adsorption data for kaolin-based bare and functionalized zeolites.

Sample	**$t_{5\%}$** (min)	**$t_{50\%}$** (min)	**$t_{95\%}$** (min)	**Breakthrough** width (min)	**$q_{95\%}$** (mmol/g)
ZSM-5	4	5	6	2	0.26
TEPA-ZSM-5	2	2	3	1	0.13
ZY	28	29	30	2	0.90
TEPA-ZY	33	34	36	3	1.09
SAPO-34	14	15	16	2	0.58
TEPA-SAPO-34	13	13	14	1	0.47

zeolites which can be correlated to faster adsorption kinetics. In agreement with adsorption capacities, the TEPA-ZY exhibited longer breakthrough time than the bare ZY zeolite while for TEPA-ZSM-5 and TEPA-SAPO-34, the breakthrough time was shorter than their corresponding bare zeolites.

4. CONCLUSION

Development of bimodal pore-network zeolites from a cheap and abundant source such as kaolin clay is of practical importance in various processes related to separation and catalysis. In this work, ZSM-5, ZY, and SAPO-34 zeolites were synthesized from kaolin clay and evaluated for CO_2 adsorption from air. The Kaolin-based zeolites were then functionalized with TEPA with varied amine loading. Our results indicated that successful incorporation of TEPA into the zeolite framework and improve in CO_2 adsorption capacity is largely dependent on the porosity and dimension of the zeolite pores. The kaolin-based ZY with larger mesopores was found to be a suitable zeolite for TEPA impregnation as opposed to ZSM-5 and SAPO-34 zeolites with microporous structure. Additionally, TEPA-ZY zeolite with higher CO_2 capacity than that for the bare ZY zeolite showed a stable performance and a relatively rapid uptake. The results presented in this study demonstrated that kaolin clay can be used as a suitable and inexpensive source for developing zeolites. The subsequent functionalization of these materials is largely dependent on their porosity and pore network. Moreover, the reported CO_2 adsorption capacities of functionalized clay-based zeolites are still low compared to other amine-functionalized mesoporous oxides and further improvements in the synthesis procedure are required to make this class of materials competitive with best-known CO_2 adsorbents used in air capture.

ACKNOWLEDGEMENT

The authors thank Xin Li and Amit Hajari for helping with nitrogen physisorption and breakthrough measurements. The authors also acknowledge Materials Research Center (MRC) of Missouri S&T for SEM and XRD analyses.

REFERENCES

[1] E. S. Sanz-Pérez, C. R. Murdock, S. A. Didas, C. W. Jones, *Chem. Rev.* **2016**, *116*, 11840−11876.

[2] K. S. Lackner, *Eur. Phys. J. Spec. Top.* **2009**, *176*, 93–106.

[3] C. W. Jones, *Annu. Rev. Chem. Biomol. Eng.* **2011**, *2*, 31–52.

[4] D. W. Keith, *Science* **2009**, *325*, 1654–1655.

[5] A. Al-Mamoori, Krishnamurthy, A., Rownaghi, A. A., F. Rezaei, *Energy Technol.* **2017**, DOI: 10.1002/ente.201600747.

[6] P. Bollini, S. A. Didas, C. W. Jones, *J. Mater. Chem.* **2011**, *21*, 15100–15120.

[7] L. A. Darunte, A. D. Oetomo, K. S. Walton, D. S. Sholl, C. W. Jones, *ACS Sustain. Chem. Eng.* **2016**, *4*, 5761–5768.

[8] A. Goeppert, M. Czaun, R. B. May, G. K. S. Prakash, G. A. Olah, S. R. Narayanan, *J. Am. Chem. Soc.* **2011**, *133*, 20164–20167.

[9] F. Liu, L. Wang, Z. Huang, C. Li, W. Li, R. Li, W. Li, *ACS Appl. Mater. Interfaces* **2014**, *6*, 4371–4381.

[10] P. E. Rajan, A. Krishnamurthy, G. Morrison, F. Rezaei, *Indoor Air* **2017**, DOI: 10.1111/ina.12386.

[11] S. Choi, J. H. Drese, C. W. Jones, *ChemSusChem* **2009**, *2*, 796–854.

[12] P. D. Jadhav, R. V. Chatti, R. B. Biniwale, N. K. Labhsetwar, S. Devotta, S. S. Rayalu, *Energy and Fuels* **2007**, *21*, 3555–3559.

[13] S. C. Lee, C. C. Hsieh, C. H. Chen, Y. S. Chen, *Aerosol Air Qual. Res.* **2013**, *13*, 360–366.

[14] X. Xu, X. Zhao, L. Sun, X. Liu, *J. Nat. Gas Chem.* **2009**, *18*, 167–172.

[15] J. Y. Kim, J. Kim, S. T. Yang, W. S. Ahn, *Fuel* **2013**, *108*, 515–520.

[16] A. Sayari, Y. Belmabkhout, R. Serna-Guerrero, *Chem. Eng. J.* **2011**, *171*, 760–774.

[17] S. A. Didas, A. R. Kulkarni, D. S. Sholl, C. W. Jones, *ChemSusChem* **2012**, *5*, 2058–2064.

[18] A. A. Rownaghi, F. Rezaei, J. Hedlund, *Chem. Eng. J.* **2012**, *191*, 528–533.

[19] A. A. Rownaghi, F. Rezaei, M. Stante, J. Hedlund, *Appl. Catal. B Environ.* **2012**, *119–120*, 56–61.

[20] A. A. Rownaghi, F. Rezaei, J. Hedlund, *Microporous Mesoporous Mater.* **2012**, *151*, 26–33.

[21] X. Li, A. Kant, Y. He, H. V. Thakkar, M. A. Atanga, F. Rezaei, D. K. Ludlow, A. A. Rownaghi, *Catal. Today* **2015**, *276*, 62–77.

[22] G. Garcia, E. Cardenas, S. Cabrera, J. Hedlund, J. Mouzon, *Microporous Mesoporous Mater.* **2016**, *219*, 29–37.

[23] P. Wang, A. Lv, J. Hu, J. Xu, G. Lu, **2011**, 9989–9997.

[24] V. K. Gupta, Suhas, *J. Environ. Manage.* **2009**, *90*, 2313–2342.

[25] *Rev. Chem. Eng* **2014**, *30*, 1–49.

[26] E. Mohiuddin, Y. Makar, M. M. Mdleleni, N. Sincadu, D. Key, T. Tshabalala, **2016**, *119*, 213–221.

[27] S. Chandrasekhar, P. N. Pramada, *Appl. Clay Sci.* **2004**, *27*, 187–198.

[28] J. Zhu, Y. Cui, Y. Wang, F. Wei, **2009**, 1–6.

[29] F. Rezaei, C. W. Jones, *Ind. Eng. Chem. Res.* **2013**, *52*, 12192–12201.

[30] A. A. Rownaghi, A. Kant, X. Li, H. Thakkar, A. Hajari, Y. He, P. J. Brennan, H. Hosseini, W. J. Koros, F. Rezaei, *ChemSusChem* **2016**, *9*, 1166–1177.

[31] P. J. Brennan, H. Thakkar, X. Li, A. A. Rownaghi, W. J. Koros, F. Rezaei, *Energy Technol.* **2017**, *5*, 327–337.

[32] M. Liu, J. Li, W. Jia, M. Qin, Y. Wang, K. Tong, H. Chen, *RSC Adv.* **2015**, *5*, 9237–9240.

[33] Y. Xia, Z. Yang, R. Mokaya, **2010**, 639–659.

[34] A. S. Kovo, O. Hernandez, S. M. Holmes, *J. Mater. Chem.* **2009**, *19*, 6207–6212.

[35] A. A. Rownaghi, F. Rezaei, J. Hedlund, *Catal. Commun.* **2011**, *14*, 37–41.

[36] A. A. Rownaghi, J. Hedlund, *Ind. Eng. Chem. Res.* **2011**, *50*, 11872–11878.

[37] R. N. M. Missengue, P. Losch, G. Sedres, N. M. Musyoka, O. O. Fatoba, B. Louis, P. Pale, L. F. Petrik, *Comptes Rendus Chim.* **2016**, *20*, 78–86.

[38] X. Wang, V. Schwartz, J. C. Clark, X. Ma, S. H. Overbury, X. Xu, C. Song, *J. Phys. Chem. C* **2009**, *113*, 7260–7268.

[39] F. Rezaei, P. Webley, *Chem. Eng. Sci.* **2009**, *64*, 5182–5191.

[40] F. Akhtar, L. Bergström, *J. Am. Ceram. Soc.* **2011**, *94*, 92–98.

[41] O. Castelein, B. Soulestin, J. P. Bonnet, P. Blanchart, *Ceram. Int.* **2001**, *27*, 517–522.

[42] F. Rezaei, M. A. Sakwa-Novak, S. Bali, D. M. Duncanson, C. W. Jones, *Microporous Mesoporous Mater.* **2015**, *204*, 34–42.

[43] S. S. A. Didas, R. Zhu, N. A. N. Brunelli, D. S. Sholl, C. W. Jones, *J. Phys. Chem. C* **2014**, *118*, 12302–12311.

[44] H. Thakkar, S. Eastman, A. Al-Mamoori, A. Hajari, A. A. Rownaghi, F. Rezaei, *ACS Appl. Mater. Interfaces* **2017**, *9*, 7489–7498.

[45] W. Chaikittisilp, R. Khunsupat, T. T. Chen, C. W. Jones, *Ind. Eng. Chem. Res.* **2011**, *50*, 14203–14210.

[46] Y. Labreche, Y. Fan, F. Rezaei, R. P. Lively, C. W. Jones, W. J. Koros, *ACS Appl. Mater. Interfaces* **2014**, *6*, 19336–19346.

[47] F. Rezaei, R. P. R. Lively, Y. Labreche, G. Chen, Y. Fan, W. J. Koros, C. W. Jones, *ACS Appl. Mater. Interfaces* **2013**, *5*, 3921–3931.

SECTION
3. CONCLUSION

Advance adsorbents such as zeolite, aminosilica and MOF were engineered, especially in monolithic form, using 3D printing technique (robocasting). Robust gas-solid contactors with tunable structural, physical and mechanical properties were fabricated by varying weight ratios of binders and plasticizers for practical and scalable CO_2 capture strategies. 3D printed monoliths exhibited comparable CO_2 capture capacity to their corresponding powders. The CO_2 uptake of 3D printed adsorbent monoliths were found to be proportional to the adsorbent loading. In addition, 3D printed monoliths showed high mechanical strength which can eventually prevent issues such as dust and attrition associated with traditional packing system. A negligible mass loss in CO_2 capacity measured on TGA by performing five consecutive cycles at 25 ºC demonstrated high stability of 3D printed monoliths. The dynamic adsorption performance of 3D printed adsorbent monoliths showed rapid CO_2 uptake which corresponds to high mass transfer activity when compared to their powder counterparts. The Monolithic form of adsorbents fabricated using 3D printer can be a potential substitute of their corresponding powders for practical and scalable CO_2 capture strategies.

Cost-effective kaolin clay based zeolites with MFI, FAU and CHA structures were synthesized and impregnated with tetraethylenepentamine (TEPA) to enhance CO_2 capture capacity. In TEPA impregnated kaolin based zeolites (MFI, FAU and CHA), zeolite Y (FAU) exhibited the highest capacity at 25 ºC and 1 bar at 0.5% CO_2/N_2 concentration to larger mesopores suitable for TEPA impregnation as opposed to ZSM-5 and SAPO-34 zeolites with microporous structure. Kaolin clay found to be an abundant and inexpensive source for developing zeolites for CO_2 capture.

4. FUTURE TASKS

The following tasks are recommended as future directions for improving the fabrication conditions of 3D-printed monoliths and their in-depth adsorption assessment.

1. Performing cyclic experiments such as pressure swing adsorption (PSA) should be conducted to assess the performance of the 3D-printed monoliths under realistic conditions to better demonstrate their advantage in terms of low pressure drop and enhanced kinetics.
2. Fabricating 3D-printed monoliths with different cell densities (cpsi) and shapes (square, oval, etc.)
3. Measuring pressure drop across a fixed-bed loaded with 3D-printed monoliths.
4. Further enhancement of the capture capacity of 3D-printed zeolite and MOF monoliths by various amines (PEI, TEPA and APS).
5. Evaluation of the adsorption performance of the 3D-printed monoliths under real conditions (humid feed, multi-component feed).
6. Optimizing the fabrication conditions for MOF monoliths to remove the binder using diluted acid or other solutions for enhancing the surface area and thus adsorption capacity.

REFERENCES

1. ESRL. Trends in Atmospheric Carbon Dioxide, Recent Montly Average Mauna Loa CO2. https://www.esrl.noaa.gov/gmd/ccgg/trends/.

2. Lackner K, Grimes P, Ziock H. *Capturing Carbon Dioxide from Air*.; 1999. http://www.netl.doe.gov/publications/proceedings/01/carbon_seq/7b1.pdf.

3. Bas E. Indoor Air Quality. Indoor Air. http://www.ggs-uk.com/indoor-air-quality-monitoring/. Published 2016.

4. Executive Yuan, Taiwan ROC. Indoor Air Quality Program (2006). Environmental Protection Administration (E.P.A.).

5. Biological Efeects of Carbon Dioxide Exposure. Centers for Disease Control and Prevention. https://www.dhs.wisconsin.gov/chemical/carbondioxide.htm. Published 2017.

6. Dangers of CO2: What You Need to Know. *CO2 meter.com; CO2 Measurement Specialisteasurement Specialist*. https://www.co2meter.com/blogs/news/4418142-dangers-of-co2-what-you-need-to-know. Published 2011.

7. Häggström M. Medical gallery of Mikael Häggström 2014. *WikiJournal Med*. 2014;1(2). doi:10.15347/wjm/2014.010.

8. Mendell MJ. Elevated Indoor Carbon Dioxide Impairs Decision-Making Performance.http://newscenter.lbl.gov/2012/10/17/elevated-indoor-carbon-dioxide-impairs-decision-making-performance/. Published 2012.

9. Grande CA, Blom R. Cryogenic adsorption of methane and carbon dioxide on zeolites 4A and 13X. *Energy and Fuels*. 2014;28(10):6688-6693. doi:10.1021/ef501814x.

10. Al-mamoori A, Krishnamurthy A, Rownaghi AA, Rezaei F. Carbon Capture and Utilization Update. 2017:1-17. doi:10.1002/ente.201600747.

11. Rownaghi AA, Kant A, Li X, et al. Aminosilane-Grafted Zirconia-Titiania-Silica Nanoparticles/Torlon Hollow Fiber Composites for CO<inf>2</inf> Capture. *ChemSusChem*. 2016;9(10). doi:10.1002/cssc.201600082.

12. Fan Y, Kalyanaraman J, Labreche Y, et al. CO2 Sorption performance of composite polymer/aminosilica hollow fiber sorbents: An experimental and modeling study. *Ind Eng Chem Res*. 2015;54(6):1783-1795. doi:10.1021/ie504603h.

13. Labreche Y, Fan Y, Rezaei F, Lively RP, Jones CW, Koros WJ. Poly(amide-imide)/silica supported PEI hollow fiber sorbents for postcombustion CO2 capture by RTSA. *ACS Appl Mater Interfaces*. 2014;6(21):19336-19346. doi:10.1021/am505419w.

14. Brennan PJ, Thakkar H, Li X, Rownaghi AA, Koros WJ, Rezaei F. Effect of Post-Functionalization Conditions on the Carbon Dioxide Adsorption Properties of Aminosilane-Grafted Zirconia/Titania/Silica-Poly(amide-imide) Composite Hollow Fiber Sorbents. *Energy Technol*. 2017;5(2). doi:10.1002/ente.201600328.

15. Sun SP, Wang KY, Rajarathnam D, Hatton TA, Chung TS. Polyamide-imide Nanofiltration hollow fiber membranes with elongation-induced nano-pore evolution. *AIChE J*. 2010;56(6):1481-1494. doi:10.1002/aic.12083.

16. Rezaei F, Webley P. Structured adsorbents in gas separation processes. 2010;70:243-256. doi:10.1016/j.seppur.2009.10.004.

17. Grande CA, Rodrigues AE. Electric Swing Adsorption for CO2 removal from flue gases. *Int J Greenh Gas Control*. 2008;2(2):194-202. doi:10.1016/S1750-5836(07)00116-8.

18. Magee HM, Sullivan MNS. Nitrogen Gas Adsorption in Zeolites 13X and 5A. *Adsorption*. 2010;24:2563-5698.

19. Currao A. Understanding Zeolite Frameworks. 2020:65.

20. W BCMLODM. *Atlas of Zeolite Framework Types*. Structure Commission of the International Zeolite Association by Elsevier; 2007. www.sciencedirect.com/science/book/9780444530646%0A%0A.

21. Sorg TJ, Schock MR, Lytle D a. Ion exchange softening : *Ion Exch softening*. 1999;(August):85-97.

22. Siriwardane R V., Shen MS, Fisher EP, Losch J. Adsorption of CO2 on zeolites at moderate temperatures. *Energy and Fuels*. 2005;19(3):1153-1159. doi:10.1021/ef040059h.

23. Primo A, Garcia H. Zeolites as catalysts in oil refining. *Chem Soc Rev*. 2014;43(22):7548-7561. doi:10.1039/C3CS60394F.

24. Jiří Čejka, Russell E Morris PN. *Zeolites in Catalysis: Properties and Applications*.; 2017. doi:http://dx.doi.org/10.1039/9781788010610.

25. Wu Q, Wang X, Qi G, et al. Sustainable synthesis of zeolites without addition of both organotemplates and solvents. *J Am Chem Soc*. 2014;136(10):4019-4025. doi:10.1021/ja500098j.

26. Johnson EBG, Arshad SE. Hydrothermally synthesized zeolites based on kaolinite: A review. *Appl Clay Sci*. 2014;97-98:215-221. doi:10.1016/j.clay.2014.06.005.

27. Jasra R V., Tyagi B, Badheka YM, Choudary VN, Bhat TSG. Effect of Clay Binder on Sorption and Catalytic Properties of Zeolite Pellets. *Ind Eng Chem Res*. 2003;42(14):3263-3272. doi:10.1021/ie010953l.

28. Musyoka NM, Missengue R, Kusisakana M, Petrik LF. Conversion of South African clays into high quality zeolites. *Appl Clay Sci*. 2014;97-98:182-186. doi:10.1016/j.clay.2014.05.026.

29. Mohiuddin E, Makar Y, Mdleleni MM, Sincadu N, Key D, Tshabalala T. Applied Clay Science Synthesis of ZSM-5 from impure and bene fi ciated Grahamstown kaolin : Effect of kaolinite content , crystallisation temperatures and time. 2016;119:213-221. doi:10.1016/j.clay.2015.10.008.

30. Garcia G, Cardenas E, Cabrera S, Hedlund J, Mouzon J. Synthesis of zeolite y from diatomite as silica source. *Microporous Mesoporous Mater*. 2016;219:29-37. doi:10.1016/j.micromeso.2015.07.015.

31. Chandrasekhar S, Pramada PN. Kaolin-based zeolite Y , a precursor for cordierite ceramics. 2004;27:187-198. doi:10.1016/j.clay.2004.07.001.

32. Ünveren EE, Monkul BÖ, Sarıoğlan Ş, Karademir N, Alper E. Solid amine sorbents for CO 2 capture by chemical adsorption: A review. *Petroleum*. 2017;3(1):37-50. doi:10.1016/j.petlm.2016.11.001.

33. Serna-guerrero R, Da E, Sayari A. New Insights into the Interactions of CO 2 with Amine-Functionalized Silica. *Ind Eng Chem Res*. 2008;47:9406-9412. doi:10.1021/ie801186g.

34. Pino L, Italiano C, Vita A, Fabiano C, Recupero V. ScienceDirect Sorbents with high efficiency for CO 2 capture based on amines-supported carbon for biogas upgrading. *JES*. 2016;48:138-150. doi:10.1016/j.jes.2016.01.029.

35. Rezaei F, Sakwa-novak MA, Bali S, Duncanson DM, Jones CW. Microporous and Mesoporous Materials Shaping amine-based solid CO 2 adsorbents : Effects of pelletization pressure on the physical and chemical properties. *MICROPOROUS MESOPOROUS Mater*. 2015;204:34-42. doi:10.1016/j.micromeso.2014.10.047.

36. Chen C, Kim J, Ahn WS. CO2capture by amine-functionalized nanoporous materials: A review. *Korean J Chem Eng*. 2014;31(11):1919-1934. doi:10.1007/s11814-014-0257-2.

37. Choi S, Watanabe T, Bae TH, Sholl DS, Jones CW. Modification of the Mg/DOBDC MOF with amines to enhance CO 2 adsorption from ultradilute gases. *J Phys Chem Lett*. 2012;3(9):1136-1141. doi:10.1021/jz300328j.

38. Sakwa-Novak MA, Yoo C-J, Tan S, Rashidi F, Jones CW. Poly(ethylenimine)-Functionalized Monolithic Alumina Honeycomb Adsorbents for CO2 Capture from Air. *ChemSusChem*. 2016;9:1-11. doi:10.1002/cssc.201600404.

39. Brilman DWF, Veneman R. Capturing atmospheric CO 2 using supported amine sorbents. *Energy Procedia*. 2013;37:6070-6078. doi:10.1016/j.egypro.2013.06.536.

40. Soto-cantu E, Cueto R, Koch J, Russo PS. Synthesis and Rapid Characterization of Amine-Functionalized Silica. 2012.

41. Didas SA, Kulkarni AR, Sholl DS, Jones CW. Role of Amine Structure on Carbon Dioxide Adsorption from Ultradilute Gas Streams such as Ambient Air. 2012:2058-2064. doi:10.1002/cssc.201200196.

42. Arstad B, Fjellvåg H, Ove K, Ole K, Richard S. Amine functionalised metal organic frameworks (MOFs) as adsorbents for carbon dioxide. 2008:755-762. doi:10.1007/s10450-008-9137-6.

43. Chem JM, Bollini P, Didas SA, Jones CW. Amine-oxide hybrid materials for acid gas separations. 2011:15100-15120. doi:10.1039/c1jm12522b.

44. Goeppert A, Czaun M, Surya Prakash GK, Olah GA. Air as the renewable carbon source of the future: an overview of CO2 capture from the atmosphere. *Energy Environ Sci*. 2012;5(7):7833. doi:10.1039/c2ee21586a.

45. Mason JA, Veenstra M, Long JR. Evaluating metal–organic frameworks for natural gas storage. *Chem Sci*. 2014;5(1):32-51. doi:10.1039/C3SC52633J.

46. Fan Y, Lively RP, Labreche Y, Rezaei F, Koros WJ, Jones CW. Evaluation of CO2 adsorption dynamics of polymer/silica supported poly (ethylenimine) hollow fiber sorbents in rapid temperature swing adsorption. *Int J Greenh Gas Control*. 2014;21:61-71. doi:10.1016/j.ijggc.2013.11.021.

47. Grande CA, Águeda VI, Spjelkavik A, Blom R. An ef fi cient recipe for formulation of metal-organic Frameworks. *Chem Eng Sci*. 2015;124:154-158. doi:10.1016/j.ces.2014.06.048.

48. Lee SC, Hsieh CC, Chen CH, Chen YS. CO 2 Adsorption by Y-Type Zeolite Impregnated with Amines in Indoor Air. 2013:360-366. doi:10.4209/aaqr.2012.05.0134.

49. Li X, Kant A, He Y, et al. Light olefins from renewable resources: Selective catalytic dehydration of bioethanol to propylene over zeolite and transition metal oxide catalysts. *Catal Today*. 2016;276. doi:10.1016/j.cattod.2016.01.038.

50. Llewellyn PL, Bourrelly S, Serre C, et al. High Uptakes of CO 2 and CH 4 in Mesoporous Metal s Organic Frameworks MIL-100 and MIL-101. 2008;(18):7245-7250.

51. Online VA, Taranco A, Me J, Herna L, Ferna R. Environmental Science and functional devices for energy and. 2017:846-859. doi:10.1039/c6ee03526d.

52. Rezaei F, Lawson S, Hosseini H, et al. MOF-74 and UTSA-16 film growth on monolithic structures and their CO<inf>2</inf> adsorption performance. *Chem Eng J*. 2017;313. doi:10.1016/j.cej.2016.11.058.

53. Ribeiro RPPL, Grande CA, Rodrigues AE. Electrothermal performance of an activated carbon honeycomb monolith. *Chem Eng Res Des*. 2012;90(11):2013-2022. doi:10.1016/j.cherd.2012.03.010.

54. Rownaghi AA, Rezaei F, Stante M, Hedlund J. Selective dehydration of methanol to dimethyl ether on ZSM-5 nanocrystals. *Appl Catal B Environ*. 2012;119-120:56-61. doi:10.1016/j.apcatb.2012.02.017.

55. Rownaghi AA, Kant A, Li X, et al. Aminosilane-Grafted Zirconia–Titiania–Silica Nanoparticles/Torlon Hollow Fiber Composites for CO2 Capture. *ChemSusChem*. 2016;9:1166-1177. doi:10.1002/cssc.201600082.

56. Sci C, Garcı J, Johnson M, Valla J, Ying JY. Catalysis Science & Technology Mesostructured zeolite Y — high hydrothermal stability and superior FCC catalytic performance w. 2012:987-994. doi:10.1039/c2cy00309k.

57. Shekhah O, Liu J, Fischer R a., Wöll C. MOF thin films: existing and future applications. *Chem Soc Rev*. 2011;40(2):1081. doi:10.1039/c0cs00147c.

58. Sherif D El, Knox JC, Marshall N, Flight S. International Space Station Carbon Dioxide Removal Assembly (ISS CDRA) Concepts and Advancements. 2005;2892:1-5.

59. Su F, Lu C, Kuo S, Zeng W. Adsorption of CO 2 on Amine-Functionalized Y-Type Zeolites. 2010;24(13):6567-6574. doi:10.1021/ef901077k.

60. Wang X, Ma X, Schwartz V, et al. A solid molecular basket sorbent for CO2 capture from gas streams with low CO2 concentration under ambient conditions. *Phys Chem Chem Phys*. 2012;14(4):1485-1492. doi:10.1039/c1cp23366a.

61. Xia Y, Yang Z, Mokaya R. Templated nanoscale porous carbons. 2010:639-659. doi:10.1039/b9nr00207c.

62. Zhao J, Nunn WT, Lemaire PC, et al. Facile Conversion of Hydroxy Double Salts to Metal-Organic Frameworks Using Metal Oxide Particles and Atomic Layer Deposition Thin-Film Templates. *J Am Chem Soc*. 2015;137(43):13756-13759. doi:10.1021/jacs.5b08752.

63. Pimentel BR, Fultz AW, Presnell K V, Lively RP. Synthesis of Water-Sensitive Metal − Organic Frameworks within Fiber Sorbent Modules. *Ind Eng Chem Res*. 2017;56:5070−5077. doi:10.1021/acs.iecr.7b00630.

64. Sanz-Pérez ES, Murdock CR, Didas SA, Jones CW. Direct Capture of CO2 from Ambient Air. *Chem Rev*. 2016;116:11840−11876. doi:10.1021/acs.chemrev.6b00173.

65. Stolaroff JK, Keith DW, Lowry G V. Carbon Dioxide Capture from Atmospheric Air Using Sodium Hydroxide Spray. *Environ Sci Technol*. 2008;42(8):2728-2735. doi:10.1021/es702607w.

66. Lee SC, Chae HJ, Lee SJ, et al. Development of Regenerable MgO-Based Sorbent Promoted with K2CO3 for CO2 Capture at Low Temperatures. *Environ Sci Technol*. 2008;42(8):2736-2741. doi:10.1021/es702693c.

67. Veselovskaya J V., Derevschikov VS, Kardash TY, Stonkus OA, Trubitsina TA, Okunev AG. Direct CO2 capture from ambient air using K2CO3/Al2O3 composite sorbent. *Int J Greenh Gas Control*. 2013;17:332-340. doi:10.1016/j.ijggc.2013.05.006.

68. Jones CW. CO2 capture from dilute gases as a component of modern global carbon management. *Annu Rev Chem Biomol Eng*. 2011;2:31-52. doi:10.1146/annurev-chembioeng-061010-114252.

69. Choi S, Gray ML, Jones CW. Amine-tethered solid adsorbents coupling high adsorption capacity and regenerability for CO2 capture from ambient air. *ChemSusChem*. 2011;4(5):628-635. doi:10.1002/cssc.201000355.

70. Titinchi SJJ, Piet M, Abbo HS, Bolland O, Schwieger W. Chemically modified solid adsorbents for CO 2 capture. *Energy Procedia*. 2015;63:8153-8160. doi:10.1016/j.egypro.2015.12.337.

71. Kumar A, Madden DG, Lusi M, et al. Direct Air Capture of CO2 by Physisorbent Materials. *Angew Chemie - Int Ed*. 2015;54(48):14372-14377. doi:10.1002/anie.201506952.

72. Hao BG, Li W, Qian D, Lu A. Rapid Synthesis of Nitrogen-Doped Porous Carbon Monolith for CO 2 Capture. 2010:853-857. doi:10.1002/adma.200903765.

73. Huff T, Knox J, Marshall N, Flight S. Evaluation of Sorbent Capacity Following Contamination in the ISS Atmosphere. 2015;(July).

74. Knox JC, Gostowski R, Watson D. Development of Carbon Dioxide Removal Systems for Advanced Exploration Systems. 2012;(July):1-17.

75. Akhtar F, Liu Q, Hedin N, Bergström L. Strong and binder free structured zeolite sorbents with very high CO2-over-N2 selectivities and high capacities to adsorb CO2 rapidly. *Energy Environ Sci*. 2012;5(6):7664-7673. doi:10.1039/c2ee21153j.

76. Rezaei F, Sakwa-Novak MA, Bali S, Duncanson DM, Jones CW. Shaping amine-based solid CO2 adsorbents: Effects of pelletization pressure on the physical and chemical properties. *Microporous Mesoporous Mater*. 2015;204(2015):34-42. doi:10.1016/j.micromeso.2014.10.047.

77. Ren J, Musyoka NM, Langmi HW, Swartbooi A, North BC, Mathe M. ScienceDirect Short Communication A more efficient way to shape metal-organic framework (MOF) powder materials for hydrogen storage applications. *Int J Hydrogen Energy*. 2015;40(13):4617-4622. doi:10.1016/j.ijhydene.2015.02.011.

78. Rezaei F, Webley P. Optimum structured adsorbents for gas separation processes. *Chem Eng Sci*. 2009;64(24):5182-5191. doi:10.1016/j.ces.2009.08.029.

79. Knox JC. Development of Carbon Dioxide Removal Systems for NASA's Deep Space Human Exploration Missions 2016 - 2017. *47th Int Conf Environ Syst*. 2017;(July):1-17.

80. Govender S, Friedrich H. Monoliths: A Review of the Basics, Preparation Methods and Their Relevance to Oxidation. *Catalysts*. 2017;7(2):62. doi:10.3390/catal7020062.

81. Villegas L, Masset F, Guilhaume N. Wet impregnation of alumina-washcoated monoliths: Effect of the drying procedure on Ni distribution and on autothermal reforming activity. *Appl Catal A Gen*. 2007;320:43-55. doi:10.1016/j.apcata.2006.12.011.

82. Ryu JH, Lee KY, La H, Kim HJ, Yang J Il, Jung H. Ni catalyst wash-coated on metal monolith with enhanced heat-transfer capability for steam reforming. *J Power Sources*. 2007;171(2):499-505. doi:10.1016/j.jpowsour.2007.05.107.

83. Niederberger M, Pinna N. Aqueous and Nonaqueous Sol-Gel. In: *Metal Oxide Nanoparticles in Organic Solvents*. Springer New York LLC; 2009:7-19.

84. Wang Y, Angelatos AS, Caruso F. Template Synthesis of Nanostructured Materials via Layer-by-Layer. 2008:848-858.

85. Öhrman O, Hedlund J, Sterte J. Synthesis and evaluation of ZSM-5 films on cordierite monoliths. *Appl Catal A Gen*. 2004;270(1-2):193-199. doi:10.1016/j.apcata.2004.05.004.

86. Hasan F a., Xiao P, Singh RK, Webley P a. Zeolite monoliths with hierarchical designed pore network structure: Synthesis and performance. *Chem Eng J*. 2013;223:48-58. doi:10.1016/j.cej.2013.02.100.

87. Rezaei F, Lawson S, Hosseini H, et al. MOF-74 and UTSA-16 film growth on monolithic structures and their CO2 adsorption performance. *Chem Eng J*. 2016;3. doi:10.1016/j.cej.2016.11.058.

88. Lawson S, Hajari A, Rownaghi AA, Rezaei F. MOF immobilization on the surface of polymer-cordierite composite monoliths through in-situ crystal growth. *Sep Purif Technol*. 2017;183:173-180. doi:10.1016/j.seppur.2017.03.072.

89. Zhakeyev A, Wang P, Zhang L, Shu W, Wang H, Xuan J. Additive Manufacturing: Unlocking the Evolution of Energy Materials. *Adv Sci*. 2017;1700187:1700187. doi:10.1002/advs.201700187.

90. Zhou X, Liu C. Three-dimensional Printing for Catalytic Applications : Current Status and Perspectives. 2017;1701134:1-13. doi:10.1002/adfm.201701134.

91. Ruiz-Morales JC, Tarancón A, Canales-Vázquez J, et al. Three dimensional printing of components and functional devices for energy and environmental applications. *Energy Environ Sci*. 2017:846-859. doi:10.1039/C6EE03526D.

VITA

Harshul Thakkar was born and brought up in November 1991 in Ahmedabad, GJ-INDIA. He received his B.E. in chemical engineering from one of the top universities of the state, L.D.College of Engineering with distinction. Harshul started his M.S. degree in chemical engineering at Missouri University of Science and Technology in January 2014 and joined Dr. Ali Rownaghi's research group, Catalysis and Membranes Research Laboratory in August 2014. In January 2016, he converted to PhD and joined Dr. Fateme Rezaei's research group, Adsorption and Separation Laboratory. During his PhD, Harshul worked on development of adsorbents into structured form, especially monolithic form, to capture CO_2 from enclosed environments. His focus was to develop monolithic adsorbents to prevent particle attrition generally encountered in traditional packing system such as beads, pellets etc. His project was funded by National Aeronautics and Space Administration (NASA). In addition, Harshul also trained and mentored more than five undergraduate and/or high school students. Harshul received his Ph.D. degree in Chemical Engineering from Missouri University of Science and Technology in December 2017.